



PONTIFICIA UNIVERSIDAD CATOLICA DE CHILE  
SCHOOL OF ENGINEERING

# **UNCERTAINTY ANALYSIS OF SEISMICALLY ISOLATED STRUCTURES**

**SEBASTIAN MIRANDA CAMUS**

Thesis submitted to the Office of Graduate Studies in partial fulfillment of  
the requirements for the Degree of Doctor in Engineering Sciences

Advisor:

**JUAN CARLOS DE LA LLERA MARTIN**

Santiago de Chile, October, 2020

© 2020, Sebastián Miranda Camus



PONTIFICIA UNIVERSIDAD CATOLICA DE CHILE  
SCHOOL OF ENGINEERING

# **UNCERTAINTY ANALYSIS OF SEISMICALLY ISOLATED STRUCTURES**

**SEBASTIAN MIRANDA CAMUS**

Members of the Committee:

**JUAN CARLOS DE LA LLERA MARTIN**

**MAGDALENA MARTA WALCZAK**

**JOSE LUIS ALMAZAN CAMPILLAY**

**CARLOS MEDEL VERA**

**EDUARDO MIRANDA**

**HECTOR JORQUERA GONZALEZ**

Thesis submitted to the Office of Graduate Studies in partial fulfillment of  
the requirements for the Degree Doctor in Engineering Sciences

Santiago de Chile, October, 2020

In memory of María Elena, my mother, and to Pedro and Valentina for their support during these years.

## ACKNOWLEDGEMENTS

First of all, I want to sincerely thank my advisor Professor Juan Carlos de la Llera, for his support, knowledge, and advice during the different stages of this doctoral research. I also wish to express my gratitude to the rest of my thesis committee for their valuable comments during this project: Professors Magdalena Walczak, Jose Luis Almazán, Carlos Medel, and Héctor Jorquera González.

I would like to especially thank Professor Eduardo Miranda, who received me as a Visiting Student Researcher at Stanford University. He has shown a deep commitment to this research, and his guidance has been extremely valuable. This abroad experience enriched not only this dissertation but also my personal and familiar life. I do want to thank Professor Miranda's research group for their support and hospitality as well.

Several institutions have supported this research at Pontificia Universidad Católica de Chile: the Structural and Geotechnical Engineering Department, the National Research Center for Integrated Natural Disaster Management (CIGIDEN), and the Laboratory for Dynamic Testing and Vibration Control. I do not want to miss the opportunity to acknowledge the continuous support of the Faculty of Engineering at Universidad del Desarrollo.

This research has been funded by CONICYT Doctorado Nacional 21161027, the National Research Center for Integrated Natural Disaster Management CONICYT /FONDAP/15110017, and FONDECYT grant 1170836 (SIBER-RISK).

Finally, I would like to express my deepest gratitude to my wife, Valentina, and my son Pedro. This work would not have been possible without their unconditional patience, encouragement, and love.

## TABLE OF CONTENTS

DEDICATION .....	III
ACKNOWLEDGEMENTS .....	IV
LIST OF TABLES .....	IX
LIST OF FIGURES.....	XI
I. INTRODUCTION.....	1
I.1 Seismic isolation .....	1
I.2 Modeling approaches for elastomeric bearings.....	3
I.3 Design-code modeling requirements.....	6
I.4 Objectives and organization of the thesis.....	10
II. A SIMPLIFIED AND VERSATILE ELEMENT MODEL FOR SEISMIC ISOLATION BEARINGS .....	18
II.1 Abstract .....	18
II.2 Introduction.....	19
II.3 Analytical Model.....	24
II.4 Model Validation.....	29
II.5 Cyclic Test Calibration.....	31
II.6 Earthquake Test Calibration.....	45
II.6.1 Earthquake simulation test calibration - Case 1 .....	46
II.6.2 Earthquake simulation test calibration - Case 2 .....	50
II.7 Summary And Conclusions.....	55

III.	UNCERTAINTY ON MEASUREMENT OF ELASTOMERIC ISOLATORS EFFECTIVE PROPERTIES .....	61
III.1	Abstract .....	61
III.2	Introduction .....	62
III.3	Uncertainty Evaluation Procedures .....	68
III.3.1	Elastomeric Isolators Test-Results Dataset .....	68
III.3.2	Summary of the GUM Uncertainty Quantification Methodology .....	70
III.3.3	Identifying uncertainty sources for input quantities <i>xi</i> .....	75
III.3.4	Monte-Carlo simulation methodology .....	78
III.4	Uncertainty Quantification – Results .....	79
III.4.1	Specimen 1 uncertainties – <i>GUM</i> Method .....	79
III.4.2	Specimen 1 uncertainties – Comparison between <i>GUM</i> and Monte-Carlo method. 87	
III.4.3	Dataset uncertainty results .....	88
III.5	Conclusions .....	97
IV.	THE EFFECT OF SPECTRAL SHAPE ON DAMPING MODIFICATION FACTORS.....	103
IV.1	Abstract .....	103
IV.2	Introduction .....	104
IV.3	Ground Motion Database .....	107
IV.4	Damping Modification Factors .....	111
IV.5	Spectral Shape Metrics.....	122
IV.6	Evaluation Of Possible Predictors.....	129
IV.7	Regression Model.....	135

IV.8 Summary And Conclusions.....	140
V. SUMMARY AND CONCLUSIONS .....	146
APPENDIX A .....	152
APPENDIX B .....	158

## LIST OF TABLES

	Page.
Table II-1. Summary of the most frequently used models.....	22
Table II-2. Seismic isolator specimens calibrated through cyclic tests.....	30
Table II-3. Seismic isolator specimens calibrated through earthquake simulator tests .....	31
Table II-4. Objective functions used to perform parameter calibration.....	34
Table II-5. Model-calibrated parameters for all specimens, when the best possible fit is obtained by setting many parameters to be displacement-dependent. (Displacement-dependent parameters are shown in bold characters).....	39
Table II-6. Model-calibrated updated parameters for all specimens. Displacement-dependent parameters are shown in bold characters.....	43
Table II-7. Model-calibrated parameters for Specimen 5 under the ICA ground motion record. Displacement-dependent parameters are shown in bold characters.....	49
Table II-8. Model-calibrated parameters for Specimen 6, under the El Centro ground motion record. Displacement-dependent parameters are shown in bold characters.....	52
Table III-1. Number of isolators and main geometric features .....	70
Table III-2. Summary of standard uncertainty components for $F +$ and $F -$ .....	82
Table III-3. Summary of standard uncertainty components for $\Delta +$ and $\Delta -$ .....	84
Table III-4. Summary of standard uncertainty components for $keff$ .....	85
Table III-5. Summary of standard uncertainty components for $\beta eff$ .....	87
Table III-6. Percentual difference ratio between <i>GUM</i> and Monte-Carlo uncertainty estimation for Specimen 1 .....	87

Table III-7. Expanded relative uncertainty in equivalent stiffness <b><i>keff</i></b> , considering only intercycle (Type A) uncertainty. ....	95
Table III-8. Expanded relative uncertainty in equivalent damping <b><i>βeff</i></b> , considering only intercycle (Type A) uncertainty. ....	96
Table III-9. Expanded relative uncertainty in equivalent stiffness <b><i>keff</i></b> , considering intercycle uncertainty (Type A) and Type B uncertainty sources.....	96
Table III-10. Expanded relative uncertainty in equivalent damping <b><i>βeff</i></b> , considering intercycle uncertainty (Type A) and Type B uncertainty sources.....	97

## LIST OF FIGURES

	Page.
Figure II-1. Proposed analytical model.....	25
Figure II-2. Force as a function of displacement for the three springs in the model. ....	26
Figure II-3. Force as a function of displacement for: a) $F1u + F2u$ , the original Menegotto-Pinto Model, and b) $F1u + F2u + F3u$ , the model proposed in this work.....	26
Figure II-4. Effect of variation of different parameters on force $F1u$ as a function of displacement (when $b = 0$ ).....	27
Figure II-5. Effect of variation of different parameters on force $F3u$ as a function of displacement.....	27
Figure II-6. Proposed rules for seismic unloading and reloading: (a) force as a function of displacement, general view, and (b) reversal point, detailed view. ....	29
Figure II-7. A comparison of errors calculated using the five objective functions in Table 4 for a given optimal parameter set, normalized to the minimum error for each optimization criterion. ....	36
Figure II-8. Comparison of the experimental test data (Specimen 1, $\gamma = 2.0$ ) and the model-fitted data using different objective functions to identify the optimal set of parameters: (a) dissipated energy deviation minimization; (b) force deviation minimization; and (c) stiffness deviation minimization.....	38
Figure II-9. Experimental test data and best model-fitted data for specimens: (a) 1, (b) 2, (c) 3, and (d) 4, as described in Table 2. The model parameters used in each Specimen are listed in Table 5.....	40

Figure II-10. Model-fitted relative error as a function of the number of displacement-dependent parameters, Specimen 1 .....	42
Figure II-11. Experimental test and simplified model-fitted data for: (a) Specimen 1 with $b$ and $uh$ displacement-dependent; (b) Specimen 2 with $b$ and $R$ displacement-dependent; (c) Specimen 3 with $Fy$ and $b$ displacement-dependent; and (d) Specimen 4 with $R$ displacement-dependent. The model parameters for each case are listed in Table 6.....	44
Figure II-12. Displacement-dependent parameter $pi$ as a function of the isolator shear strain, when calibrating with earthquake test results: (a) Functional Form 1, FF1; and (b) Functional Form 2, FF2.....	46
Figure II-13. Force-displacement curves for the experimental test and the model-fitted data under the ICA ground motion record: (a) Five displacement-dependent parameters; and (b) No displacement-dependent parameters, as detailed in Table 7. ....	49
Figure II-14. Force as a function of time for the experimental test and the model-fitted data, under the ICA ground motion record: (a) Five displacement-dependent parameters; and (b) No displacement-dependent parameters, as detailed in Table 7. ....	50
Figure II-15. Force-displacement curves for the experimental test and the model-fitted data, under <i>El Centro</i> ground motion record: (a) Five parameters displacement-dependent; and (b) No displacement-dependent parameters, as detailed in Table 8. ....	52
Figure II-16. Force as a function of time for the experimental test and the model-fitted data, under the <i>El Centro</i> ground motion record: (a) Five displacement-dependent parameters; and (b) No displacement-dependent parameters, as detailed in Table 8.....	53

Figure II-17. Relative error as a function of the number of displacement-dependent parameters for both specimens being calibrated with earthquake simulator tests. ....	55
Figure III-1. (a) Shear force – lateral displacement curve for an annular elastomeric isolator with an external diameter $D_{ext} = 70\text{ cm}$ , internal diameter $D_{int} = 10\text{ cm}$ , and total rubber height $H_r = 16.2\text{ cm}$ , considering four displacement sequences with $\gamma = 0.25, 0.50, 1.00$ , and 1.50 and six repetition cycles for each sequence; (b) Different maximum force values used for uncertainty calculation; (c) Equivalent stiffness $keff$ as defined in ASCE-7 and NCh2745; and (d) Energy dissipated in one displacement cycle, $E_{loop}$ , as required for equivalent damping $\beta_{eff}$ calculation.....	66
Figure III-2. Seismic isolator geometric parameters.....	69
Figure III-3. Ishikawa Diagram for effective stiffness uncertainty quantification .....	77
Figure III-4. Ishikawa Diagram for damping ratio uncertainty quantification .....	77
Figure III-5. Expanded relative uncertainty in equivalent stiffness $keff$ for the seismic isolators dataset, considering only intercycle uncertainty: (a) Compound 1, using cycles 2 through 6, (b) Compound 2, using cycles 2 through 6, (c) Compound 1, using cycles 1 through 5, and (d) Compound 2, using cycles 1 through 5 (legend notation, $x = keff$ , $s = \sigma_{keff}$ , and n = number of samples) .....	89
Figure III-6. Expanded relative uncertainty for the effective damping $\beta_{eff}$ of the seismic isolator dataset, considering only intercycle uncertainty: (a) cycles 2 to 6 of Compound 1, (b) cycles 2 to 6 of Compound 2, (c) cycles 1 to 5 of Compound 1, and (d) cycles 1 to 5 of Compound 2 (legend notation, $x = \beta_{eff}$ , $s = \sigma_{\beta_{eff}}$ , and n = number of samples).....	91

Figure III-7. Expanded relative uncertainty in equivalent stiffness  $\mathbf{keff}$  for the seismic isolators dataset, considering intercycle uncertainty and Type B uncertainty sources: (a) compound 1, using cycles 2 through 6, (b) compound 2, using cycles 2 through 6, (c) compound 1, using cycles 1 through 5, and (d) compound 2, using cycles 1 through 5 (legend notation,  $\mathbf{x} = \mathbf{keff}$ ,  $\mathbf{s} = \sigma\mathbf{keff}$ , and  $n$  = number of samples) ..... 93

Figure III-8. Expanded relative uncertainty of the equivalent damping ratio  $\mathbf{\betaeff}$  for the seismic isolators dataset, considering intercycle uncertainty and Type B uncertainty sources: (a) Cycles 2 through 6 of Compound 1, (b) Cycles 2 through 6 of Compound 2, (c) Cycles 1 through 5 of Compound 1, and (d) Cycles 2 through 5 of Compound 2 (legend notation,  $\mathbf{x} = \mathbf{\betaeff}$ ,  $\mathbf{s} = \sigma\mathbf{\betaeff}$ , and  $n$  = number of samples) ..... 94

Figure IV-1. Magnitude versus source-to-site distance (minimum distance between source and site,  $Rrup$ ) for the considered ground motion database..... 109

Figure IV-2. Variability of record duration as a function of magnitude; (a)  $D5 - 75$  versus  $Mw$ , and (b)  $D5 - 95$  versus  $Mw$ . ..... 110

Figure IV-3. Variability of record duration as a function of source-to-site distance (minimum distance between source and site,  $Rrup$ ); (a)  $D5 - 75$  versus  $Rrup$ , and (b)  $D5 - 95$  versus  $Rrup$ . ..... 111

Figure IV-4. Effect of damping ratio and oscillator period on median  $\eta$  values, considering arbitrary horizontal components and RotI50 horizontal components, in blue solid and red dashed lines, respectively. The shaded area represents values between the 16<sup>th</sup> and 84<sup>th</sup> percentiles of  $\eta$ . ..... 112

Figure IV-5. Effect of magnitude on median $\eta$ values, calculated without site effect normalization and calculated with site effect normalization, in solid and dashed lines, respectively.....	114
Figure IV-6. Damping modification factors: (i) median values calculated from a sub-set of Chilean ground motions with a minimum magnitude of 5.7; (ii) values currently specified in NCh 2745; (iii) values predicted by Lin and Chang (2004) model; (iv) values currently specified in ASCE/SEI 7-16; and (v) median values calculated from a sub-set of Chilean ground motions with a minimum magnitude of 8.0.....	117
Figure IV-7. Duration $D5 - 95$ versus magnitude; (a) interface subduction events, and (b) inslab events.....	119
Figure IV-8. Median $\eta$ values as a function of oscillator period for interface ground motion set and inslab ground motion set, in solid and dashed lines, respectively. ....	120
Figure IV-9. Effects of site class (following ASCE/SEI 7-16 classification) on median $\eta$ values as a function of oscillator period.....	122
Figure IV-10. Contour curves of equal $R2$ for $\eta$ as a function of $SaRatio$ for different $a$ and $b$ pairs: (1) $T = 0.5 s$ and $\xi = 2\%$ ; (2) $T = 1.5 s$ and $\xi = 2\%$ ; (3) $T = 3.0 s$ and $\xi = 2\%$ ; (4) $T = 0.5 s$ and $\xi = 20\%$ ; (5) $T = 1.5 s$ and $\xi = 20\%$ ; and (6) $T = 3.0 s$ and $\xi = 20\%$ . .....	126
Figure IV-11. $a$ and $b$ factor optimal values as a function of vibration period for different damping ratios.....	127
Figure IV-12. $R2$ values measuring the correlation between $\eta$ and $SaRatio$ as a function of vibration period and damping ratio for two different methodologies to compute $SaRatio$ : (1)	

considering optimal values of $a$ and $b$ factors; and (2) considering constant values of $a$ and $b$ factors, displayed with markers and solid lines, respectively.....	129
Figure IV-13. $\eta$ values as a function of earthquake magnitude, duration $D5 - 95$ , epsilon ( $\epsilon$ ), and $SaRatio$ for the complete ground motion set and an SDOF oscillator with $T=3.0$ s and $\xi = 20\%$ .....	131
Figure IV-14. Contour curves of equal $R2$ for different combinations of oscillator periods and damping ratios when using different predictors: a) $SaRatio$ ; b) $SaRatio$ and earthquake magnitude; c) $SaRatio$ and duration $D5 - 95$ ; and d) $SaRatio$ , earthquake magnitude, and duration $D5 - 95$ . .....	132
Figure IV-15. Coefficient of determination $R2$ as a function of oscillator period for different regression models: a) 2% damping ratio; b) 10% damping ratio; and c) 20% damping ratio. ....	134
Figure IV-16. Median $\eta$ values as a function of $SaRatio$ for magnitude-binned ground motion records. ....	135
Figure IV-17. $\eta$ versus $SaRatio$ scattered data for different oscillator periods.....	136
Figure IV-18. 189,720 ( $\xi$ , $SaRatio$ , $\eta$ ) sample points to perform non-linear regression. ..	137
Figure IV-19. Proposed model to estimate $\eta$ as a function of damping ratio $\xi$ and $SaRatio$ (same data, different views). ....	139
Figure IV-20. Residuals between observed and estimated damping modification factors $\eta$ as a function of $\beta$ and $SaRatio$ .....	140

PONTIFICIA UNIVERSIDAD CATOLICA DE CHILE  
SCHOOL OF ENGINEERING

UNCERTAINTY ANALYSIS OF SEISMICALLY ISOLATED STRUCTURES

Thesis submitted to the Office of Graduate Studies in partial fulfillment of the  
requirements for the Degree of Doctor in Engineering Sciences by

SEBASTIAN MIRANDA CAMUS

ABSTRACT

This dissertation presents an original investigation of several topics related to seismic analysis and currently-implemented code-design procedures for seismically isolated structures, focusing primarily on high-damping rubber-based isolators.

A considerable effort to develop accurate mathematical models to represent rubber-based isolators' force-displacement behavior has been made in the last decades. These research-oriented models can represent complex phenomena as shear-strain hardening, scragging, and strain-rate dependence. However, engineering design procedures have not embraced these advanced modeling techniques, and the implementation of equivalent linear or bilinear models using deterministic parameters is still recommended for seismic response assessment. This approach neglects the model parameters' inherent uncertainty and ignores several characteristics of the isolators' force-displacement relationship, whose relevance should be elucidated.

As the number of isolated structures increases steadily in Chile, other Latin American countries, and most of the world's seismically active regions, this research aims to close some aspects of the gap between the research-oriented modeling techniques and the simplified engineering design procedures. Particular emphasis is placed on the uncertainty

quantification of the isolators' effective properties currently used in engineering design procedures. To reach this goal, this thesis is divided into three stages: (i) the development of a simplified and versatile element model for seismic isolators' response history analysis, to be implemented in engineering design practices but able to capture accurately relevant features of isolators' behavior; (ii) an uncertainty analysis of the properties used in equivalent lateral force and response spectrum procedures, quantifying the variability of the measured-by-test effective stiffness and effective damping of a vast isolator dataset; and (iii) a statistical analysis of damping modification factors used to correct the seismic demand in equivalent lateral force and response spectrum procedures, aiming to find better predictors for these damping factors based on spectral shape metrics.

It is highly expected that some findings of this research can improve current design methodologies, allowing for a better estimation of interstory drifts, inertial forces, and floor accelerations on protected structures at a reasonable additional effort. The implementation of the element model presented in this thesis in general-purpose software-packages for seismic analysis is encouraged. Moreover, some findings related to effective properties uncertainties and damping modification factors could enrich current provisions in the Chilean design code for seismically isolated structures.

Keywords: elastomeric isolation modeling, uncertainty in measurement, GUM methodology, damping modification factor, elastic displacement responses of structures with high damping, elastic displacement responses of structures with base isolation, spectral shape metrics.

Members of the Doctoral Thesis Committee:

Juan Carlos de la Llera Martin

Magdalena Marta Walczak

José Luis Almazán Campillay

Carlos Medel Vera

Eduardo Miranda

Héctor Jorquera González

Santiago, October, 2020

## I. INTRODUCTION

### I.1 Seismic isolation

Seismic isolation is a passive vibration control technique that has proven to be useful in reducing seismic demand in residential buildings, hospitals, schools, bridges, lifelines, industrial facilities, and other infrastructure. When properly designed and implemented, seismic isolators can significantly reduce interstory drifts, inertial forces, and floor accelerations seismic demands. This reduction is due to the inclusion of a flexible interface (i.e., seismic isolators) that uncouples the superstructure response from the ground motion and increases energy dissipation while providing a large vertical strength and stiffness to withstand vertical loads. This flexible interface needs to accommodate a large relative displacement to uncouple the superstructure response from ground motion effectively.

Different materials and geometries have been used historically to achieve the isolation effect [1][2]. Modern seismic isolation systems can be roughly classified in: (i) elastomeric isolators, based on the flexibility of natural or synthetic rubber; (ii) friction isolators, based on the relative displacement of two surfaces with a small friction coefficient; and (iii) other isolators, e.g., spring isolators or flexible piles isolators. Elastomeric isolators can be categorized in: (i) low damping rubber bearings (LDRB); (ii) high damping rubber bearings (HDRB); and (iii) lead-core rubber bearings (LRB) [3].

A recent work by Makris [1] compiled early developments on seismic isolation in Japan, New Zealand, and the United States. Eriksen et al. [4] compared the use and development of seismic isolation and North and South America. The authors concluded that due to the

life and property losses generated by frequent large earthquakes striking Latin America, engineering communities, governments, and populations have pushed the implementation of seismic protection systems to achieve higher performance structures and more resilient systems. This work highlighted the Chilean case, mirroring the Japan experience, as the use of seismic isolation increased substantially after the successful behavior of the isolated structures in 2010  $M_w$  8.8 Maule earthquake. The authors also described several applications in Peru, Colombia, Mexico, and other countries. On the other hand, in the United States and Canada, the number of seismically isolated buildings has not increased as expected, and more interest has been shown in protecting bridges and non-structural components. Clemente [2] presented a summary of base-isolation case histories, emphasizing applications in Italy. Also, seismic responses of instrumented base-isolated buildings are presented and discussed.

Elastomeric isolation has been used in Chile since 1992 when a four-story low-cost building was erected on eight HDRB [5]. The first floor and the upper three floors were built with reinforced concrete and confined masonry, respectively. A twin building with conventional foundations was constructed for comparison purposes. The results showed a reduction of the building peak accelerations even for small recorded motions. In 2004 De la Llera et al. [6] carried out a comprehensive study on analysis, testing, and implementation of isolated buildings. They concluded that a remarkable growth in the number of projects with seismic isolation was expected for the following years.

Based on several aspects of the mentioned studies and the international experience from seismic codes as the Uniform Building Code [7], the first version of the Chilean code for seismically isolated structures NCh2745 [8] was released in 2003.

In 2010 Chile suffered the consequences of the  $M_w$  8.8 Maule earthquake. To that date, twelve structures were protected with seismic isolation, mainly critical infrastructure as hospitals, bridges, LNG tanks, and the Puerto Coronel wharf. As stated by Almazan [9], the behavior of structures and non-structural components was excellent, assuring operation continuity in all cases. Moroni et al. [10] studied the accelerometers readings in the building detailed in [5] and in bridges in Santiago and Vina del Mar. These structures presented remarkable reductions in the recorded accelerations.

There are currently more than 60 isolated structures in Chile, including hospitals, bridges, emergency management facilities, apartment buildings, university buildings, religious buildings, and industrial facilities. This technique has also been used to retrofit patrimonial structures as the *Basilica del Salvador* in Santiago [11]. Most of the isolators installed in these projects were tested by the "Laboratory for dynamic testing and vibration control" at Pontificia Universidad Catolica de Chile, and their results were generously shared for this research project.

As previously stated, seismic isolators can be roughly classified in elastomeric-based or friction-based. This research mainly focuses on quantifying and reducing uncertainty in elastomeric isolators; however, some findings are also applicable to friction-based isolators.

## **I.2 Modeling approaches for elastomeric bearings**

Modeling strategies for elastomeric bearings depend on the isolator type. Isolators manufactured from untreated rubber exhibiting low damping levels (LDRB) can be adequately modeled as linear elastic systems with viscous damping. These devices' dissipation capacity can be improved through the inclusion of a lead core (LRB). In this case,

the behavior can be accurately modeled using bilinear constitutive relationships, combining a linear model and a perfectly plastic model for low damping rubber and lead, respectively. High-damping rubber bearings (HDRB) are manufactured from reinforced rubber, primarily through the inclusion of fillers as carbon black, oils, or resins to increase damping. HDRBs present a highly nonlinear shear force - lateral displacement constitutive relation, much more complicated to model than the ones from LDRBs or LRBs, showing several complex material effects as: (i) Mullins effect [12] that produces degradation of the peak lateral force and lateral stiffness when the isolation bearing is subjected to cyclic loading; (ii) strain-rate dependency; (iii) axial load dependency; (iv) load-path dependency; and (v) internal temperature dependency. Additionally, geometric effects (e.g., buckling [13]) also influence isolator response.

Several modeling techniques have been proposed and implemented to assess the seismic response of HDRB-based isolated structures. A comprehensive set of phenomenological models aiming to capture different features of the measured-by-test force-displacement constitutives is available in the literature. Additionally, several finite element efforts have been made to model HDRB's behavior, considering the use of elastic, plastic, or hyperelastic materials [14][15][16].

Phenomenological models can be grouped based on their rate-dependency (i.e., the dependence of the isolator force on the isolator velocity). In the early days of HDRBs modeling, rate-independent approaches considered smooth hysteretic constitutives [17][18], unable to capture the nonlinear stiffening showed at large shear strains. In the seminal work of Kikuchi and Aiken [19], a model able to account for this stiffening effect and stiffness degradation between cycles was presented.

Grant et al. [20] presented a model capable of describing the behavior under bidirectional loading. This model includes two damage parameters to account for scragging degradation and short-term Mullins effect [12]. Yamamoto et al. [21] and Kikuchi et al. [22] presented models based on the original Kikuchi and Aiken model [19], including the coupling between horizontal and vertical effects, nonlinear behavior at large shear strains, dependence on axial load, and horizontal bidimensional coupling.

Gjorgjiev and Garevski [23] developed a simple polynomial model capable of capturing hardening but unable to model Mullins' effect and axial load dependence. Properties modification factors can be applied to model parameters to include aging, scragging, and internal temperature effects. Markou and Manolis [24] presented a series of one-dimensional models based on several elements arranged in parallel. These elements include nonlinear elastic springs, elastoplastic elements, and hysteretic dampers. This practitioner-oriented model showed good agreement up to shear strains of two. Recent efforts on rate-independent models include the work of Oliveto et al. [25] that combined several bi-dimensional simple formulations to describe the response of HDRBs at low, intermediate, and high shear strain levels.

This research work presents a newly developed simplified and versatile rate-independent model for seismic isolation [26] capable of accurately represent the behavior of different types of isolation devices, including HDRBs. Additional references to rate-independent models in the literature can be found in Chapter II of this thesis.

There is also a wide variety of rate-dependent models in the literature. Tsopelas et al. [27] presented a model that can account for large shear-strain hardening, currently available in the software package 3D-BASIS. Hwang et al. [28] developed a model that includes

scragging, frequency, temperature, and Mullins' effects. Recent efforts in rate-depending HDRBs modeling include the work of Yuan et al. [29], which proposed a model with hyper-elastic springs and a dashpot to represent the strain-rate dependence. For a comprehensive and detailed literature review on rate-dependent models, the reader is referred to [30].

### **I.3 Design-code modeling requirements**

The design of seismically isolated structures in Chile must follow the provisions from NCh2745 [31]. This seismic code declares the following modeling philosophy: "Different methodologies can be used to model the seismic response of isolated structures, from simplified models to nonlinear tridimensional analyses of the complete building. Model detail needs to be coherent with the complexity of the structures. Generally speaking, flexible superstructures and structures with height or plan irregularity shall require more sophisticated models." Section 8.5.2.2 of this code establishes that seismic isolation modeling should be able to capture: (i) isolators spatial distribution; (ii) both horizontal displacements and plan torsion; (iii) overturning moments generating uplift in the isolators; and (iv) vertical force effects, bi-directional actions, and strain-rate when these variables affect isolators' properties. Additionally, the commentary section (C6.5.1.b.1) advises that uncertainty in isolators' properties should be considered by using the highest stiffness for assessing the design forces in the superstructure and the lowest stiffness for evaluation of the displacement demand over the isolation system.

NCh 2745 [31] suggests three different modeling strategies for response history analysis of structures with elastomeric isolators: (i) for low-damping rubber bearings (LDRBs), a linear model and a linear-viscous model are recommended for low and high shear strains,

respectively; (ii) for lead-core rubber bearings (LRBs), a bilinear hysteretic model should suffice and; (iii) for high-damping rubber bearings (HDRBs) a bilinear constitutive model or a Bouc-Wen [17] model should be implemented. This seismic code does not have specific recommendations on which features of the force-displacement curves, described above in Section I.2., are more relevant in seismic response and should be explicitly included in the structural model.

Response spectrum analysis is permitted in NCh2745 [31] when the isolators show a force-displacement curve feasible to be represented by a linear equivalent model, the effective modal damping is lower than 30 %, and there is no expected pounding with adjacent structures. In this case, seismic isolators can be modeled with an effective (secant) stiffness, and seismic demand is reduced based on effective damping, calculated as presented elsewhere [32]. A detailed analysis of the damping modification factors used to reduce seismic demand is carried out in Chapter IV of this thesis.

Effective properties, required for response spectrum analysis, are calculated from force-displacement constitutive curves, measured in non-destructive tests. In the early phases of a project, *prototype tests* need to be performed in two real-size specimens of each isolator type and size to determine isolators' design properties. For properties assessment, three complete deformation cycles are performed at different shear-strain levels under the expected vertical load. The effective properties are calculated for each cycle, and the specimens are accepted if properties show a small dispersion among cycles and specimens. Based on the same prototype test results, upper-bound and lower-bound effective stiffness and damping are calculated for design purposes. *Quality control tests* are required for every installed isolator to ensure compatibility with the isolation system properties determined in the prototype tests.

Provisions of NCh2745 [8] are based on the Uniform Building Code (UBC) [7] from California, United States. UBC provisions have evolved to the current provisions in ASCE/SEI 7-16 [33], which present a more rational approach to quantifying and propagating the uncertainty in isolator's properties. Unlike concrete or steel production, there are no standards defining how an isolator must be manufactured. Every provider has its (probably proprietary) methodology using non-traditional civil engineering materials as elastomers and lead. It is highly expected to observe a vast difference in isolators' quality and performance, even for identical specimens from different manufacturers.

To consider this uncertainty, ASCE/SEI 7-16 requires the assessment of seismic response using upper-bound and lower-bound force-displacement curves defined through property modification factors  $\lambda$ . The report from McVitty and Constantinou [34] explains in detail the rationale behind the  $\lambda$  factors suggested in the provisions and serves as a guide for their calculation when required.

The actual properties of the isolator system will vary over the structure life span, meaning that the isolators properties under the design earthquake load could be different from the properties determined from *prototype tests*, due to three uncertainty sources: (i) the date of the earthquake that determines the state of the isolator given the aging and environmental effects; (ii) the internal heating, strain rate and scragging effects that modify the constitutive relationship during the earthquake; and (iii) isolator geometric dimensions that can be different from the prototype specimens. Based on the listed uncertainty sources, ASCE/SEI 7-16 defines three modification factors:  $\lambda_{ae}$ , accounting for aging and environmental effects,  $\lambda_{test}$ , accounting for heating, strain rate and scragging, and  $\lambda_{spec}$ , accounting for manufacturing variations. For each uncertainty source, maximum and minimum values of  $\lambda$

are defined and rationally combined to calculate  $\lambda_{max}$  and  $\lambda_{min}$ . It should be noted that the simple multiplication of the three  $\lambda$  factors will be too conservative as these effects are not expected to present their maximum deviations simultaneously.

The report of McVitty and Constantinou [34] assumes that most of the currently installed seismic isolation devices are: (i) low-damping rubber bearings (LDRBs), (ii) lead-core rubber bearings (LRBs), and (iii) friction pendulums (FPS), being all these isolators suitable to be modeled with a bilinear constitutive. This assumption neglects many high damping rubber bearings (HDRBs) currently installed and exhibiting a noticeable hardening effect. The authors of the report state: "Even with the most complex models, which can explicitly account for some property variations (i.e. instantaneous temperature, velocity, axial load, etc.), there will likely always be a need to perform bounding analysis in order to account for the effects of aging and specification tolerance, since these factors are not captured by mathematical models." As HDRBs are not referenced explicitly in the code or the report, there is no clarity on how these property modification factors should affect the assumed HDRB constitutive relationship. A detailed analysis of the uncertainty of the measured-by-test isolators' properties is presented in Chapter III of this research work. The results of that chapter are closely related to the property modification factor  $\lambda_{test}$  in ASCE/SEI 7-16.

Based on the declared uncertainty sources, ASCE/SEI 7-16 [33] has updated the testing requirements, mandating qualification, prototype, and production (quality control in NCh2745 nomenclature) tests. Typical testing procedures that can be traced back to outdated documents require quasi-static testing; however, this newer version of the code recommends implementing dynamic tests to quantify velocity depending effects, especially in friction-based devices.

#### I.4 Objectives and organization of the thesis

The mechanical behavior of elastomeric seismic bearings presents several complexities, primarily due to the rubber's organic origin and the high levels of lateral displacement to which these devices are subjected. However, the currently implemented code-design provisions are oversimplified and neglect relevant features of the elastomeric bearing's behavior. Additionally, the effective properties used in seismic codes are treated as deterministic despite their inherent uncertainties. These uncertainties need to be quantified and properly propagated to seismic response estimation. This research's main hypothesis states: *"the uncertainty quantification of elastomeric bearings properties and the propagation of these uncertainties to seismic response assessment will lead to a more rational design procedure."* The effects of these uncertainties in the elastomeric bearings modeling techniques and the bearing-induced damping ratio are tackled in this research work, covering topics related to isolators (Chapter II and III) and seismic demand (Chapter IV).

The following research questions will contribute to validating the hypothesis, and their answers are pursued in this work: (i) Is it possible to develop a practitioner-oriented modeling approach that permits to efficiently represent the force-displacement constitutive relationship of different types of seismic isolators to select a particular type of isolator for a given project?; (ii) Could this newly developed modeling approach consider the relevant hardening effect in elastomeric isolators that is currently neglected by design procedures?; (iii) Is it possible to improve some of the assumptions made in the equivalent lateral force and response spectrum methods, currently used to design isolated structures?; (iv) Which

are the uncertainty levels of the isolators' effective properties calculated from measured-by-test force-displacement curves? These research questions are answered following three avenues of research: (i) the development of a versatile and simplified practitioner-oriented element for modeling the seismic response of different types of seismic isolators; (ii) the uncertainty quantification of the elastomeric isolators measured-by-test effective properties; and (iii) the quantification of the damping effect on the seismic response of structures with damping levels different from 5%.

This thesis is written as three independent journal articles. Chapter IV: *The Effect of Spectral Shape on Damping Modification Factors* has already been published in *Earthquake Spectra* (<https://doi.org/10.1177/8755293020936691>), Chapter II: *A Simplified and Versatile Element Model for Seismic Isolation Bearings* was submitted to *Earthquake Spectra* (currently under review), and Chapter III: *Uncertainty on Measurement of Elastomeric Isolators Effective Properties* was submitted to *Measurement* (currently under review).

The first phase of this research focuses on modeling the seismic isolators' nonlinear force-displacement constitutive relationship in response history analysis. As the presented literature review reveals, a considerable gap exists between the research-oriented modeling techniques and the engineering design procedures. A practitioner-oriented element model capable of accurately representing the behavior of different types of seismic isolators is proposed. The model is based on the widely used Menegotto-Pinto [35] model, initially developed for modeling reinforcing bars in reinforced concrete but includes an additional term to model elastomeric isolators' hardening effect. It was calibrated using experimental data from quasi-static cyclic tests and earthquake simulation tests. The model parameters

were identified using different objective functions. Results showed that the model can considerably improve the seismic response estimation with a reasonable additional effort.

This thesis's second phase aims to quantify the uncertainty of elastomeric isolators' effective properties assessed from measured-by-test force-displacement curves. In these tests, effective properties (stiffness  $k_{eff}$  and damping  $\beta_{eff}$ ) are calculated by averaging values for several repeated deformation cycles. Even though these average values are intrinsically random, they are considered deterministic in the engineering design process. In this chapter of the thesis, the *GUM Guide to the expression of uncertainty in measurement* [36], a well-known metrology procedure, is implemented to assess isolators' properties uncertainties. *GUM* estimates the variance of the effective properties, using a first-order Taylor polynomial approximation, from the uncertainties of the quantities directly measured during the test, i.e., forces and displacements. After implementing the *GUM* methodology, supplementary Monte-Carlo simulations were performed to confirm *GUM* estimates. This procedure was applied to an extensive database of elastomeric isolators' test results, then some general trends regarding the uncertainty levels of these properties were identified.

Finally, the third stage of this Doctoral investigation focuses on the equivalent lateral force and the response spectrum procedures used in the design of seismically isolated structures. In both approaches, the 5% damped seismic demand is corrected to account for isolators' additional energy dissipation using damping modification factors  $\eta$ , currently specified in most seismic codes [31,33]. As has been extensively reported in the literature, these damping modification factors  $\eta$  are strongly dependent on damping level, period of vibration, earthquake magnitude, and earthquake duration. However, several seismic codes only consider the damping dependence [33,37] or the damping and vibration period dependence

[31] but neglect the earthquake magnitude and duration effects. The main novelty in this study is the evaluation of two recently developed spectral shape metrics, *SaRatio* [38] and epsilon ( $\epsilon$ ) [39], as predictors for damping modification factor  $\eta$ .

The elastomeric isolators' prototype and quality control test results used in this research were generously shared by the "Laboratory for dynamic testing and vibration control" at Pontificia Universidad Catolica de Chile. Additionally, for the damping modification factor regression analyses, the ground motion records were provided by the SIBER-RISK project.

## REFERENCES

1. Makris N. Seismic isolation: Early history. *Earthquake Engineering and Structural Dynamics* 2019; **48**(2): 269–283. DOI: 10.1002/eqe.3124.
2. Clemente P. Seismic isolation: past, present and the importance of SHM for the future. *Journal of Civil Structural Health Monitoring* 2017; **7**(2): 217–231. DOI: 10.1007/s13349-017-0219-6.
3. Kelly JM, Konstantinidis DA. *Mechanics of Rubber Bearings for Seismic and Vibration Isolation*. 2011. DOI: 10.1002/9781119971870.
4. Eriksen KB, Mohammed MS, Coria CB. Seismic isolation in North and South America. *2018 NZSEE Conference*, 2018.
5. Moroni MO, Sarrazin M, Boroschek R. Experiments on a base-isolated building in Santiago, Chile. *Engineering Structures* 1998; **20**(8): 720–725. DOI: 10.1016/S0141-0296(97)00086-2.
6. De la Llera JC, Luders C, Leigh P, Sady H. Analysis, testing, and implementation of seismic isolation of buildings in Chile. *Earthquake Engineering and Structural Dynamics* 2004; **33**(5): 543–574. DOI: 10.1002/eqe.360.
7. ICBO. Uniform Building Code - Division IV - Earthquake Regulations for Seismic-

- Isolated Structures. International Conference of Building Officials, Whittier, California, 1997.
8. Instituto Nacional de Normalización (INN). *NCh2745.Of2003 - Análisis y diseño de edificios con aislación sísmica (In Spanish)*. 2003.
  9. Almazán JL. Comportamiento de estructuras antisísmicas durante el terremoto del maule y su posible efecto en las normas de diseño sísmico en Chile. *Revista Sul-Americana de Engenharia Estrutural* 2010; **3**(2): 4–28.
  10. Moroni MO, Sarrazin M, Soto P. Behavior of instrumented base-isolated structures during the 27 February 2010 Chile earthquake. *Earthquake Spectra* 2012; **28**(SUPPL.1): 407–424. DOI: 10.1193/1.4000041.
  11. Rendel M, Luders C, Greer M, Vial I, Westenek B, de la Llera J, *et al.* Retrofit, using seismic isolation, of the heavily damaged Basílica del Salvador in Santiago, Chile. *Proceedings of the 14th New Zealand Society for Earthquake Engineering. Aotea, New Zealand*, 2014.
  12. Mullins L. Softening of rubber by displacement. *Rubber Chemistry and Technology* 1969; **42**(1): 339–362.
  13. Maureira N, de la Llera J, Oyarzo C, Miranda S. A nonlinear model for multilayered rubber isolators based on a co-rotational formulation. *Engineering Structures* 2017; **131**: 1–13. DOI: 10.1016/j.engstruct.2016.09.055.
  14. Simo JC, Kelly JM. Finite element analysis of the stability of multilayer elastomeric bearings. *Engineering Structures* 1984; **6**(3): 162–174. DOI: 10.1016/0141-0296(84)90044-0.
  15. Amin a. F, Wiraguna SI, Bhuiyan a. R, Okui Y. Hyperelasticity Model for Finite Element Analysis of Natural and High Damping Rubbers in Compression and Shear. *Journal of Engineering Mechanics* 2006; **132**(1): 54–64. DOI: 10.1061/(ASCE)0733-9399(2006)132:1(54).
  16. Ohsaki M, Miyamura T, Kohiyama M, Yamashita T, Yamamoto M, Nakamura N.

- Finite-element analysis of laminated rubber bearing of building frame under seismic excitation. *Earthquake Engineering and Structural Dynamics* 2015. DOI: 10.1002/eqe.2570.
17. Wen YK. METHOD FOR RANDOM VIBRATION OF HYSTERETIC SYSTEMS. *ASCE J Eng Mech Div* 1976.
  18. Ozdemir H. Nonlinear transient dynamic analysis of yielding structures. University of California, Berkeley, California, 1976.
  19. Kikuchi M, Aiken ID. An analytical hysteresis model for elastomeric seismic isolation bearings. *Earthquake Engineering and Structural Dynamics* 1997; **26**(2): 215–231. DOI: 10.1002/(SICI)1096-9845(199702)26:2<215::AID-EQE640>3.0.CO;2-9.
  20. Grant DN, Fenves GL, Whittaker AS. Bidirectional modelling of high-damping rubber bearings. *Journal of Earthquake Engineering* 2004; **8**: 161–185. DOI: 10.1080/13632460409350524.
  21. Yamamoto S, Kikuchi M, Ueda M, Aiken ID. A mechanical model for elastomeric seismic isolation bearings including the influence of axial load. *Earthquake Engineering and Structural Dynamics* 2009. DOI: 10.1002/eqe.847.
  22. Kikuchi M, Nakamura T, Aiken ID. Three-dimensional analysis for square seismic isolation bearings under large shear deformations and high axial loads. *Earthquake Engineering & Structural Dynamics* 2010. DOI: 10.1002/eqe.1042.
  23. Gjorgjiev I, Garevski M. A polynomial analytical model of rubber bearings based on series of tests. *Engineering Structures* 2013; **56**: 600–609. DOI: 10.1016/j.engstruct.2013.04.006.
  24. Markou AA, Manolis GD. Mechanical models for shear behavior in high damping rubber bearings. *Soil Dynamics and Earthquake Engineering* 2016; **90**: 221–226. DOI: 10.1016/j.soildyn.2016.08.035.
  25. Oliveto ND, Markou AA, Athanasiou A. Modeling of high damping rubber bearings

- under bidirectional shear loading. *Soil Dynamics and Earthquake Engineering* 2019; **118**(February 2018): 179–190. DOI: 10.1016/j.soildyn.2018.12.017.
26. Miranda S, Miranda E, Carlos de la Llera J. A simplified and versatile element model for seismic isolation bearings. *Submitted to Earthquake Spectra* 2020.
  27. Tsopelas P, Constantinou M, Reinhorn A. *3D-BASIS-ME: computer program for non-linear dynamic analysis of seismically isolated single and multiple structures and liquid storage tanks. Technical report NCEER-94-0010*. 1994.
  28. Hwang JS, Wu JD, Pan TC, Yang G. A mathematical hysteretic model for elastomeric isolation bearings. *Earthquake Engineering and Structural Dynamics* 2002; **31**(4): 771–789. DOI: 10.1002/eqe.120.
  29. Yuan Y, Wei W, Tan P, Igarashi A, Zhu H, Iemura H, *et al.* A rate-dependent constitutive model of high damping rubber bearings: modeling and experimental verification. *Earthquake Engineering and Structural Dynamics* 2016. DOI: 10.1002/eqe.2744.
  30. Markou AA, Oliveto ND, Athanasiou A. Modeling of High Damping Rubber Bearings. In: Sextos AG, Manolis GD, editors. *Dynamic Response of Infrastructure to Environmentally Induced Loads: Analysis, Measurements, Testing, and Design*, Cham: Springer International Publishing; 2017. DOI: 10.1007/978-3-319-56136-3\_7.
  31. Instituto Nacional de Normalización (INN). *NCh2745.Of2013 - Análisis y diseño de Edificios con Aislación Sísmica (In Spanish)*. 2013.
  32. Anil K. Chopra. *Dynamics of Structures Theory and Applications to Earthquake Engineering*. Fourth Edi. Prentice Hall; 2012.
  33. American Society of Civil Engineers (ASCE). *Minimum Design Loads for Buildings and Other Structures, ASCE/SEI 7-16*. 2017.
  34. McVitty W, Constantinou M. *Property Modification Factors for Seismic Isolators: Design Guidance for Buildings - Technical Report MCEER-15-0005*. 2015.
  35. Menegotto M, Pinto PE. Method of Analysis for Cyclically Loaded R. C. Plane

Frames Including Changes in Geometry and Non-Elastic Behavior of Elements under Combined Normal Force and Bending. *Proceedings of IABSE Symposium on Resistance and Ultimate Deformability of Structures Acted on by Well Defined Loads* 1973: 15–22. DOI: <http://dx.doi.org/10.5169/seals-13741>.

36. BIPM, IEC, IFCC, ILAC, ISO, IUPAC I and O. Guide to the Expression of Uncertainty in Measurement, JCGM 100:2008 (GUM 1995 with minor corrections). *International Organization for Standardization Geneva ISBN 2008*.
37. Instituto Nacional de Normalización (INN). *NCh2369.Of2013 - Diseño sísmico de estructuras e instalaciones industriales (In Spanish)*. 2013.
38. Eads L, Miranda E, Lignos D. Spectral shape metrics and structural collapse potential. *Earthquake Engineering and Structural Dynamics*, 2016. DOI: 10.1002/eqe.2739.
39. Baker JW, Cornell CA. Spectral shape, epsilon and record selection. *Earthquake Engineering and Structural Dynamics* 2006; **35**(9): 1077–1095. DOI: 10.1002/eqe.571.

## II. A SIMPLIFIED AND VERSATILE ELEMENT MODEL FOR SEISMIC ISOLATION BEARINGS

Sebastián Miranda,<sup>a), c)</sup> M.EERI, Eduardo Miranda,<sup>b)</sup> M.EERI and Juan Carlos de la Llera,<sup>a)</sup> M.EERI.

### II.1 Abstract

A general-purpose simplified model for seismic isolation bearings is developed. The model considers three springs in parallel, namely: i) an elastoplastic spring with a smooth transition between branches; ii) a linear elastic spring; and iii) a non-linear elastic spring. The model is defined by only six parameters, which can be easily calibrated from cyclic tests. The main advantages of the simplified model are twofold: 1) Versatility, as a single model is capable of reproducing well the behavior of different types of seismic isolators including high damping rubber bearings (HDRB), lead - core rubber bearings (LRB) and simple friction pendulums (FPS); and 2) Simplicity, as it requires fewer parameters than most currently available models, which can be easily obtained from experimental cyclic tests. These advantages of the proposed model are illustrated by parameter calibration using quasi-static cyclic and earthquake simulator tests of various types of isolators showing good agreement

---

<sup>a)</sup> National Research Center for Integrated Natural Disaster Management, CONICYT/FONDAP/15110017, Faculty of Engineering, Pontificia Universidad Católica de Chile, Chile

<sup>b)</sup> John A. Blume Earthquake Engineering Center, Department of Civil and Environmental Engineering, Stanford University, Stanford, CA 94305-4020, U.S.A.

<sup>c)</sup> School of Engineering, Universidad del Desarrollo, Chile

between experimental and model results. Additionally, different objective functions are used for model calibration, and their effect on the identified parameters is studied and discussed. This practitioner-oriented model is particularly amenable for implementation in general-purpose structural analysis software.

## **II.2 Introduction**

Seismic isolation has shown to be one of the most effective, and sometimes economical, seismic protection technology. In particular, it is one of the few protection systems that, when adequately implemented, can simultaneously achieve significant reductions in interstory drift demands, horizontal accelerations, and lateral forces in buildings. For the selection of the type of bearing as well as for its characteristics that will result in an adequate control of lateral force and deformation demands in the superstructure, it is necessary to explicitly model their cyclic behavior. In particular, in the context of applications in engineering practice, the words of George E. Box resonate (Box et al., 2011): "all models are wrong, but some models are useful." The author added in the second edition of his book that the question to ask was not if the model is exact (it never is) but just if the model is good enough to produce useful results for a particular application.

Among the different types of seismic isolators, the ones manufactured from high damping rubber (HDRB, high damping rubber bearings) and the ones with a lead-core in their center (LRB, lead-core rubber bearings) have a force-displacement relationship strongly non-linear, especially at large lateral shear strains where alignment of polymeric chains and crystallization in the rubber make the material considerably stiffer. Additionally, these types of isolators have several other well-known characteristics such as: (i) Mullins effect (Mullins

1969) that produces degradation of the peak lateral force and lateral stiffness when the isolation bearing is subjected to cyclic loading; (ii) axial load dependency; (iii) strain-rate dependency; (iv) load-path dependency; and (v) internal temperature dependency.

Kikuchi and Aiken (1997) described how seismic isolators had been modeled to that date. Typically, a Ramberg-Osgood (Ramberg and Osgood 1943) or a bilinear constitutive model were used. However, to adequately model the behavior of the isolators, the bearing parameters need to be updated as a function of shear strain. According to the authors, that methodology was suitable for low-to-moderate shear strains, but it did not capture the stiffening effect on rubber-based isolators subjected to large shear strains. As described below, similar modeling approaches have considered the implementation of the Ozdemir (Ozdemir 1976) or the Wen (Wen 1976) constitutive relationships. These models use a differential equation to track the current state of the isolator, and hence, the model parameters do not need to be updated.

After assessing the accuracy of several formulations available to that date, Kikuchi and Aiken (1997) proposed a new set of equations, characterizing the force in the isolator as a function of shear strain. The Kikuchi and Aiken model, which does not consider differential equations for tracking the isolator current state, showed a much better agreement with the experimental data than many other models, especially if hardening effects were present in the high shear strain range. The Kikuchi and Aiken model requires the calibration of six parameters and the definition of the skeleton curves, all of them typically defined as a function of the isolator shear strain, and considers a simplified procedure to incorporate stiffness degradation that occurs as the deformation cycles evolve.

Pang and Yang (1996) proposed a model that explicitly splits the isolator force in a restoring component, and in a damping component, where the restoring and damping parts are non-linear functions of the isolator displacement and velocity. Hwang et al. (2002) improved the Pang and Yang (1996) model by including the degradation of the stiffness and the dissipated energy as the deformation cycles evolve, and by simplifying the model mathematical formulation as the number of parameters to calibrate was reduced from eleven to ten.

Tsai et al. (2003) recognized that the second generation of models, including the Kikuchi and Aiken (1997) model, effectively included the stiffening effect, but there was still the necessity of more straightforward approaches capable of including, for example, the HDRB strain rate-dependency. The authors proposed a model based on the Bouc-Wen (Wen 1976) constitutive model, modified to include this effect.

Abe et al. (2004) proposed a model capable of considering multiaxial loading, based on the Ozdemir (Ozdemir 1976) elastoplastic model, that also uses differential equations for tracking the state of the system. The Abe et al. model also includes an isotropic hardening displacement-dependent term and a non-linear elastic spring. The one-dimensional version of this model requires the calibration of thirteen parameters. The differential equation approach in this type of models has proven to considerably restrict their implementation in engineering design procedures. Table 1 shows a summary of several models and their main features.

All models listed in Table 1 consider, with different approaches, the significant isolator hardening effect at large shear strains. Additionally, some of them include highly complex phenomena as the strain-rate dependency or the stress softening behavior. However, the influence of these phenomena in the seismic response of isolated structures is still being

investigated. In a recent work by Tubaldi et al. (2017), a new model, especially suited for the stress softening effect assessment, was developed. Its implementation on an SDOF system suggested that the usage of a simplified fully scragged condition in seismic isolation modeling leads to a low to moderate overestimation of the displacements under typical seismic conditions. On the other hand, under near-fault seismic conditions, simulations based on a fully scragged condition could lead to nonrealistic large displacements.

Table II-1. Summary of the most frequently used models.

Model	Calibration parameters	Displacement dependency	Differential Equation	Main Features
Tsopelas et al. (1994)	6	No	Yes	<ul style="list-style-type: none"> <li>• Biaxial behavior</li> <li>• Does not consider cyclic softening effect.</li> </ul>
Pan and Yang (1996)	11	No	No	<ul style="list-style-type: none"> <li>• Uniaxial behavior</li> <li>• Does not consider cyclic softening effect.</li> </ul>
Kikuchi and Aiken (1997)	8	Yes	No	<ul style="list-style-type: none"> <li>• Uniaxial behavior</li> <li>• Considers cyclic softening effect.</li> </ul>
Hwang et al. (2002)	10	No	No	<ul style="list-style-type: none"> <li>• Uniaxial behavior</li> <li>• Considers cyclic softening effect.</li> </ul>
Tsai et al. (2003)	7	No	Yes	<ul style="list-style-type: none"> <li>• Biaxial behavior</li> <li>• Considers rate-dependency effects.</li> </ul>
Abe et al. (2004)	13	No	Yes	<ul style="list-style-type: none"> <li>• Biaxial behavior</li> <li>• Considers isotropic hardening.</li> </ul>

Table 1 shows that most of the existing models require a relatively large number of parameters, which are often hard to calibrate, for example, in models in which these

parameters are not constants, but functions that depend on the shear strain in the isolator. Most of these models are research-oriented, and therefore have not been implemented in commercially available structural analysis programs nor they are used in practice for evaluating the seismic response of isolated structures. On the other hand, most seismic regulatory codes use quite simplified design methodologies based on an equivalent linearization of the isolators' force-displacement relationship, neglecting significant effects that certainly should be considered in the design or just make reference to very simple non-linear models such as bilinear models that neglect some features such as hardening that may not lead to an adequate estimate of lateral forces and accelerations on the structure. The proposed simplified model is aimed at capturing the main features of many types of isolation bearings, such as being able to represent with reasonable accuracy the hardening effect present in many of the currently installed rubber-based seismic isolators, with a formulation significantly simpler when compared with the other models available in the literature.

The main objectives of this research are: (1) to propose a simplified and versatile practitioner-oriented model, able to capture relevant features of the behavior of seismic isolators that currently are not considered by the standard design procedures; (2) to demonstrate that the model is capable of representing with reasonable accuracy the measured behavior of different types of seismic isolators when subjected to quasi-static cyclic loading and earthquake simulation tests; (3) to study if the parameters that define the model need to be defined as a function of the isolator shear strain or could be defined as constants; (4) to identify the model parameters using system identification techniques combined with different objective functions minimizing error in dissipated energy, force history, and

stiffness history during a deformation cycle; and (5) to study the sensitivity of the model-predicted response to the objective function used to perform the parameter calibration.

### II.3 Analytical Model

The simplified model is based on several aspects of the Kikuchi-Aiken model but makes several modifications that make it more versatile and easier to calibrate. Similarly to the Kikuchi-Aiken model, the proposed simplified model is based on several springs arranged in parallel. One of them has a hysteretic behavior based on the well-known Menegotto-Pinto model (Menegotto and Pinto 1973) initially developed for modeling steel reinforcing bars used in reinforced concrete. The Menegotto-Pinto model is characterized by four parameters: (i)  $F_y$ , the yield force; (ii)  $u_y$ , the yield displacement; (iii)  $R$ , a parameter that controls the shape of the transition between the elastic and the plastic branches; and (iv)  $b$  the ratio of the secondary and initial stiffness. In steel modeling, the  $R$  parameter is used to represent the Bauschinger effect (Bauschinger, 1881), and its value is typically a function of the maximum inelastic displacement experienced by the steel specimen.

The Menegotto-Pinto model can be easily interpreted as two springs acting in parallel, namely  $F_1(u)$  and  $F_2(u)$ , where  $F_1$  and  $F_2$  are the forces acting in each spring, and  $u$  is the displacement. As can be seen in Figure 2,  $F_1(u)$  is an elastoplastic spring with a smooth transition between its branches, and  $F_2(u)$  is a linear elastic spring.

To include the hardening effect that characterizes isolators' response when subjected to moderate and high levels of lateral shear strain, a non-linear elastic spring, namely  $F_3(u)$ , is included. This non-linear spring is defined by two parameters: (i)  $u_h$ , the displacement associated with a unitary force  $F_0$ ; and (2)  $n$ , a parameter that controls the nonlinearity of the

spring.  $F_o$  is a constant term defined as one in the considered force units. By adding the contributions of the three springs in the simplified model, the complete equation giving the force as a function of the displacement is given by:

$$F(u) = \frac{\frac{F_y(1-b)u}{u_y} \left(1 + \left(\frac{u}{u_y}\right)^{\frac{1}{R}}\right)^{\frac{1}{R}}}{\left(1 + \left(\frac{u}{u_y}\right)^{\frac{1}{R}}\right)^{\frac{1}{R}}} + \frac{F_y}{u_y} bu + F_o \operatorname{sign}(u) \left(\frac{|u|}{u_h}\right)^n \quad (1)$$

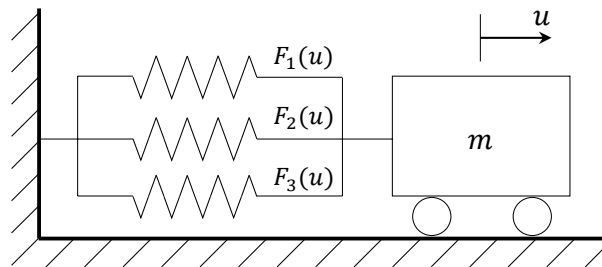


Figure II-1. Proposed analytical model.

Figure 2 shows plots of force as a function of displacement for the three springs in the simplified model. A comparison between the original Menegotto-Pinto model and the proposed model which incorporates  $F_3(u)$  to account for hardening effects is shown in Figure 3.

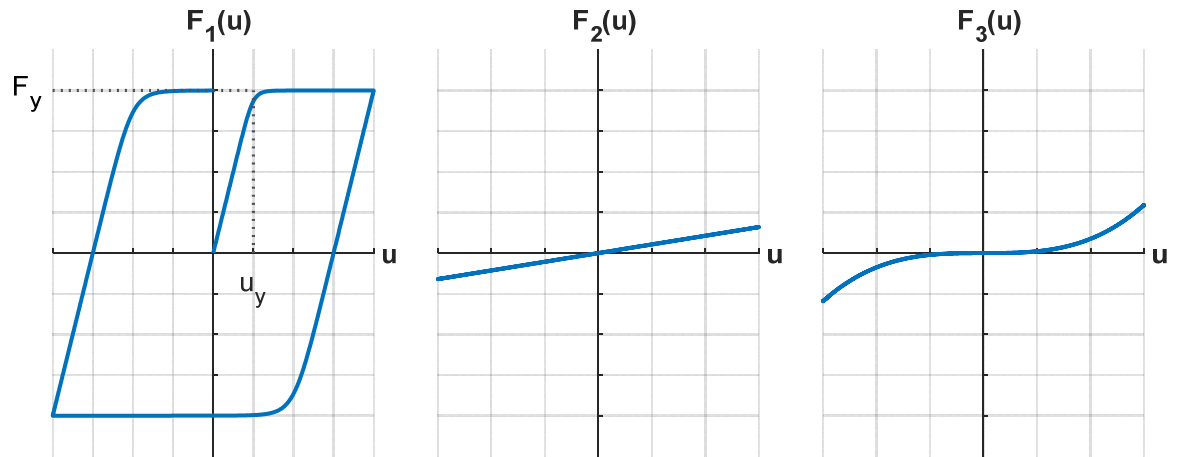


Figure II-2. Force as a function of displacement for the three springs in the model.

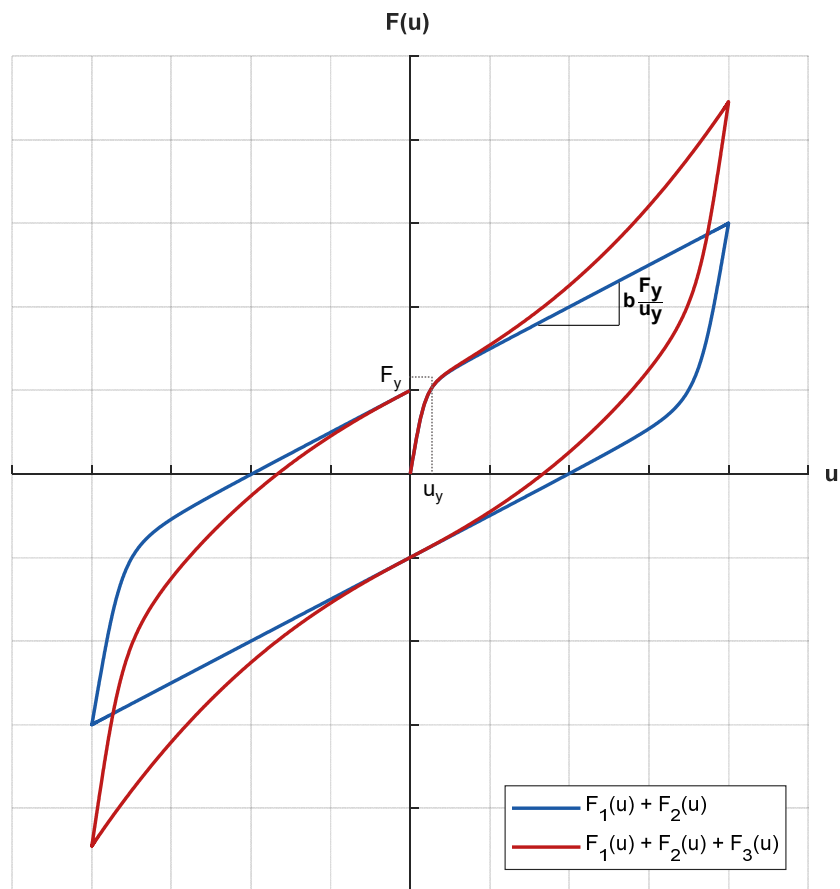


Figure II-3. Force as a function of displacement for: a)  $F_1(u) + F_2(u)$ , the original Menegotto-Pinto Model, and b)  $F_1(u) + F_2(u) + F_3(u)$ , the model proposed in this work.

The parameters defining the springs  $F_1(u)$  and  $F_3(u)$  and the overall effect of their variation on the springs force-displacement constitutive relations are displayed in Figures 4 and 5, respectively. For the  $F_1(u)$  spring case, the plots consider  $b = 0$ .

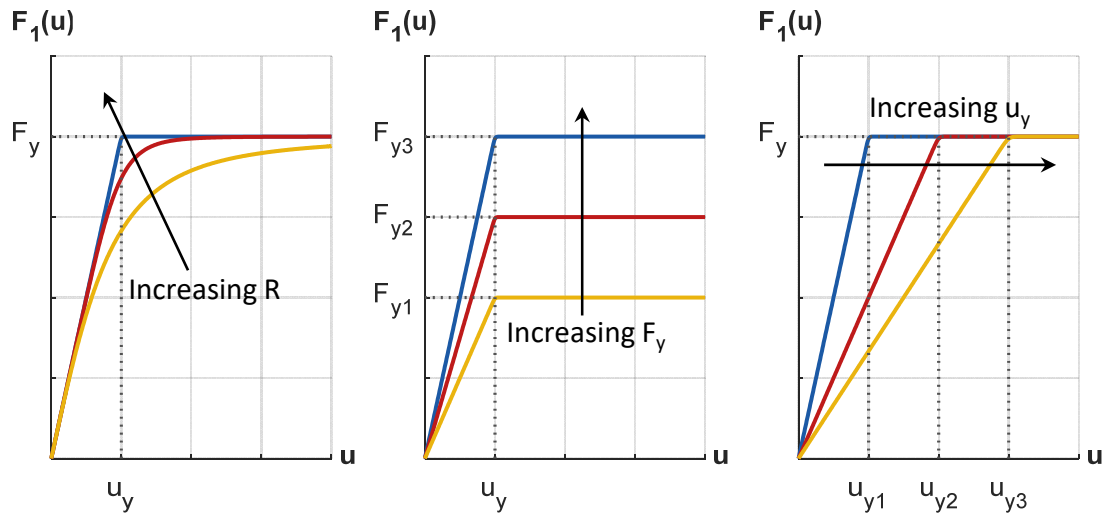


Figure II-4. Effect of variation of different parameters on force  $F_1(u)$  as a function of displacement (when  $b = 0$ )

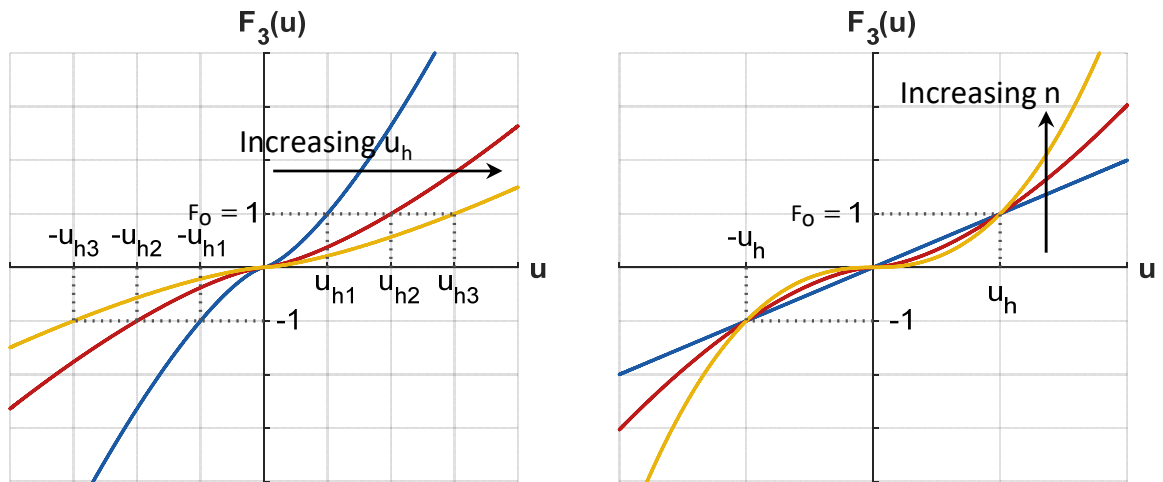


Figure II-5. Effect of variation of different parameters on force  $F_3(u)$  as a function of displacement.

It should be noted that the proposed model converges to the frequently-used kinematic-hardening bilinear model when the parameters  $R$  and  $u_h$  are set to high values (e.g.,  $R \approx 40$  and  $u_h \approx 10 \max |u(t)|$ ). Under these conditions, the  $F_3(u)$  term vanishes to zero and the hardening effect disappears.

As this model is intended for seismic isolator modeling under earthquake loads which involves reverse cyclic loading with varying amplitudes, a set of rules for unloading and reloading for inner cycles needs to be defined. In the original Menegotto-Pinto formulation, when the oscillator reverses its velocity at any displacement level smaller than the maximum displacement already reached during the response, the reloading curve could produce forces higher than the ones associated with the previous loading curve, violating the constraint imposed by the primary skeleton curve. In order to overcome this flaw in the original model, the storage of a previously undefined number of internal loops, generated by the subsequential velocity reversals, was required. These internal loops could be sequentially forgotten as the oscillator displacement exceeds the displacement where the loop was originated.

Ciampi et al. (1982) proposed a simplified procedure to correct this problem in the original Menegotto-Pinto model. This procedure only memorizes four curves, namely: i) the skeleton curve; ii) the ascending curve, starting at the reversal point with the minimum displacement value; iii) the descending curve, starting at the reversal point with the maximum displacement value; and iv) the current curve starting at the last reversal point. Despite its simplicity, this methodology has proven to give reasonably accurate results for modelling reinforcing steel bars subjected to reverse cyclic loading and is then implemented in this simplified model for seismic isolation bearings.

Figure 6 shows the original Menegotto-Pinto model erroneously following the blue line after a velocity reversal point, in this case, a small unloading followed by reloading. The model proposed in this work returns to the ascending curve defined by the reversal point with the minimum displacement. The transition curve after the last reversal point was analytically defined with the methodology proposed by Bosco et al. (2016)

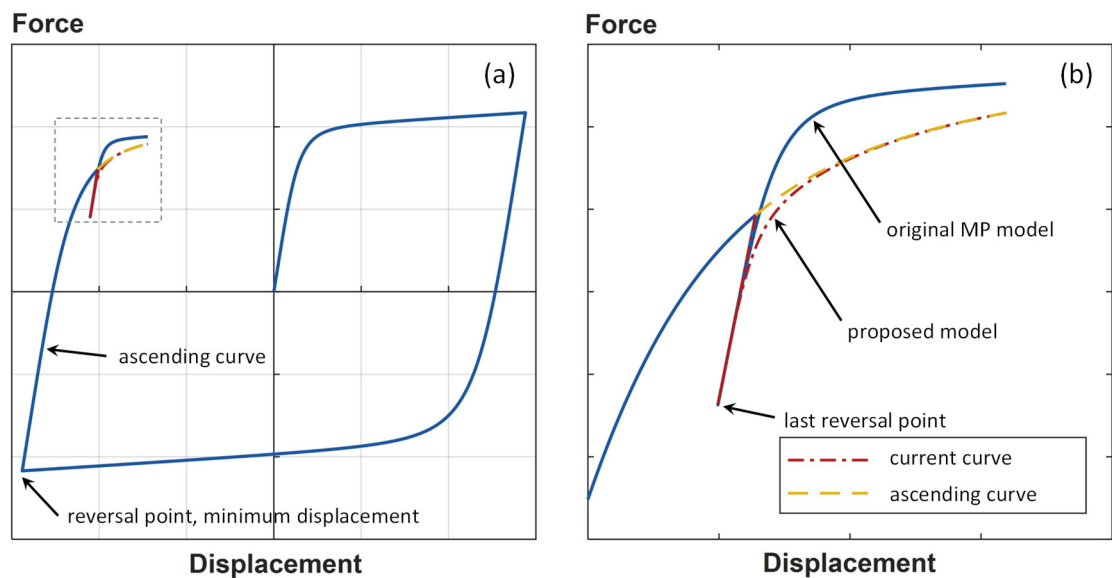


Figure II-6. Proposed rules for seismic unloading and reloading: (a) force as a function of displacement, general view, and (b) reversal point, detailed view.

#### II.4 Model Validation

Two different verifications were implemented to assess the ability of the simplified model to represent the seismic isolator behavior under different load conditions. Firstly, the model was calibrated to fit four cyclic tests of different types of seismic isolators, including high-damping rubber bearings (HDRB) and lead-core rubber bearings (LRB). Secondly, the proposed model was calibrated to fit two earthquake simulator tests of an HDRB isolator

and an LRB isolator. The specimens used to calibrate the model are described in Table 2 and Table 3, for the cyclic tests and the earthquake simulator tests, respectively.

Table II-2. Seismic isolator specimens calibrated through cyclic tests.

Specimen	Type	Geometry	Shear Strains
1	HDRB, Natural rubber compound.	$\phi = 750 \text{ mm}$ $\phi_i = 100 \text{ mm}$ $h_r = 128 \text{ mm}$	$\gamma = 0.50, 1.00, 1.50, 2.00$
2	LRB, Unfilled natural rubber compound	$\phi = 180 \text{ mm}$ $\phi_{lead} = 25 \text{ mm}$ $h_r = 36 \text{ mm}$	$\gamma = 0.85, 1.28, 1.70, 2.60$
3	LRB, Filled Natural rubber compound	$\phi = 750 \text{ mm}$ $\phi_{lead} = 150 \text{ mm}$ $h_r = 204 \text{ mm}$	$\gamma = 0.25, 0.50, 1.0, 1.25$
4	HDRB, Natural rubber compound.	$\phi = 600 \text{ mm}$ $\phi_i = 100 \text{ mm}$ $h_r = 133 \text{ mm}$	$\gamma = 0.25, 0.50, 1.0, 1.50$

Table II-3. Seismic isolator specimens calibrated through earthquake simulator tests

Specimen	Type	Geometry	Calibration Ground Motion
5	HDRB, Natural rubber compound	$\phi = 650 \text{ mm}$ $\phi_i = 100 \text{ mm}$ $h_r = 204 \text{ mm}$	ICA – 2007 Pisco (Peru) PGA = 0.50 g
6	LRB, Unfilled natural rubber compound	$\phi = 180 \text{ mm}$ $\phi_{lead} = 25 \text{ mm}$ $h_r = 36 \text{ mm}$	El Centro – 1940 Imperial Valley PGV = 50 cm/s

## II.5 Cyclic Test Calibration

The parameter calibration was performed using a least-squares approach to minimize the difference between measured and model-predicted response, but different objective functions were used to define different sets of optimal model parameters. Frequently, a minimization of the deviation between the dissipated energy during a deformation cycle and its corresponding model-predicted value is selected as the optimality criterion (e.g., Ibarra et al. 2005). Another approach commonly used when calibrating the model parameters considers minimizing the difference between the forces measured during the test and the model-predicted forces during a given deformation cycle. However, as the dynamic response of an oscillator depends on its tangent stiffness in the integration step under consideration, an objective function that minimizes the deviation in tangent stiffness is especially desirable. To study how the objective function used during the optimization (minimization in this case) influences the model parameters, the cyclic test calibration was performed using five different objective functions, detailed in Table 4. For the objective functions minimizing the

deviation of forces throughout the loading history or when minimizing the deviation of stiffnesses, two different approaches were implemented by computing an absolute difference and a relative difference between the experimental and the model-predicted values.

In the absolute difference case, the sum of the differences (in absolute value) between the measured and the model-predicted values during a deformation cycle is minimized, then the optimization process will tend to generate a better fit in the displacement range where the forces or the stiffnesses are high, as their contribution to the sum for the complete deformation cycle is high. On the other hand, in the relative difference case, the differences (also in absolute value) between the measured and the model-predicted values are normalized by the average between these values. The normalized differences are afterward added for the complete deformation cycle. The optimal parameters obtained through the latter procedure should assure a more consistent agreement between the measured and the model-predicted values for the complete force-displacement curve.

The lateral stiffness was calculated using two different methods: (i) by using an "instantaneous" tangent stiffness, calculated as the force-displacement curve slope between two consecutive sampled values; and (ii) a secant stiffness, calculated as the slope of the force-displacement curve given a fixed displacement increment of 0.25 cm. In most cases, both approaches result in similar optimal parameters, but the extremely high stiffnesses observed for large shear displacements could generate some numerical issues when using the "instantaneous" tangent stiffness approach, then the use of the secant stiffness was implemented.

The complete set of objective functions was used to calibrate the cyclic test results for Specimen 1. This specimen was vulcanized from natural rubber, it is annular-shaped with an

external diameter of 750 mm, an internal diameter of 100 mm, sixteen 8-mm thick rubber layers, and fifteen 3-mm thick steel shims. The cyclic test was performed in the "Laboratory for dynamic testing and vibration control" at Pontificia Universidad Catolica de Chile on July 30th, 2014, under an expected axial load of 447 tonf. This specimen was subjected to a maximum shear strain of  $\gamma = 2.0$ , and the measured effective properties were  $k_{eff} = 1.62 \text{ tonf/cm}$  (effective stiffness) and  $\beta_{eff} = 12.4\%$  (effective damping). For further details on the testing setup, the reader is referred to De la Llera et al. (2014)

The influence of the selected objective function in the robustness of the different optimal parameter sets was assessed through the following steps:

- Different optimal parameter sets ( $a$ ,  $b$ ,  $c$ ,  $d$ , and  $e$ ) were calculated using each objective function described in Table 4.
- For each optimal parameter set, five different calibration errors were calculated using the five error indexes in Table 4.
- The five errors calculated with a specific error index were normalized by the minimum error associated with that index, i.e., the error of the optimal parameter set determined by the minimization of that specific error index.
- The last step was repeated for all the different error indexes defined in Table 4.

Table II-4. Objective functions used to perform parameter calibration

Method	Objective function	Optimal parameter set	Error index used to fit model
1	$\min (E_d^t - E_d^f)$	<i>a</i>	Dissipated energy during a complete deformation cycle, deviation between test-measured and model-fitted values.
2	$\min \sum_i (F_i^t - F_i^f)^2$	<i>b</i>	Force for each sampled displacement, squared absolute deviation between test-measured and model-fitted values.
3	$\min \sum_i \left( \frac{(F_i^t - F_i^f)}{ F_i^t  +  F_i^f } \right)^2$	<i>c</i>	Force for each sampled displacement, squared relative deviation between test-measured and model-fitted values.
4	$\min \sum_i (K_i^t - K_i^f)^2$	<i>d</i>	Secant stiffness for each sampled displacement, squared absolute deviation between test-measured and model-fitted values.
5	$\min \sum_i \left( \frac{(K_i^t - K_i^f)}{ K_i^t  +  K_i^f } \right)^2$	<i>e</i>	Secant stiffness for each sampled displacement, squared relative deviation between test-measured and model-fitted values.

---

where:

$E_d^t = 1/2 \sum_{i=1}^{m-1} (F_{i+1}^t + F_i^t)(u_{i+1} - u_i)$ , total test-measured dissipated energy for a given displacement cycle.

$E_d^f = 1/2 \sum_{i=1}^{m-1} (F_{i+1}^f + F_i^f)(u_{i+1} - u_i)$ , total model-fitted dissipated energy for a given displacement cycle.

$u_i$  = sampled displacement  $i$ , during a cyclic test.

$m$  = total number of sampled displacements during a cyclic test.

$F_i^t$  = test-measured force at step  $i$ , during a cyclic test.

$F_i^f$  = model-fitted force at step  $i$ , during a cyclic test.

$K_i^t$  = test-measured secant stiffness at step  $i$ , during a cyclic test.

$K_i^f$  = model-fitted secant stiffness at step  $i$ , during a cyclic test.

For each optimal set of parameters, that is, those that minimize the five different objective functions, the relative errors of the other four objective functions are shown in Figure 7. The optimal set of parameters  $b$ , determined through minimization of absolute force deviation, shows the smallest variability between relative errors, meaning that the deviation between the test and the model-predicted values is closest, regardless of the error index used to measure this deviation. On the other extreme, for the optimal parameter set  $e$ , determined through minimization of the relative secant stiffnesses, the level of agreement between the test and the model-predicted values depends strongly on which measure of error was used to quantify the deviation between experimental and calculated results. Consequently, for Specimen 1 modeling, the use of optimal parameter set  $b$  is better than using the optimal parameter set  $e$ , as it produces errors using all five measures of deviation that are closer to the minimum values.

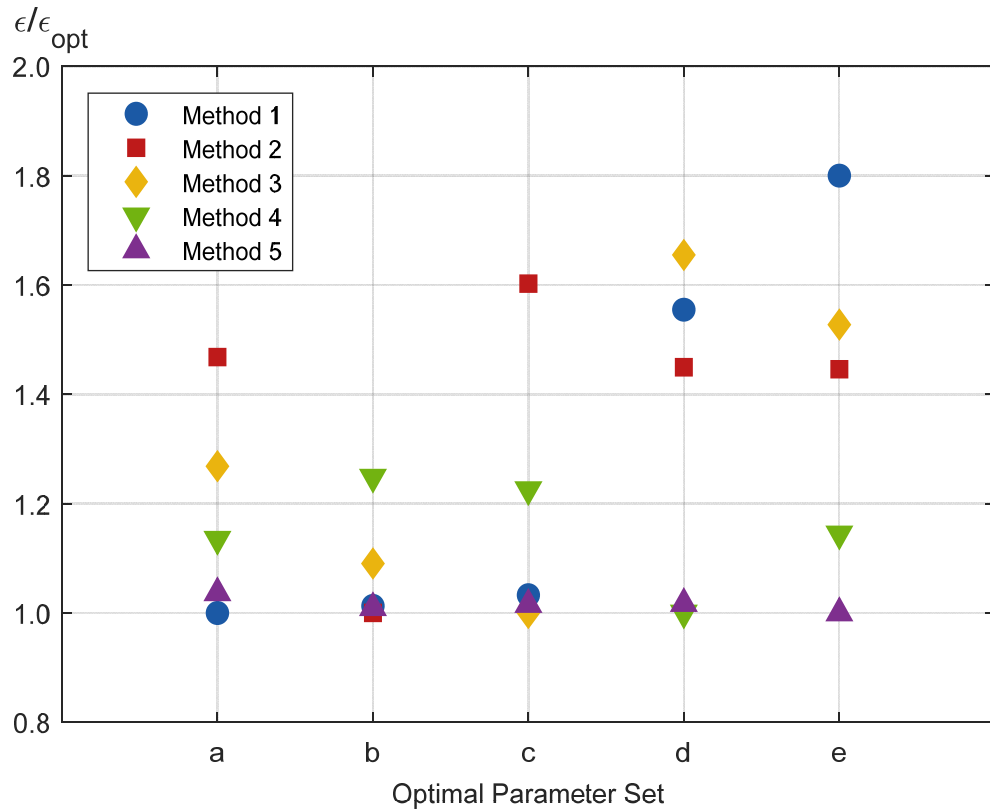


Figure II-7. A comparison of errors calculated using the five objective functions in Table 4 for a given optimal parameter set, normalized to the minimum error for each optimization criterion.

Figure 8 shows schematically for Specimen 1, at a given shear strain of  $\gamma = 2.0$ , how the selection of the objective function influences the optimal parameter set and their associated model-predicted values. When dissipated energy is selected as calibration criterion, the optimization process tends to equalize the areas enclosed by the force-displacement curves, and then some significant differences in lateral stiffness can be observed mainly in the low to moderate displacement cycles. Then, since the solution to the differential equations of motion depends on adequately capturing changes in the lateral tangent stiffness at each integration step, this approach could lead to significant errors in the oscillator seismic response calculation.

Based on the previous comment, an objective function based on minimizing the difference in stiffness between the measured and the model-predicted values, would appear to be the most logical choice. However, the specimen under consideration is strongly characterized by its noticeable hardening in the high displacement range, then a substantial stiffness increase is expected at large displacements. For specimens that exhibit strong hardening, the stiffness can become very large and therefore the use of this objective function, even though the general agreement between the experimental and the model-predicted values is acceptable, will minimize deviations between measured and computed stiffness in this region but may produce larger errors in portions of the hysteretic cycle in which the stiffness is small, which are of interest as those would be producing larger displacement increments. As can be seen in the central plot in Figure 8, when a force deviation minimization criterion is used to define the optimal parameters, the model fits with reasonable accuracy the experimental test data in the complete displacement range under analysis, then the stiffnesses and the non-linear forces predicted by the model are quite similar to the ones in the experimental test. Based on this fact, an absolute force-based error index (Method *b* in Table 4) was selected as the optimization criterion for the rest of this study.

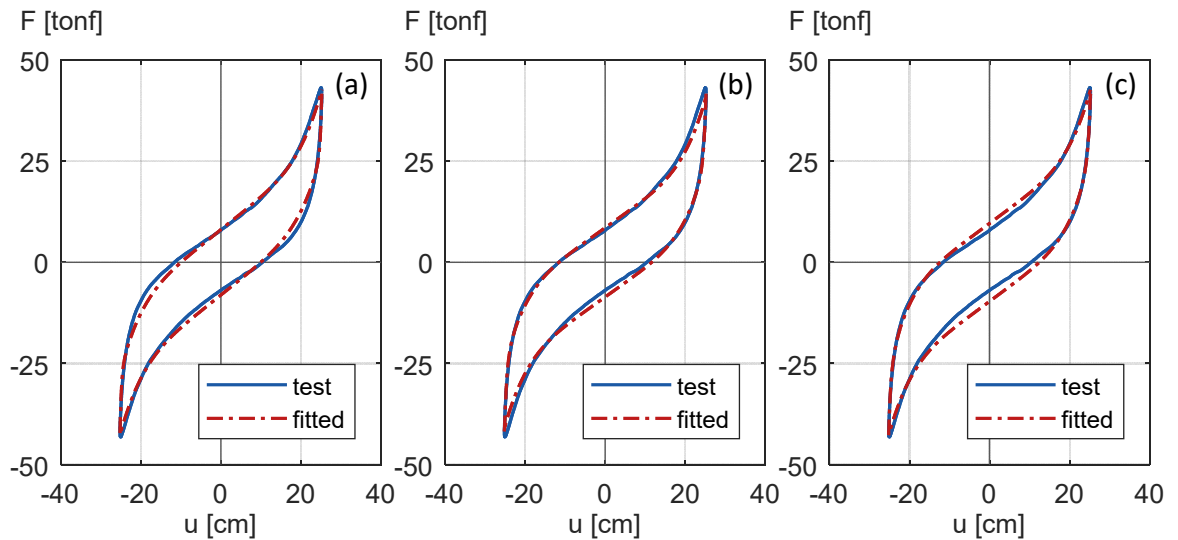


Figure II-8. Comparison of the experimental test data (Specimen 1,  $\gamma = 2.0$ ) and the model-fitted data using different objective functions to identify the optimal set of parameters: (a) dissipated energy deviation minimization; (b) force deviation minimization; and (c) stiffness deviation minimization.

As it has been widely established in the literature (Kikuchi and Aiken 1997), the constitutive models that do not use differential equations on their formulation generally need to update their parameters as a function of the shear strain in the specimen (hereafter referred to as displacement-dependent parameters).

To study how the quality of the fit is affected by this displacement-dependency, a sequential approach was implemented. In the first stage of the optimization process, the model parameters were calibrated independently for each shear strain in the cyclic test, getting the best possible fit and implying that all parameters were displacement-dependent. This allows the identification of the parameters that are more sensitive to the level of deformation.

In the second stage of the optimization procedure, the displacement-dependent parameters were gradually constrained to check displacement-independency, in a sequence that minimized the growth of the fitting error.

Figure 9 shows the experimental and the model-predicted force-displacement curves for the first stage of the calibration procedure when most parameters are assumed displacement-dependent. An excellent agreement between the experimental and the model-predicted data is observed for all specimens under analysis. Optimal parameters are listed in Table 5.

Table II-5. Model-calibrated parameters for all specimens, when the best possible fit is obtained by setting many parameters to be displacement-dependent. (Displacement-dependent parameters are shown in bold characters).

Specimen	$\gamma$	$u$ (cm)	$F_y$ (t/cm <sup>2</sup> )	$u_y$ (cm)	$b$	$R$	$u_h$ (cm)	$n$
1	0.50	6.40	<b>7.79</b>	<b>0.17</b>	<b>0.04</b>	<b>0.65</b>	<b>10.00</b>	4.85
	1.00	12.80	<b>8.78</b>	<b>0.19</b>	<b>0.02</b>	<b>0.69</b>	<b>10.00</b>	4.85
	1.50	19.20	<b>7.90</b>	<b>0.22</b>	<b>0.02</b>	<b>0.93</b>	<b>11.90</b>	4.85
	2.00	25.60	<b>9.12</b>	<b>0.37</b>	<b>0.03</b>	<b>1.94</b>	<b>14.50</b>	4.85
2	0.85	3.06	<b>0.51</b>	<b>0.15</b>	<b>0.07</b>	<b>3.61</b>	10.00	1.00
	1.28	4.61	<b>0.50</b>	<b>0.10</b>	<b>0.04</b>	<b>1.84</b>	10.00	1.00
	1.70	6.12	<b>0.56</b>	<b>0.05</b>	<b>0.01</b>	<b>0.66</b>	10.00	1.00
	2.60	9.36	<b>0.51</b>	<b>0.09</b>	<b>0.02</b>	<b>0.95</b>	10.00	1.00
3	0.25	5.10	<b>80.36</b>	<b>0.83</b>	<b>0.002</b>	<b>0.56</b>	18.00	3.50
	0.50	10.20	<b>64.94</b>	<b>0.50</b>	<b>0.002</b>	<b>0.53</b>	18.00	3.50
	1.00	20.40	<b>28.98</b>	<b>0.37</b>	<b>0.009</b>	<b>0.82</b>	18.00	3.50
	1.25	25.50	<b>21.58</b>	<b>0.26</b>	<b>0.007</b>	<b>0.70</b>	18.00	3.50
4	0.25	3.33	<b>6.88</b>	<b>0.27</b>	<b>0.038</b>	<b>0.39</b>	15.9	6.00
	0.50	6.65	<b>5.77</b>	<b>0.16</b>	<b>0.023</b>	<b>0.39</b>	15.9	6.00
	1.00	13.30	<b>3.32</b>	<b>0.31</b>	<b>0.072</b>	<b>1.56</b>	15.9	6.00
	1.50	19.95	<b>4.03</b>	<b>0.39</b>	<b>0.068</b>	<b>1.95</b>	15.9	6.00

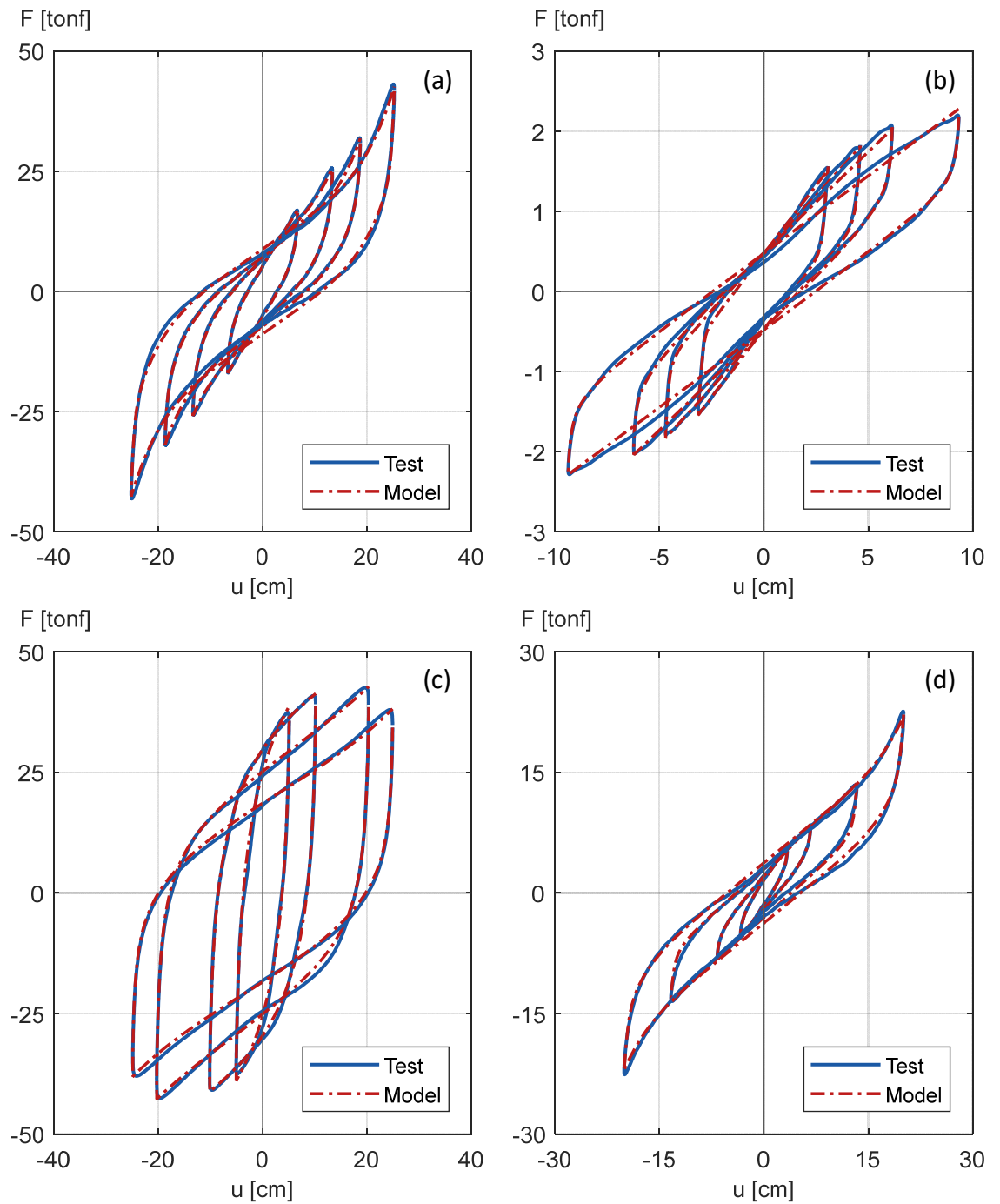


Figure II-9. Experimental test data and best model-fitted data for specimens: (a) 1, (b) 2, (c) 3, and (d) 4, as described in Table 2. The model parameters used in each Specimen are listed in Table 5.

Figure 10 shows the calibration relative error in Specimen 1 as a function of the number of displacement-dependent parameters. This sensitivity analysis was performed for the five objective functions defined in Table 4. The best fit was considered to be the one obtained when five out of six parameters were set to be displacement-dependent, as this case did not show any noticeable decrease in the fit quality when compared with the case where all parameters were considered displacement-dependent. These parameters were sequentially constrained to be displacement-independent (i.e., assuming constant values) to assess how the quality of the fit decreases as the number of displacement-dependent parameters decreases.

For Specimen 1, it can be seen that when setting only two displacement-dependent parameters ( $b$  and  $u_h$ ), the quality of the fit is quite similar to the case with five displacement-dependent parameters, regardless of the objective function used for the optimization, excepting the case where the dissipated-energy objective function was used (Method 1).

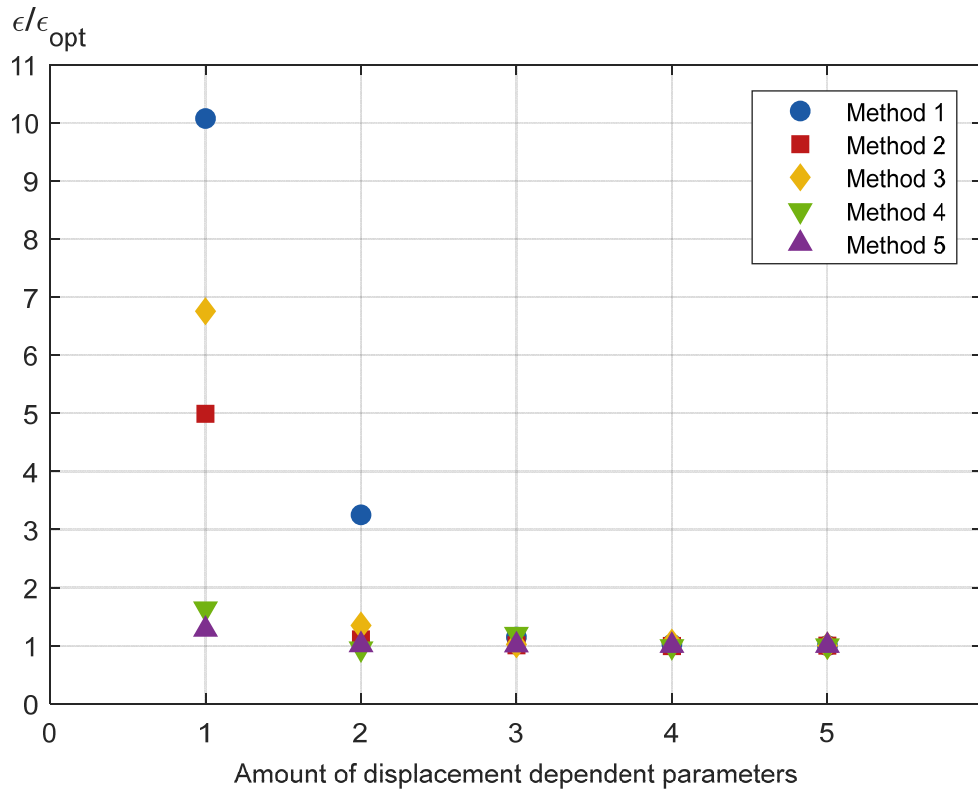


Figure II-10. Model-fitted relative error as a function of the number of displacement-dependent parameters, Specimen 1.

A similar trend between the quality of the fit and the number of displacement-dependent parameters was observed for the other specimens used in this study. Therefore, with the proposed model, generally speaking, there is no need to consider a large number of displacement-dependent parameters to get an accurate analytical prediction. Figure 11 shows the comparison between the experimental and the model-predicted force-displacement curves when only two displacement-dependent parameters are considered for Specimens 1, 2, and 3, and when only one displacement-dependent parameter is considered for Specimen 4. These updated parameter sets are listed in Table 6.

Even though the updated parameters in Table 6 are considerably simpler than the parameters listed in Table 5, the agreement between the test results and the model-predicted values is still entirely satisfactory.

Table II-6. Model-calibrated updated parameters for all specimens. Displacement-dependent parameters are shown in bold characters.

Specimen	$\gamma$	$u$ (cm)	$F_y$ (t/cm <sup>2</sup> )	$u_y$ (cm)	$b$	$R$	$u_h$ (cm)	$n$
1	0.50	6.40	8.40	0.30	<b>0.05</b>	1.05	<b>10.00</b>	4.85
	1.00	12.80	8.40	0.30	<b>0.04</b>	1.05	<b>10.00</b>	4.85
	1.50	19.20	8.40	0.30	<b>0.03</b>	1.05	<b>11.90</b>	4.85
	2.00	25.60	8.40	0.30	<b>0.03</b>	1.05	<b>14.50</b>	4.85
2	0.85	3.06	0.54	0.06	<b>0.02</b>	<b>1.00</b>	10.00	1.00
	1.28	4.61	0.54	0.06	<b>0.02</b>	<b>0.99</b>	10.00	1.00
	1.70	6.12	0.54	0.06	<b>0.02</b>	<b>0.77</b>	10.00	1.00
	2.60	9.36	0.54	0.06	<b>0.01</b>	<b>0.75</b>	10.00	1.00
3	0.25	5.10	<b>55.87</b>	0.49	<b>0.009</b>	0.61	18.00	3.50
	0.50	10.20	<b>53.27</b>	0.49	<b>0.004</b>	0.61	18.00	3.50
	1.00	20.40	<b>39.86</b>	0.49	<b>0.005</b>	0.61	18.00	3.50
	1.25	25.50	<b>27.96</b>	0.49	<b>0.007</b>	0.61	18.00	3.50
4	0.25	3.33	4.13	0.43	0.076	<b>0.75</b>	15.9	6.00
	0.50	6.65	4.13	0.43	0.076	<b>0.73</b>	15.9	6.00
	1.00	13.30	4.13	0.43	0.076	<b>0.81</b>	15.9	6.00
	1.50	19.95	4.13	0.43	0.076	<b>2.31</b>	15.9	6.00

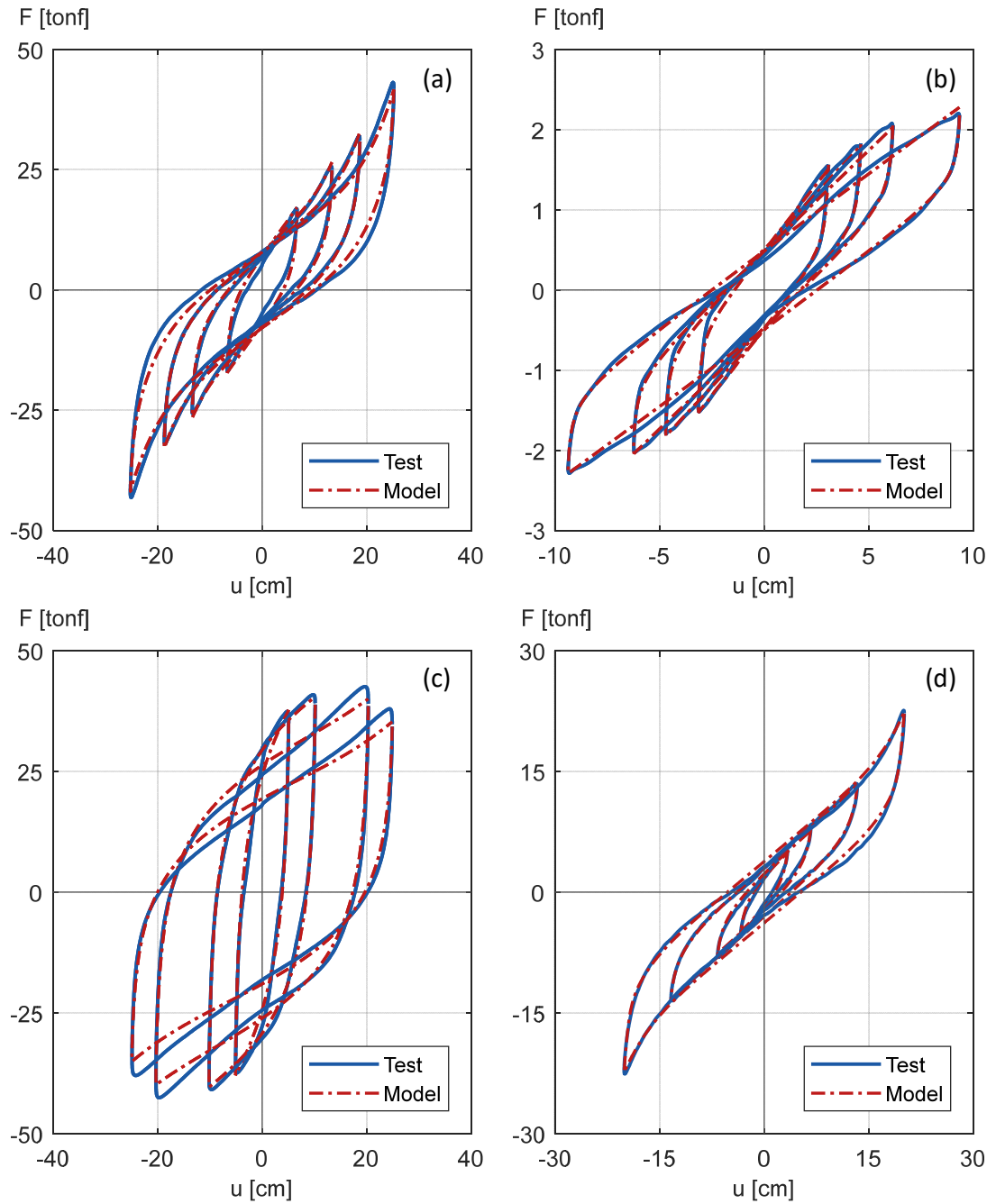


Figure II-11. Experimental test and simplified model-fitted data for: (a) Specimen 1 with  $b$  and  $u_h$  displacement-dependent; (b) Specimen 2 with  $b$  and  $R$  displacement-dependent; (c) Specimen 3 with  $F_y$  and  $b$  displacement-dependent; and (d) Specimen 4 with  $R$  displacement-dependent. The model parameters for each case are listed in Table 6.

## II.6 Earthquake Test Calibration

The capability of the proposed simplified model to adequately represent the force-displacement relationship of different types of seismic isolators under earthquake loads was assessed by comparing its analytically predicted values with the results of two different earthquake simulator tests. In this case, the model parameters were identified as follows:

- As the isolators cyclic test results were available for both cases, an initial and displacement-independent estimation of the six model parameters was performed.
- An analysis of the sequence that best improves the fit quality, by incrementally redefining some parameters as displacement-dependent, was carried out.
- Given parameter  $p_i$  to be updated as displacement-dependent, its identification was performed through a force-error minimization procedure (i.e., Method 2 in Table 4) for the complete earthquake displacement history. In this case, the output of the optimization process is not a single value for the parameter  $p_i$ , but several  $(\gamma, p_i)$  ordered pairs. The selected  $\gamma$  values were arbitrarily defined based on the displacement history of the earthquake ground motion under analysis.

The last step was repeated for the following parameter  $p_j$  selected to be updated as displacement-dependent.

It should be noted that in the case of an earthquake test calibration, a functional form relating the parameter being calibrated with the isolator shear strain needs to be selected, then several functional forms were studied. However, results suggest that the selected functional form does not have a significant effect on the ability of the model to predict the isolator behavior under a given displacement history. Consequently, only two functional forms to describe the

variation of the parameters with changes in the level of strain, were selected based on their simplicity. These functional forms will be hereafter referred to as FF1 and FF2 and are displayed in Figure 12.

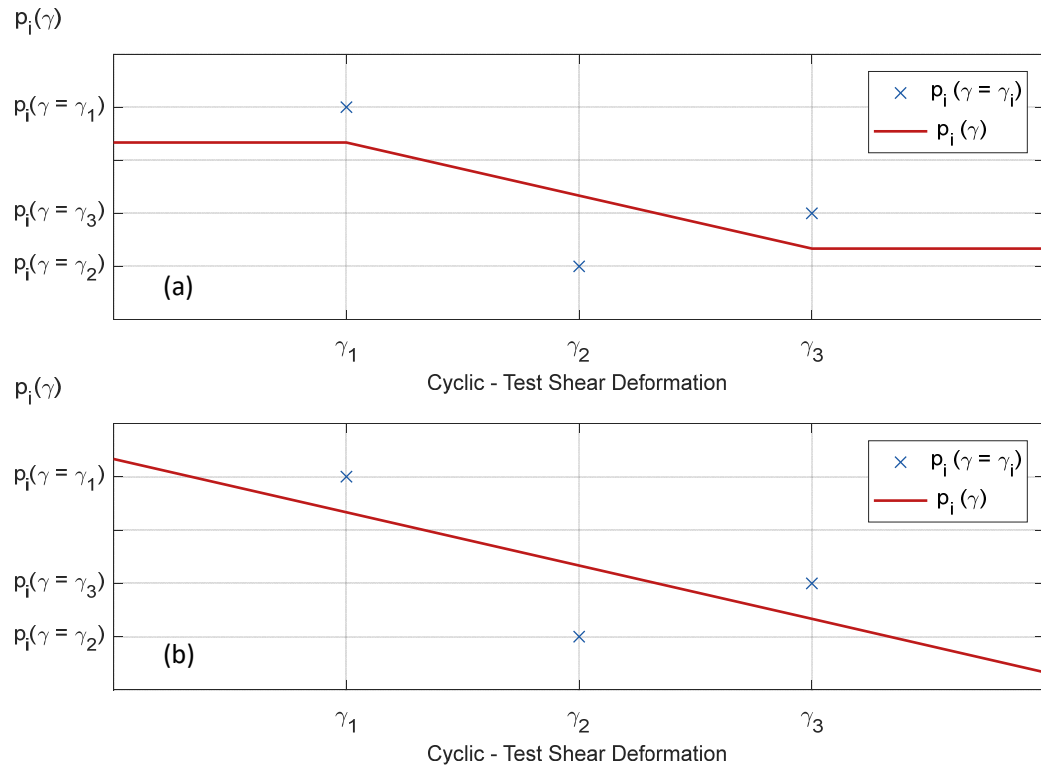


Figure II-12. Displacement-dependent parameter  $p_i$  as a function of the isolator shear strain, when calibrating with earthquake test results: (a) Functional Form 1, FF1; and (b) Functional Form 2, FF2.

The following paragraphs describe the main characteristics and features of the earthquake simulation tests used to calibrate the simplified-model.

### II.6.1 Earthquake simulation test calibration - Case 1

The *Building Nonstructural Components and Systems (BNCS)* (Chen et al. 2013) project considered the construction and earthquake simulation testing of a one to one scale specimen of a five-story reinforced concrete building, equipped with several nonstructural

components. The project considered tests on a fixed-base configuration and on an isolated-base configuration that took place between April 2012 and May 2012 at the George E. Brown, Jr., Network for Earthquake Engineering Simulation (NEES) unidirectional Large High-Performance Outdoor Shake Table at the University of California, San Diego (UCSD). In the base-isolated configuration, the building was subjected to seven ground motions records, representative of the seismicity in California, a central area of Alaska, and a subduction zone in South America. For the simplified-model calibration, a record from the 2007 Mw 8.0 Pisco-Peru earthquake (ICA ground motion record) was selected. In the *BNCS* project, the original ICA ground motion record was scaled by a factor of 1.4; then, the test specimen was subjected to a maximum ground acceleration of 0.50 g, a peak input velocity of 62.59 cm/s, and a peak input displacement of 12.92 centimeters. This ground motion record was the most demanding one used in the isolated-base configuration of the building, so it was selected to test the ability of the simplified model to capture the hardening effect adequately. The building was supported on four high damping rubber isolators (HDRB), whose geometric and material characteristics are listed in Table 4, as Specimen 5.

The force-displacement curve in any of the isolators was required to perform the model calibration. As this information was not directly reported, the induced inertial forces in the building and the resultant shear force demand over the isolation level were estimated by using the accelerometer readings on each floor and their corresponding floor masses lumped at the center of mass of each floor. The isolators' relative displacements were calculated through double integration of the accelerometer readings below and above the isolators.

Figure 13 shows the experimentally measured and the model-predicted force-displacement curves for Specimen 5. The fitted curve in the figure on the left was computed using five

displacement-dependent parameters (all but  $n$ ) while the fitted curve in the figure on the right was computed with all six parameters as constant (i.e., displacement-independent parameters). The model-parameters for both cases are detailed in Table 7. In the case where displacement-dependent parameters were considered, the functional form FF1 was used to relate the parameter with the isolator shear strain. It can be seen that while the fit obtained using five displacement-dependent parameters is better, the one computed with the much simpler displacement-independent (i.e., constant) parameters still provides a very good match of measured hysteretic behavior, being this latter approach good enough for practical engineering applications.

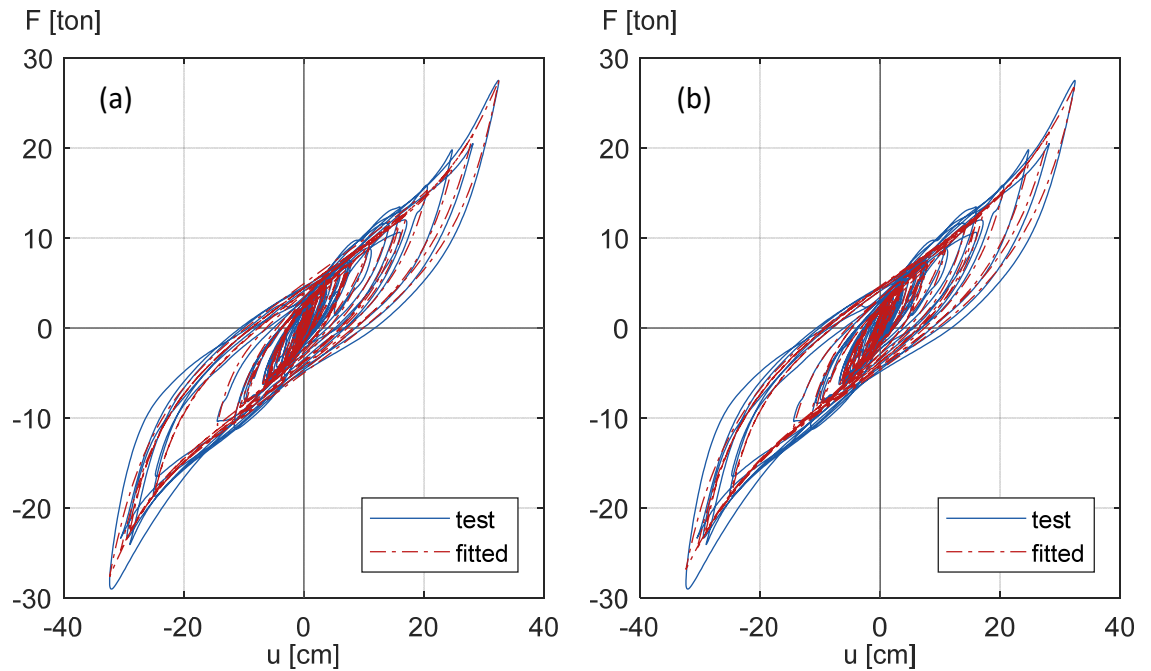


Figure II-13. Force-displacement curves for the experimental test and the model-fitted data under the ICA ground motion record: (a) Five displacement-dependent parameters; and (b) No displacement-dependent parameters, as detailed in Table 7.

Table II-7. Model-calibrated parameters for Specimen 5 under the ICA ground motion record. Displacement-dependent parameters are shown in bold characters.

Case	$\gamma$	$u$ (cm)	$F_y$ (t/cm <sup>2</sup> )	$u_y$ (cm)	$b$	$R$	$u_h$ (cm)	$n$
(a)	0.5	10.2	<b>7.29</b>	<b>2.98</b>	<b>0.20</b>	<b>1.16</b>	<b>23.16</b>	4.65
	1.0	20.4	<b>6.63</b>	<b>2.90</b>	<b>0.18</b>	<b>1.30</b>	<b>20.05</b>	4.65
	1.5	30.6	<b>7.29</b>	<b>3.10</b>	<b>0.20</b>	<b>1.16</b>	<b>21.61</b>	4.65
(b)	any	any	6.83	2.93	0.19	1.24	19.44	3.97

Figure 14 shows the force-history response as a function of time, for the experimental and the model-predicted data, using the model parameters detailed in Table 7.

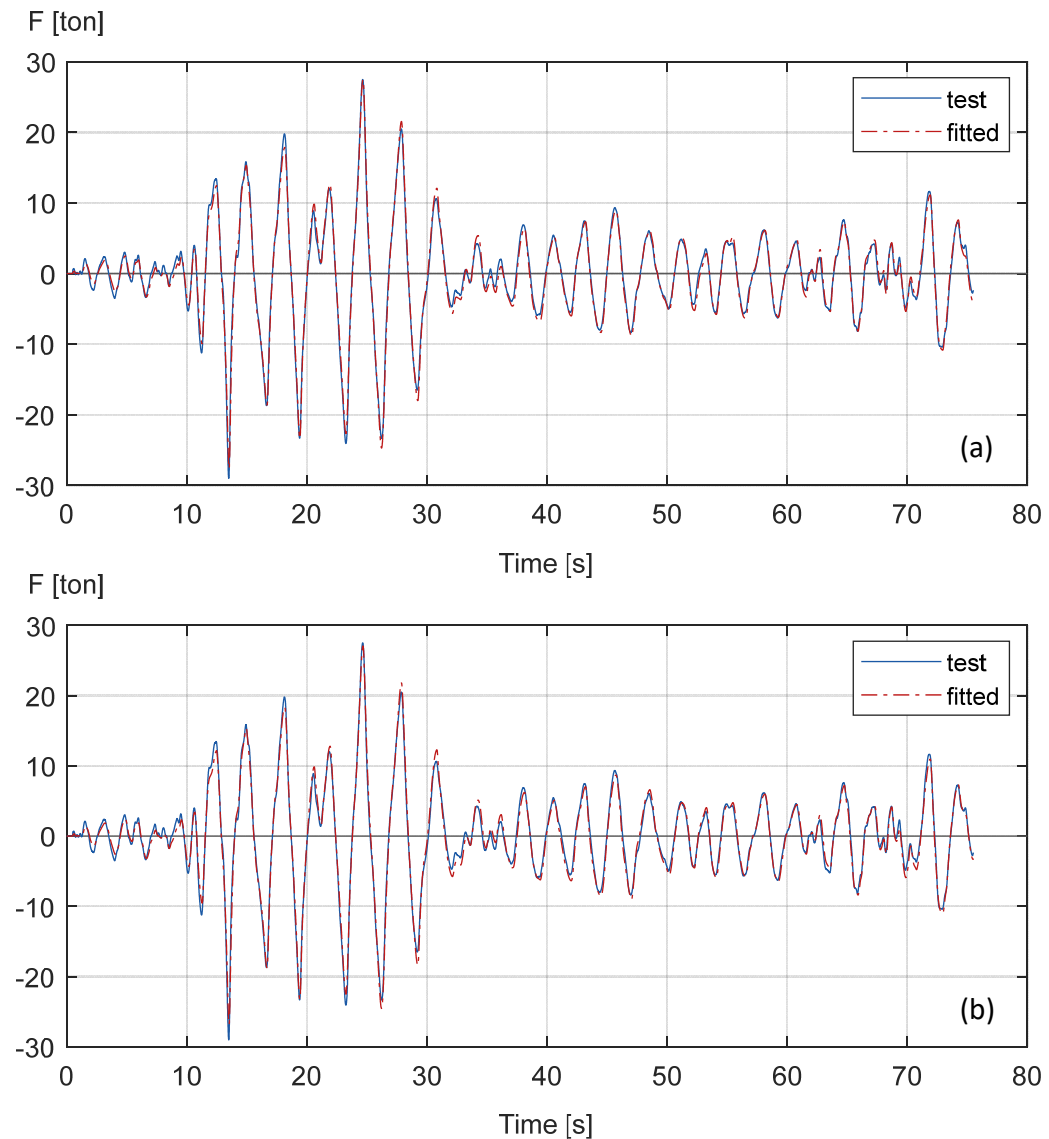


Figure II-14. Force as a function of time for the experimental test and the model-fitted data, under the ICA ground motion record: (a) Five displacement-dependent parameters; and (b) No displacement-dependent parameters, as detailed in Table 7.

## II.6.2 Earthquake simulation test calibration - Case 2

The second earthquake simulation test was taken from the seminal work of Kikuchi and Aiken (1997). The specimen under analysis is a Lead-Rubber Bearing (LRB) described as

Specimen 6 in Table 3. For any further detail on the test features and specifications, the reader is referred to Kikuchi and Aiken (1997), where this specimen is identified as *lead-rubber bearing*. The earthquake simulation test was performed with the well-known NS component of *El Centro* ground motion record from the 1940 Imperial Valley earthquake. Figure 15 shows the experimentally measured and the model-predicted force-displacement curves for Specimen 6. Again the fitted curve in the figure on the left was computed setting five out of the six parameters to be displacement-dependent parameters (all but  $u_h$ ), while the fitted curve in the figure on the right was computed setting all six parameters as constant (i.e., displacement-independent). The model parameters for both cases are detailed in Table 8. In the case where displacement-dependent parameters were considered, the functional form FF1 was used to relate the parameter with the shear strain. Similar to the results shown in Figure 13 and Figure 14, it can be seen that the model-predicted values using constant parameters provide good results that are enough for engineering design practice.

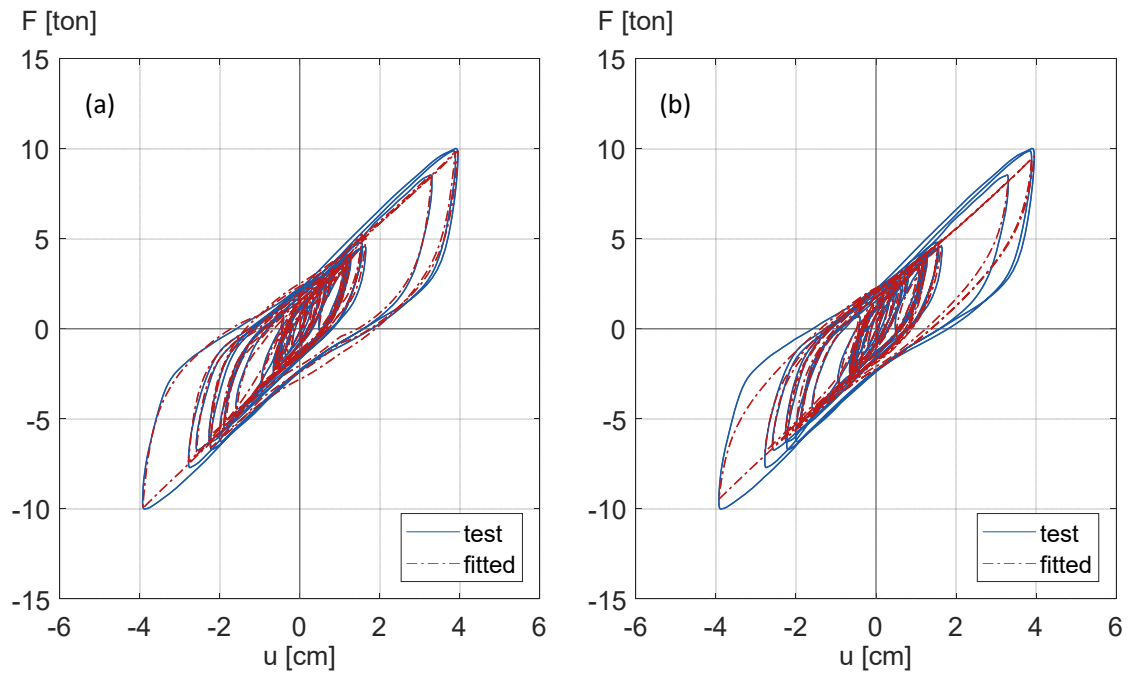


Figure II-15. Force-displacement curves for the experimental test and the model-fitted data, under *El Centro* ground motion record: (a) Five parameters displacement-dependent; and (b) No displacement-dependent parameters, as detailed in Table 8.

Table II-8. Model-calibrated parameters for Specimen 6, under the *El Centro* ground motion record. Displacement-dependent parameters are shown in bold characters.

Case	$\gamma$	$u$ (cm)	$F_y$ (t/cm <sup>2</sup> )	$u_y$ (cm)	$b$	$R$	$u_h$ (cm)	$n$
(a)	0.16	1.5	<b>3.06</b>	<b>0.12</b>	<b>0.04</b>	<b>0.68</b>	1.69	<b>1.42</b>
	0.48	2.5	<b>3.37</b>	<b>0.13</b>	<b>0.03</b>	<b>1.27</b>	1.69	<b>1.52</b>
(b)	any	any	2.69	0.14	0.04	1.00	1.29	1.30

Figure 16 shows the force-history response as a function of time, for the experimental and the model-predicted data, using the model parameters detailed in Table 8.

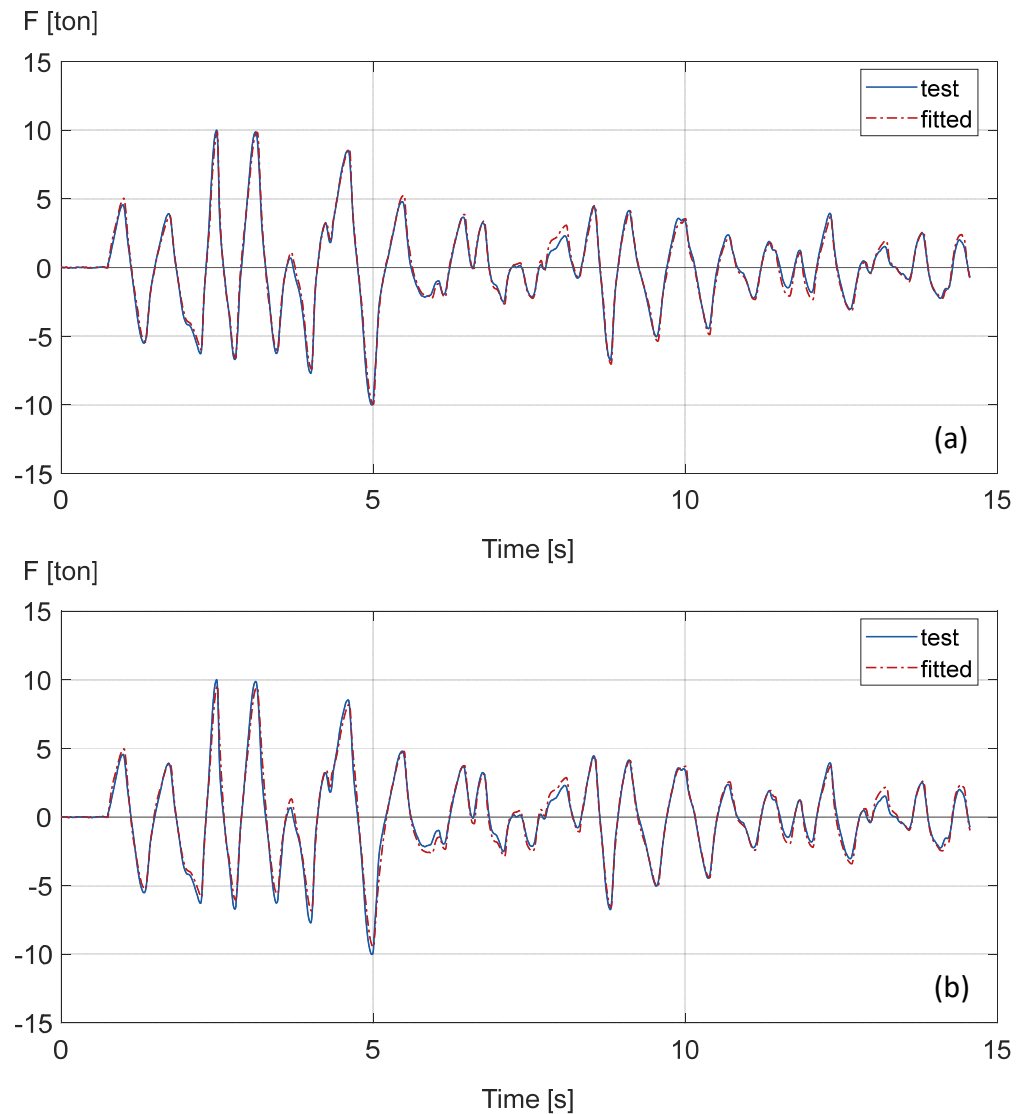


Figure II-16. Force as a function of time for the experimental test and the model-fitted data, under the *El Centro* ground motion record: (a) Five displacement-dependent parameters; and (b) No displacement-dependent parameters, as detailed in Table 8.

In Figure 17, an analysis of the tradeoff between considering an increasing number of displacement-dependent parameters in exchange for minimizing the error is presented. As it should be expected, the error decreases as the number of displacement-dependent parameters increases; however, a distinct difference is observed for Specimen 5 (HDRB) relative to

Specimen 6 (LRB), as the former is less sensitive to the number of displacement-dependent parameters. This condition can be confirmed by comparing the force-displacement curves in Figure 13, that look quite similar despite their difference in the definition of parameters. The total error of the model-fitted force-history increases only 20% when comparing the simplest model with no displacement-dependent parameters, with the most complex model, with five displacement-dependent parameters.

On the other hand, Specimen 6 is more sensitive to the model parameter definition, with a fitting error that is 75% higher in the simplest case (no displacement-dependent parameters) relative to the most complex case (five displacement-dependent parameters). However, a noticeable improvement in the fitting quality occurs by considering only one parameter as displacement-dependent ( $R$  in this case). In this new scenario, the relative error reduces from 75% to being only 15% higher than the best fit case. As can be seen in Figure 17, as more parameters become displacement-dependent, the additional fitting improvement is rather small. As previously stated in this article, the choice of the functional form used to evaluate the displacement-dependent parameters does not have a significant influence on the quality of the fit for both cases under study.

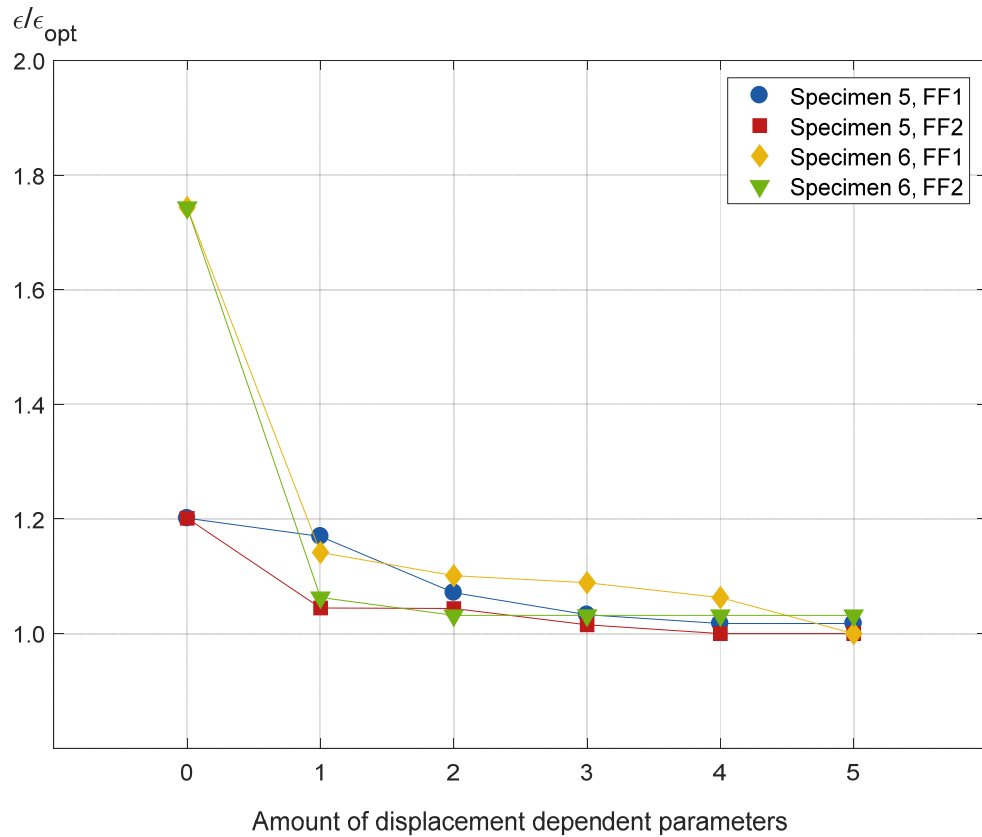


Figure II-17. Relative error as a function of the number of displacement-dependent parameters for both specimens being calibrated with earthquake simulator tests.

## II.7 Summary And Conclusions

A new simplified and versatile design-oriented model for seismic isolation bearings has been presented. Its ability to accurately represent the behavior of different types of seismic isolators was demonstrated through the calibration of six different specimens, four with cyclic test results, and two with earthquake simulation test results. The agreement between the experimental test data and the model-predicted values is entirely satisfactory for practical design purposes, even if most of the model parameters are displacement-independent, i.e., parameters that are not defined as a function of the isolator shear strain.

The calibration with cyclic tests was performed through the minimization of different measures of error between test-measured and model-predicted values. The difference between dissipated energy, force history, and stiffness history for a deformation cycle were considered. Results showed that for isolators that exhibit significant hardening, the minimization of the force deviation delivers more robust optimal parameters than the minimization of the error in the lateral stiffness. This is the case because in minimizing the difference in lateral stiffness, the optimization procedure has a bias to the hardening region, allowing larger errors in the region of smaller stiffnesses which are actually more likely to produce larger displacement increments.

For the earthquake simulation test calibration, two different functional forms were analyzed to constrain the variation of some of the parameters with the level of shear strain imposed in the isolator. Results showed that for the specimens that were considered, both functional forms led to similar error levels. Consequently, the use of a simple linear functional form (FF2) is recommended.

Because seismic design codes require cyclic testing of isolator prototypes for each project, the calibration of the model can always be done using real data, enabling specific parameter calibrations and the need for presenting completely general values for those six parameters. However, Tables 5, 6, 7, and 8 can serve as useful references for choosing optimal parameter values in an initial phase of seismic isolation design.

The proposed model can capture the hardening effect on elastomeric isolators accurately. Also, the type of isolator being modeled can be easily changed by just modifying the six parameters of the model. Then, this novel model presents a highly desirable balance between

accuracy and simplicity on its implementation, making it particularly amenable for implementation in general-purpose seismic analysis software packages.

### **Acknowledgments**

This research was funded by CONICYT Doctorado Nacional 21161027, the National Research Center for Integrated Natural Disaster Management CONICYT /FONDAP/15110017, and FONDECYT grant 1170836 (SIBER-RISK). The authors also would like to thank the John A. Blume Earthquake Engineering Center at Stanford University for hosting the first author during his one-year stay at Stanford as visiting student researcher and to Professor Masaru Kikuchi and Dr. Ian Aiken, who generously provided results of cyclic and earthquake simulation tests, used to calibrate the model presented in this article.

### **References**

- Abe, M., Yoshida, J., and Fujino, Y., 2004. Multiaxial behaviors of laminated rubber bearings and their modeling. II: Modeling. *Journal of Structural Engineering*, **130(8)**, 1133-1144.
- Bauschinger, J., 1881. Ueber die Veränderung der Elasticitätsgrenze und des Elasticitätsmoduls verschiedener Metalle. *Civiling NF*, **27 (19)**, pp. 289-348.
- Bosco, M., Ferrara, E., Ghersi, A., Marino, E. M., and Rossi, P. P., 2016. Improvement of the model proposed by Menegotto and Pinto for steel. *Engineering Structures*, **124**, 442-456.
- Bouc, R., 1971. A mathematical model for hysteresis. *Acta Acustica united with Acustica*, **24(1)**, 16-25.

Box, G. E., Luceño, A., and Del Carmen Paniagua-Quinones, M. (2011). *Statistical control by monitoring and adjustment*, Second edition, John Wiley & Sons.

Ciampi, V., Eligehausen, R., Bertero, V. V., and Popov, E. P., 1982. Analytical model for concrete anchorages of reinforcing bars under generalized excitations. Berkeley, CA, USA: College of Engineering, University of California.

Chen, M. C., Pantoli, E., Wang, X., Astroza, R., Ebrahimian, H., Mintz, S., Hutchinson, T., Conte, J., Restrepo, J., Meacham, B., Kim, J., and Park, H., 2013a. BNCS Report #1: Full-Scale Structural and Nonstructural Building System Performance during Earthquakes and PostEarthquake Fire - Specimen Design, Construction and Test Protocol, Structural Systems Research Project Report Series, SSRP 13/9, University of California San Diego, La Jolla, CA.

Chen, M. C., Pantoli, E., Wang, X., Mintz, S., Hutchinson, T., and Restrepo, J., 2013b. BNCS Report #4: Full-Scale Structural and Nonstructural Building System Performance during Earthquakes and Post-Earthquake Fire – Construction Details and Technical Specifications of Specific Subsystems, Structural Systems Research Project Report Series, SSRP 13/12, University of California San Diego, La Jolla, CA.

Dall'Asta, A., and Ragni, L., 2006. Experimental tests and analytical model of high damping rubber dissipating devices. *Engineering Structures*, **28(13)**, 1874-1884.

De la Llera, J.C., Luders, C., Leigh, P. and Sady, H. Analysis, testing, and implementation of seismic isolation of buildings in Chile. *Earthquake Engineering and Structural Dynamics*, **33(5)**, 543–574.

Hwang, J. S., Wu, J. D., Pan, T. C., and Yang, G., 2002. A mathematical hysteretic model for elastomeric isolation bearings. *Earthquake Engineering & Structural Dynamics*, **31(4)**, 771-789.

Ibarra, L. F., Medina, R. A., and Krawinkler, H., 2005. Hysteretic models that incorporate strength and stiffness deterioration. *Earthquake engineering & structural dynamics*, **34(12)**, 1489-1511.

- Lion, A., 1997. On the large displacement behaviour of reinforced rubber at different temperatures. *Journal of the Mechanics and Physics of Solids*, **45(11-12)**, 1805-1834
- Kikuchi, M., and Aiken, I. D., 1997. An analytical hysteresis model for elastomeric seismic isolation bearings. *Earthquake engineering & structural dynamics*, **26(2)**, 215-231.
- Menegotto M, and Pinto PE., 1973. Method of analysis for cyclically loaded reinforced concrete plane frames including changes in geometry and non-elastic behaviour of elements under combined normal force and bending. IABSE symposium of resistance and ultimate deformability of structures acted on by well-defined repeated loads, vol. 13. Lisbon, Portugal: International Association of Bridge and Structural Engineering; 1973. p. 15–22.
- Mullins, L., 1969. Softening of rubber by displacement. *Rubber chemistry and technology*, **42(1)**, 339-362.
- Ramberg W, and Osgood WR., 1943 Description of stress-strain curves by three parameters Technical note No. 902. Washington DC: National Advisory Committee for Aeronautics; 1943.
- Ozdemir, Non-linear transient dynamic analysis of yielding structures, Ph.D. Dissertation, Division of Structural Engineering and Structural Mechanics, Department of Civil Engineering, University of California, Berkeley, 1976.
- Pan, T. C., and Yang, G. (1996, June). Non-linear analysis of base-isolated MDOF structures. *In Proceedings of the 11th World Conference on Earthquake Engineering, Mexico*.
- Tsai, C. S., Chiang, T. C., Chen, B. J., and Lin, S. B., 2003. An advanced analytical model for high damping rubber bearings. *Earthquake engineering & structural dynamics*, **32(9)**, 1373-1387
- Tsopelas, P., Constantinou, M. C., and Reinhorn, A. M. (1994). 3D-BASIS-ME: Computer program for non-linear dynamic analysis of seismically isolated single and multiple structures and liquid storage tanks.

Tubaldi, E., Ragni, L., Dall'Asta, A., Ahmadi, H., and Muhr, A. (2017). Stress softening behaviour of HDNR bearings: modelling and influence on the seismic response of isolated structures. *Earthquake Engineering & Structural Dynamics*, **46(12)**, 2033-2054.

Wen, Y. X., 1976. Method for random vibration of hysteretic systems. *Journal of the engineering mechanics division*, **102(2)**, 249-263.

### III. UNCERTAINTY ON MEASUREMENT OF ELASTOMERIC ISOLATORS EFFECTIVE PROPERTIES

Sebastián Miranda<sup>1</sup>, Juan Carlos de la Llera<sup>1</sup>, and Eduardo Miranda<sup>2</sup>

<sup>1</sup>Department of Structural and Geotechnical Engineering, Pontificia Universidad Católica de Chile, and National Research Center for Integrated Natural Disaster Management, CONICYT/FONDAP/15110017, Santiago 7820436, Chile

<sup>2</sup> John A. Blume Earthquake Engineering Center, Department of Civil and Environmental Engineering, Stanford University, Stanford, CA 94305-4020, U.S.A.

#### III.1 Abstract

Elastomeric seismic isolators are subjected to a series of non-destructive tests with several repeated deformation cycles before they are implemented in a structure. For each deformation cycle, effective properties are determined in each direction and then averaged. Despite their inherent uncertainty, these properties are treated as deterministic values by seismic design procedures. Consequently, a methodology based on the *Guide to the expression of Uncertainty in Measurement GUM* and Monte-Carlo simulation is implemented to assess the uncertainty in these properties, considering variability between repetitions and instrumentation errors. The peak relative expanded uncertainty in all considered effective properties reaches a maximum of 12%, and the *GUM* method and Monte-Carlo simulation method lead to similar results. A higher-order polynomial approximation for the *GUM* uncertainty assessment was implemented; however, results including higher-order terms do not deliver significant differences to the traditional first-order approach.

### III.2 Introduction

Inherent uncertainty in measurements is a relevant topic since the measurand value by itself does not constitute a complete test result. It should be mandatory to specify the quality of the result with a parameter that reflects its reliability; however, this information is frequently skipped in reporting test results. Several uncertainty calculation procedures have been proposed and used historically [1]; however, since the release of the *Guide to the expression of Uncertainty in Measurement (GUM)* [2], the testing industry has embraced this methodology as a standard. The publication of this *Guide* constitutes a landmark in the measurement field, as it presented, probably for the first time, a comprehensive and standardized approach for uncertainty evaluation, irrespective of the type of measurement and the required level of accuracy [3]. The *Guide* uses a first-order Taylor expansion for estimating the variance of an arbitrary output quantity  $y$ , i.e., the test measurand, as a function of the variances of  $n$  input quantities  $x_i$ , which are directly measured or estimated during the test. The measurand  $y$  and the input quantities  $x_i$  need to be related through a model  $y = f(x_1, x_2, \dots, x_n)$ . The *Guide* uses both, frequentist and Bayesian statistical methods, to assign a standard uncertainty value for each of the input quantities  $x_i$  and then propagate them into the measurand  $y$ . Also, the *Guide* includes supplements for Monte-Carlo implementation [4], a glossary of metrology related concepts, the International vocabulary of Metrology *VIM* [5], and other related documents.

Da Silva and Ten Caten [6] presented a comprehensive literature review comprising 114 journal articles published in four journals between 2004 and 2010 in which the main topic was measurement uncertainty. The authors classified the articles based on different criteria,

one of them being the method used for uncertainty quantification. By far, the most commonly used technique was the *GUM* method, followed by Monte-Carlo simulation and Fuzzy variables procedures [7,8]. This research focuses on the evaluation of uncertainty in the effective properties of seismic isolators using the *GUM* methodology and Monte-Carlo simulation.

Many research articles in vastly different fields assessing uncertainty using the *GUM* procedure are available in the literature. For instance, Shahanaghi and Nakhjiri [9] quantified uncertainty in the calibration of a platinum resistance thermometer using the *GUM* methodology and Monte-Carlo simulation, and results showed a difference between the symmetric uncertainty interval obtained with *GUM* and a skewed uncertainty interval given by Monte-Carlo simulation. Both approaches were also implemented in the work of Theodorou et al. [10] in the estimation of the uncertainty in the direct estimation of cadmium in water by graphite furnace atomic absorption spectrometry. Results in this case showed a mild overestimation of the uncertainty when the *GUM* method is implemented. Chen and Chen [11] assessed the uncertainty on a perspiration measurement system composed of several sensors. The authors considered several uncertainty sources as airflow rate, air density, and humidity. They carried out a comparison between *GUM* and Monte-Carlo methods obtaining no significant differences in the uncertainty values. Junga et al. [12] quantified measurement uncertainties required to determine the thermal-balance in small-scale boilers, also implementing both methodologies. The authors concluded that Monte-Carlo methods are faster, simpler, and easier to implement in spreadsheets of commercial computation tools, delivering results showing excellent accuracy relative to the ones from the *GUM* method. In the recent work of Moona et al. [13], the dot pitch of a display monitor

shadow mask was measured by interferometry. Again, they assessed the uncertainty of the expected dot pitch value by the GUM and MonteCarlo methods, obtaining similar values for both approaches.

Some relevant articles in civil and mechanical engineering applications include the work of Link et al. [14] and Bringmann and Knapp [15] that used Monte-Carlo simulation to assess the uncertainty on the parameters characterizing piezoelectric accelerometers, and the measurements performed during a machine tool calibration, respectively. Furthermore, the work of Leyi et al. [16] analyzed uncertainty sources for the Brinell hardness measurements. Additionally, they used finite elements and Monte-Carlo simulations to acquire theoretical measurement uncertainties. Mahmoud and Hegazy [17] implemented the *GUM* and Monte-Carlo methods to assess the uncertainty in Brinell and Vickers hardness measurements. As stated in different investigations, their results showed no significant differences between the *GUM* expanded uncertainty and the Monte-Carlo estimation. Also, they found that the correlations between input quantities play an essential role in the estimated uncertainties. The work of Guimaraes et al. [18] presented examples of uncertainty assessment in Brinell hardness measurement and a torque measurement.

Kuhinek et al. [19] studied uniaxial compressive tests to determine the strength and deformability of rock samples. They performed a *GUM* uncertainty assessment, considering transducers and other instrumentation as sources of uncertainty. Results showed a relative standard uncertainty lower than 1% for strength and elasticity modulus and ranging from 2.6% to 12% for the Poisson coefficient. Godina and Acko [20] analyzed the calibration of a gauge block comparing the interferometric and mechanical methods for calibration. They concluded that mechanical calibration delivers credible expected values but more uncertain

than the ones estimated with interferometric calibration. Additionally, Salah et al. [21] presented an uncertainty analysis of stress and elongation measurement on metal tensile tests by implementing the *GUM* method, Monte-Carlo simulation, and Markov Chain Monte-Carlo simulation. Kapper et al. [22] studied plastic anisotropy ratio for sheet-metals. The most relevant uncertainty sources were repeatability and reproducibility, being the latter more significant than the former. As defined in the *GUM* [2], repeatability considers independent test results obtained from identical specimens with the same method, laboratory, equipment, and operator, while reproducibility considers the same testing method done on identical specimens but performed with different operators, equipment, and laboratories.

Based on the inherent uncertainty of rubber mechanical properties and uncertainties arising in the fabrication process, as isolators are frequently custom designed and manufactured, seismic codes (e.g., ASCE/SEI 7-16 [23], NCh2745 [24]) establish rigorous testing programs for prototype and regular isolators. Results from these tests show that elastomeric isolators present a strongly nonlinear force-displacement relationship, including axial load dependency, strain hardening, strain-rate effects, and load-path effects. Moreover, the widely studied Mullins effect [25], which corresponds to a degradation of the isolator maximum load and stiffness after each load cycle (a phenomenon also known as *scragging*), is also observed. To account for these relevant isolator features, tests consider several displacement sequences at a given shear strain. For each sequence, several full-reversed displacement cycles are performed; a typical shear force-lateral displacement curve for an elastomeric isolator is shown in Figure 1 for four different shear deformations  $\gamma =$

0.25,0.50,1.0 and 1.5. Full cycles are presented in Figure 1(a), and a close-up of the maximum forces is shown in Figure 1(b).

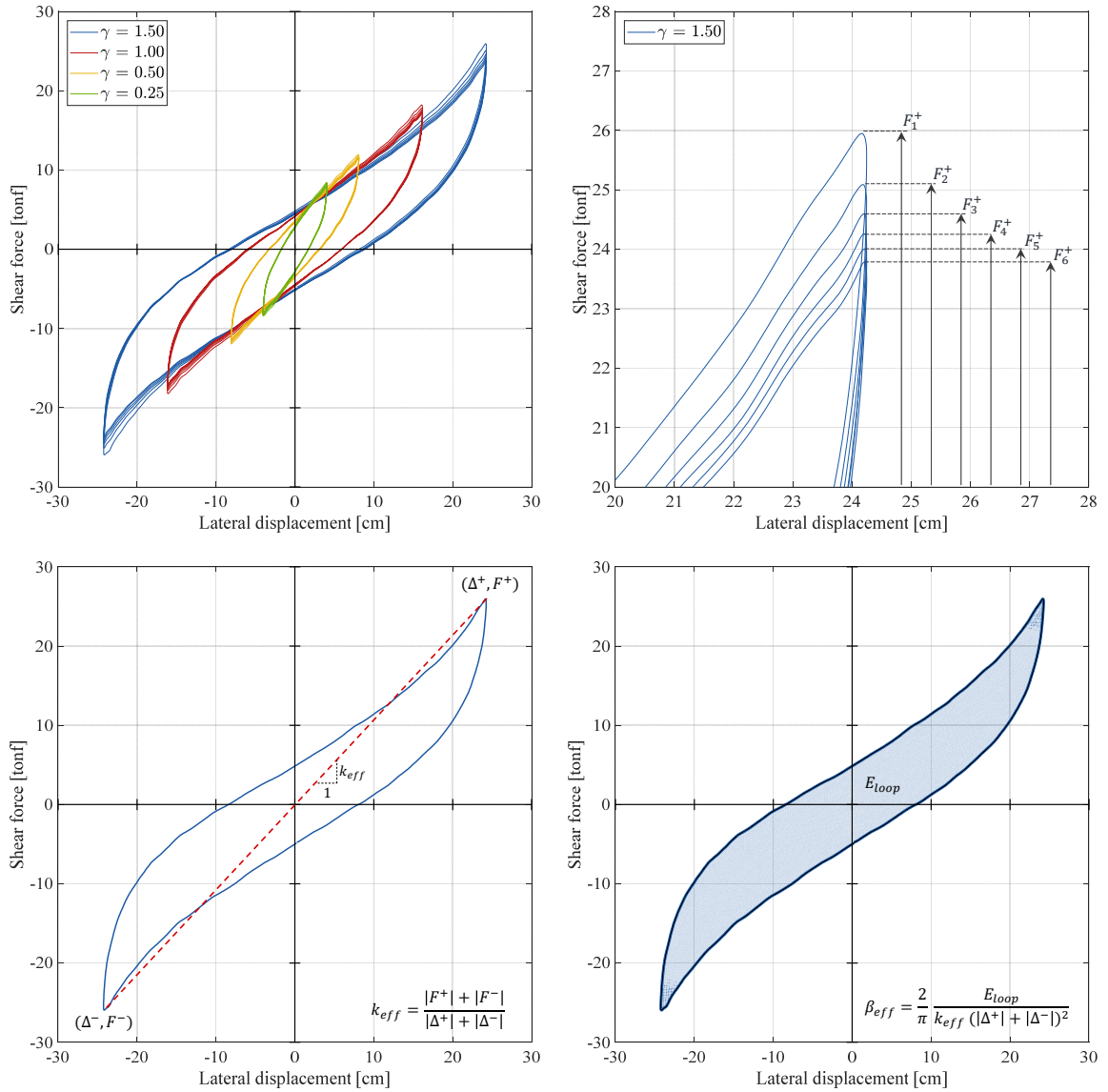


Figure III-1. (a) Shear force – lateral displacement curve for an annular elastomeric isolator with an external diameter  $D_{ext} = 70\text{ cm}$ , internal diameter  $D_{int} = 10\text{ cm}$ , and total rubber height  $H_r = 16.2\text{ cm}$ , considering four displacement sequences with  $\gamma = 0.25, 0.50, 1.00,$  and  $1.50$  and six repetition cycles for each sequence; (b) Different maximum force values used for uncertainty

calculation; (c) Equivalent stiffness  $k_{eff}$  as defined in ASCE-7 and NCh2745; and (d) Energy dissipated in one displacement cycle,  $E_{loop}$ , as required for equivalent damping  $\beta_{eff}$  calculation.

In spite of the complexity of the behavior of elastomeric isolators, most structures are designed using an approximate methodology based on two effective isolator properties derived from measured by test shear force - lateral displacement curves; which are: (1) the lateral effective stiffness  $k_{eff}$ , calculated as the force-displacement curve slope to a given objective displacement, (Figure 1(c)); and (2) the effective damping ratio  $\beta_{eff}$ , based on the energy dissipated ( $E_{loop}$ ) during a full cycle of reversible load over the displacement amplitude  $|\Delta^+| + |\Delta^-|$  [23], as it is schematically shown in Figure 2(d) and presented elsewhere [26]. Effective stiffness  $k_{eff}$  and effective damping  $\beta_{eff}$  are calculated for each displacement cycle and their values averaged, discarding the first cycle to use the *scragged* properties of the isolator. The acceptance or rejection of a specific isolator unit is based on its average properties, thus neglecting the uncertainty of this value.

The main objectives of this research are: (1) to implement an uncertainty quantification procedure for the measured-by-test effective properties of elastomeric isolators, according to the *GUM* methodology; (2) to evaluate effective properties uncertainty considering only Type A (repeatability) uncertainty sources; (3) to evaluate effective properties uncertainty considering combined Type A and Type B uncertainty sources; and (4) to validate the results from *GUM* methodology by Monte-Carlo simulation.

### III.3 Uncertainty Evaluation Procedures

#### III.3.1 Elastomeric Isolators Test-Results Dataset

This research project is developed in conjunction with the "Laboratory for dynamic testing and vibration control" at Pontificia Universidad Catolica de Chile. This testing facility has performed more than 6,000 tests of elastomeric seismic isolators during the last twenty years. For further details on the experimental test setup, the reader should refer to De la Llera et al. [27]. As required by the seismic isolation Chilean Code NCh2745 [24], two types of experimental tests are performed: (i) prototype tests, applied over a representative sample of the isolators of the project to validate the isolation system design properties considering several combinations of dead loads, live loads, wind loads and earthquake loads; and (ii) quality-control tests (production tests in ASCE/SEI 7-16 [23] terminology) in which all the seismic isolators of the project are subjected to consecutive sequences of lateral deformation, typically at values of shear strain  $\gamma = 0.25$ ,  $\gamma = 0.50$ ,  $\gamma = 1.00$ , and a final design value  $\gamma = \gamma_D$ , as defined by the structural engineer, that usually ranges between  $\gamma = 1.20$  and  $\gamma = 1.50$  for the Chilean design experience. All these shear strains are imposed under the expected axial load, i.e., the average axial load for all isolators of the same type under the dead (D), and live (L), load combination  $D + 0.50 L$ .

The dataset considered the results of more than 2,400 quality-control tests of elastomeric seismic isolators from 40 projects constructed between 2007 and 2014 in Chile and Peru. These projects include hospitals, buildings, bridges, and industrial facilities. All specimens were manufactured by the same company, using two different compounds vulcanized from natural rubber; namely, Compound 1, for low stiffness isolators, and Compound 2, for

medium stiffness isolators. All specimens have annular geometry with external diameters ( $D_{ext}$ ) ranging from 50 cm to 115 cm, internal diameters ( $D_{int}$ ) from 10 cm to 15 cm, 0.3 cm thick steel shims ( $t_s$ ), and 2 cm thick end steel plates ( $e_s$ ) at the top and bottom. Isolator total rubber heights range from 12.6 cm to 25.9 cm, using rubber layers with thicknesses ( $t_r$ ) from 0.6 cm to 0.8 cm. The expected axial loads over the isolators range from 3760 kN to 10380 kN, and from 1960 kN to 9200 kN, implying vertical stresses ranging from 0.21 kN/cm<sup>2</sup> to 2.02 kN/cm<sup>2</sup>, and from 0.55 kN/cm<sup>2</sup> to 1.68 kN/cm<sup>2</sup> for compounds 1 and 2, respectively. Table 1 classifies the specimens based on their manufacturing compound and external diameter. Figure 2 shows the geometric parameters of an isolator unit.

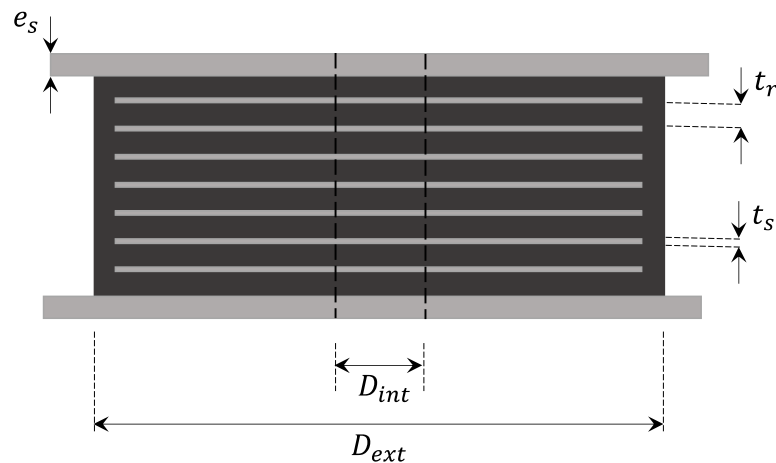


Figure III-2. Seismic isolator geometric parameters.

Table III-1. Number of isolators and main geometric features

Isolator External Diameter (cm)	Number of Specimens	
	Compound 1	Compound 2
50	0	13
60	148	13
65	56	130
70	38	539
75	409	219
80	62	197
85	33	76
90	227	175
100	91	27
115	45	0
<b>Total</b>	<b>1109</b>	<b>1389</b>

### III.3.2 Summary of the GUM Uncertainty Quantification Methodology

The *GUM* methodology for measurement uncertainty assessment has become the standard in the last decades, mainly because of its simplicity and ability to combine different uncertainty sources. Uncertainties assessed from several measurements under *repeatability conditions*, and uncertainties evaluated from non-statistically assessed data, are defined as Type A and Type B uncertainty sources, respectively. Type B uncertainty sources are related to code tolerances, experience values, instrument resolution, variability in operators, among others.

Given some functional relationship between an arbitrary number of assumed uncorrelated input quantities  $x_i$ , which are in most cases directly measured, and an output quantity  $y = f(x_1, x_2, \dots, x_n)$ , the combined uncertainty on the output quantity  $u_c(y)$  is estimated by propagating the uncertainties in the input quantities  $u(x_i)$  through the expression:

$$u_c^2(y) = \sum_{i=1}^N \left( \frac{\partial f}{\partial x_i} \right)^2 u^2(x_i) \quad (1)$$

an equation that is based on a first-order Taylor expansion of the variance of the measurand  $y$ . As stated in the Guide [2], the combined uncertainty  $u_c^2(y)$  is an estimator of the variance and characterizes the dispersion of the values that could be reasonably be attributed to the measurand  $Y$ . It should be noted, that Equation (1) applies when all the input quantities  $x_i$  are mutually uncorrelated. The partial derivatives are typically named sensitivity coefficients

$$c_i = \partial f / \partial x_i = \partial y / \partial x_i \quad (2)$$

Equation (1) can be conveniently rewritten in matrix format as

$$u_c^2(y) = \mathbf{g}^T \mathbf{u}^2(\mathbf{x}_i) \mathbf{g} \quad (3)$$

where

$$\mathbf{g} = \left[ \frac{\partial y}{\partial x_1} \quad \frac{\partial y}{\partial x_2} \quad \dots \quad \frac{\partial y}{\partial x_n} \right]^T = \nabla y \quad (4)$$

is a gradient vector containing the sensitivity coefficients of the measurand  $y = f(x_1, x_2, \dots, x_n)$  with respect to all the input variables  $x_i$  and

$$\mathbf{u}^2(\mathbf{x}_i) = \begin{bmatrix} u^2(x_1) & 0 & \dots & 0 \\ 0 & u^2(x_2) & \dots & 0 \\ \vdots & \vdots & \ddots & \vdots \\ 0 & 0 & \dots & u^2(x_n) \end{bmatrix} \quad (5)$$

is a diagonal matrix where  $u^2(x_i)$  is the squared standard uncertainty for each input quantity  $x_i$ .

The counterpart of Equation (1) for the case with correlated input quantities, a frequent condition in measuring input quantities using the same or similar instruments, is given by Equation (6)

$$u_c^2(y) = \sum_{i=1}^N \left( \frac{\partial f}{\partial x_i} \right)^2 u^2(x_i) + 2 \sum_{i=1}^{N-1} \sum_{j=i+1}^N \left( \frac{\partial f}{\partial x_i} \right) \left( \frac{\partial f}{\partial x_j} \right) u(x_i, x_j) \quad (6)$$

where  $x_i$  and  $x_j$  are the estimates of  $X_i$  and  $X_j$  and  $u(x_i, x_j) = u(x_j, x_i)$  is the estimated covariance associated with  $x_i$  and  $x_j$ . The degree of linear correlation between  $x_i$  and  $x_j$  is characterized by the estimated correlation coefficient, shown in Equation (7)

$$r(x_i, x_j) = \frac{u(x_i, x_j)}{u(x_i) u(x_j)} \quad (7)$$

where  $r(x_i, x_j) = r(x_j, x_i)$ , and  $-1 \leq r(x_i, x_j) \leq +1$ . Rewriting Equation (6) as a function of the correlation and sensitivity coefficients gives:

$$u_c^2(y) = \sum_{i=1}^N c_i^2 u^2(x_i) + 2 \sum_{i=1}^{N-1} \sum_{j=i+1}^N c_i c_j u(x_i) u(x_j) r(x_i, x_j) \quad (8)$$

equation that can be expressed in compact matrix format as

$$u_c^2(y) = \mathbf{g}^T \mathbf{cov}(x_i) \mathbf{g} \quad (9)$$

where the covariance matrix  $\mathbf{cov}(x_i)$  is defined as:

$$\mathbf{cov}(x_i) = \begin{bmatrix} u^2(x_1) & r(x_1, x_2) u(x_1) u(x_2) & \dots & r(x_1, x_n) u(x_1) u(x_n) \\ r(x_2, x_1) u(x_2) u(x_1) & u^2(x_2) & \dots & r(x_2, x_n) u(x_2) u(x_n) \\ \vdots & \vdots & \ddots & \vdots \\ r(x_n, x_1) u(x_n) u(x_1) & r(x_n, x_2) u(x_n) u(x_2) & \dots & u^2(x_n) \end{bmatrix} \quad (10)$$

The described approach delivers reasonable uncertainty estimations under the assumption that the relationship between the input quantities  $x_i$  and the measurand  $y$  is not highly nonlinear when evaluated in the expected values of the input quantities  $x_i$ . One novelty of this study is to include a second-order term in the Taylor expansion of the measurand variance  $u_c(y)$ , an approach previously developed by authors as Lira [28] and Mekid and Vaja [29]. However, they considered the particular case of a single input quantity. The

expression in matrix form for uncertainty estimation, considering a second-order Taylor polynomial approximation for  $u_c(y)$ , is given in Equation (11).

$$u_c^2(y) = \mathbf{g}^T \mathbf{cov}(\mathbf{x}_i) \mathbf{g} + \frac{1}{4} (\mathbf{g}')^T \mathbf{krt}(\mathbf{x}_i) \mathbf{g}' + \mathbf{g}^T \mathbf{skw}(\mathbf{x}_i) \mathbf{g}' - \frac{1}{4} (\mathbf{g}')^T \mathbf{var}^2(\mathbf{x}_i) \mathbf{g}' \quad (11)$$

where

$$\mathbf{krt}(\mathbf{x}_i) = \mathbf{E} \begin{bmatrix} (x_1 - \bar{x}_1)^4 & (x_1 - \bar{x}_1)^2(x_2 - \bar{x}_2)^2 & \dots & (x_1 - \bar{x}_1)^2(x_n - \bar{x}_n)^2 \\ (x_2 - \bar{x}_2)^2(x_1 - \bar{x}_1)^2 & (x_2 - \bar{x}_2)^4 & \dots & (x_2 - \bar{x}_2)^2(x_n - \bar{x}_n)^2 \\ \vdots & \vdots & \ddots & \vdots \\ (x_n - \bar{x}_n)^2(x_1 - \bar{x}_1)^2 & (x_n - \bar{x}_n)^2(x_2 - \bar{x}_2)^2 & \dots & (x_n - \bar{x}_n)^4 \end{bmatrix} \quad (12)$$

$$\mathbf{skw}(\mathbf{x}_i) = \mathbf{E} \begin{bmatrix} (x_1 - \bar{x}_1)^3 & (x_1 - \bar{x}_1)(x_2 - \bar{x}_2)^2 & \dots & (x_1 - \bar{x}_1)(x_n - \bar{x}_n)^2 \\ (x_2 - \bar{x}_2)(x_1 - \bar{x}_1)^2 & (x_2 - \bar{x}_2)^3 & \dots & (x_2 - \bar{x}_2)(x_n - \bar{x}_n)^2 \\ \vdots & \vdots & \ddots & \vdots \\ (x_n - \bar{x}_n)(x_1 - \bar{x}_1)^2 & (x_n - \bar{x}_n)(x_2 - \bar{x}_2)^2 & \dots & (x_n - \bar{x}_n)^3 \end{bmatrix} \quad (13)$$

and

$$\mathbf{var}^2(\mathbf{x}_i) = \begin{bmatrix} u^4(x_1) & u^2(x_1)u^2(x_2) & \dots & u^2(x_1)u^2(x_n) \\ u^2(x_2)u^2(x_1) & u^4(x_2) & \dots & u^2(x_2)u^2(x_n) \\ \vdots & \vdots & \ddots & \vdots \\ u^2(x_n)u^2(x_1) & u^2(x_n)u^2(x_2) & \dots & u^4(x_n) \end{bmatrix} \quad (14)$$

Equation (11) introduces the vector  $\mathbf{g}'$  defined by Equation (15)

$$\mathbf{g}' = \left[ \frac{\partial^2 y}{\partial x_1^2} \quad \frac{\partial^2 y}{\partial x_2^2} \quad \dots \quad \frac{\partial^2 y}{\partial x_n^2} \right]^T \quad (15)$$

Equation (11) propagates not only the standard uncertainty  $u(x_i)$  of the input quantities  $x_i$ , but also their skewness and kurtosis, the third and fourth-order moments of their probability density functions, respectively. For the sake of brevity in this presentation, the demonstration of Equation (11) is left for Appendix A.

In this work, *GUM* [2] methodology is applied to quantify the uncertainty in elastomeric isolators effective properties  $k_{eff}$  and  $\beta_{eff}$ . To evaluate uncertainty of these properties,

models relating the measurands  $k_{eff}$  and  $\beta_{eff}$  and their input variables are shown in Equations (16) and (17),

$$k_{eff} = \frac{|F^+| + |F^-|}{|\Delta^+| + |\Delta^-|} \quad (16)$$

$$\beta_{eff} = \frac{2}{\pi k_{eff}} \frac{E_{loop}}{(|\Delta^+| + |\Delta^-|)^2} \quad (17)$$

where  $F^+$  and  $F^-$  are the peak positive and negative forces, measured at the cycle maximum positive and negative displacements  $\Delta^+$  and  $\Delta^-$ , respectively, as shown in Figure 2(c). The energy  $E_{loop}$  is the one dissipated per loading cycle, as it is schematically shown in Figure 2(d.)

To assess the uncertainty of the measurands  $k_{eff}$  and  $\beta_{eff}$  through Equation (9) it is necessary to calculate coefficients quantifying the sensitivity of the measurand  $Y$  to variations in the input variables  $x_i$ . Given the Equations (16) and (17), the sensitivity coefficients are defined by Equations (18) – (25)

$$\frac{\partial k_{eff}}{\partial F^+} = \frac{1}{\Delta^+ - \Delta^-} \quad (18)$$

$$\frac{\partial k_{eff}}{\partial F^-} = \frac{-1}{\Delta^+ - \Delta^-} \quad (19)$$

$$\frac{\partial k_{eff}}{\partial \Delta^+} = \frac{-(F^+ - F^-)}{(\Delta^+ - \Delta^-)^2} \quad (20)$$

$$\frac{\partial k_{eff}}{\partial \Delta^-} = \frac{F^+ - F^-}{(\Delta^+ - \Delta^-)^2} \quad (21)$$

$$\frac{\partial \beta_{eff}}{\partial E_{loop}} = \frac{2}{\pi k_{eff} (\Delta^+ - \Delta^-)^2} \quad (22)$$

$$\frac{\partial \beta_{eff}}{\partial k_{eff}} = -\frac{2}{\pi} \frac{E_{loop}}{k_{eff}^2 (\Delta^+ - \Delta^-)^2} \quad (23)$$

$$\frac{\partial \beta_{eff}}{\partial \Delta^+} = -\frac{4}{\pi} \frac{E_{loop}}{k_{eff} (\Delta^+ - \Delta^-)^3} \quad (24)$$

$$\frac{\partial \beta_{eff}}{\partial \Delta^-} = \frac{4}{\pi} \frac{E_{loop}}{k_{eff} (\Delta^+ - \Delta^-)^3} \quad (25)$$

It should be emphasized that in these expressions, the absolute value operator was removed, taking advantage of the fact that the force-displacement relationship can always be centered around the zero displacement reference. For the second-order Taylor approximation implemented in this study, the second derivatives of the measurands  $y_i$  (i.e.,  $k_{eff}$  and  $\beta_{eff}$ ) with respect to the input quantities  $x_i$  ( $F^+$ ,  $F^-$ ,  $\Delta^+$ ,  $\Delta^-$ ,  $k_{eff}$ , and  $E_{loop}$ ) are required to evaluate the  $\mathbf{g}'$  matrix. Given the lengthy derivations, these expressions are presented in Appendix B.

### III.3.3 Identifying uncertainty sources for input quantities $x_i$

As Equations (16) and (17) show, measurands  $k_{eff}$  and  $\beta_{eff}$  depend on four input quantities, namely  $F^+$ ,  $F^-$ ,  $\Delta^+$ , and  $\Delta^-$ , since the two additional quantities  $E_{loop}$  and  $k_{eff}$ , could be considered intermediate quantities in the calculation of  $\beta_{eff}$ , as their expected values and standard uncertainties also depend on force and displacement measurements. Hence, the uncertainty sources for the input quantities  $F^+$ ,  $F^-$ ,  $\Delta^+$ ,  $\Delta^-$ , and  $F_i$  (force measurements through the entire loop) need to be studied. A strong correlation is expected between all force-related input quantities (i.e.,  $F^+$ ,  $F^-$ , and  $F_i$ ) and between all displacement-related input quantities (i.e.,  $\Delta^+$  and  $\Delta^-$ ) since they are measured using the same instrumental setup.

Therefore, uncertainty quantification is based on the Equations (9) and (11) for correlated input quantities.

### III.3.3.1 Uncertainty sources for force measurement

The uncertainty sources for force measurement considered in this work are: (i) Type-A uncertainty arising from different measurements performed under *repeatability conditions*; (ii) Type-B uncertainty obtained from measurement tolerance of the force transducer (load-cell); (iii) Type-B uncertainty obtained from a calibration laboratory; and (iv) Type-B uncertainty inherent to the measurement instrument resolution.

### III.3.3.2 Uncertainty sources for displacement measurement

The uncertainty sources for displacement measurement considered in this work are: (i) Type-A uncertainty arising from different measurements performed under *repeatability conditions*; (ii) Type-B uncertainty obtained from measurement tolerance of the linear variable differential transducer (LVDT), (iii) Type-B uncertainty obtained from the calibration laboratory; and (iv) Type-B uncertainty inherent to measurement instrument resolution.

Figures 3 and 4 show the Ishikawa diagrams (cause-effect diagrams) with the considered uncertainties for  $k_{eff}$  and  $\beta_{eff}$  uncertainty assessment.

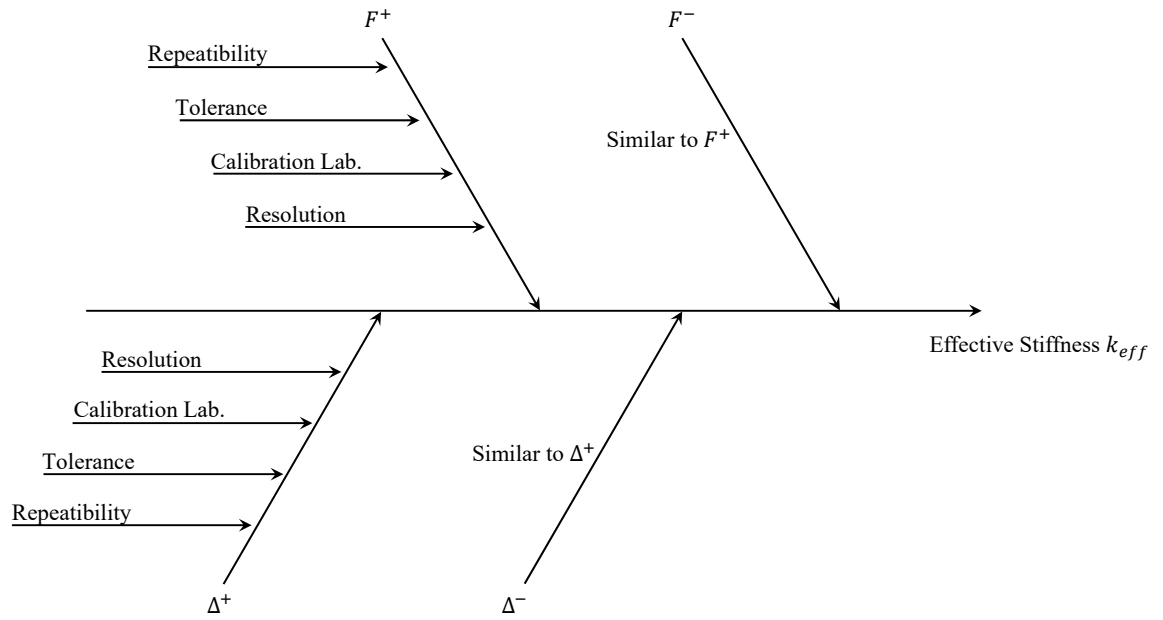


Figure III-3. Ishikawa Diagram for effective stiffness uncertainty quantification

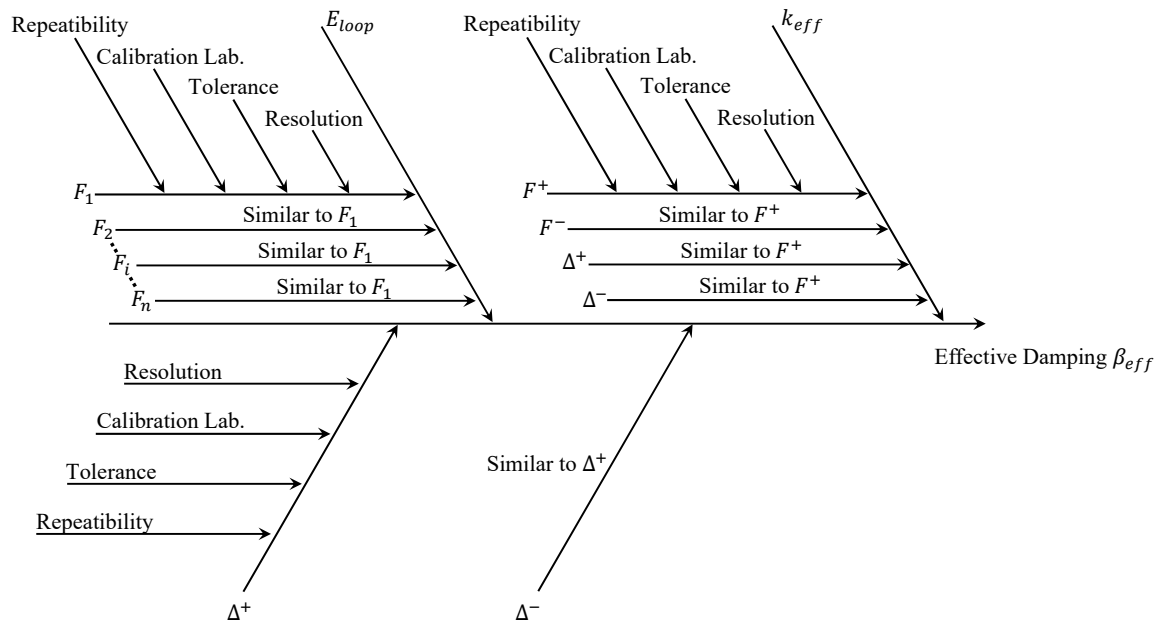


Figure III-4. Ishikawa Diagram for damping ratio uncertainty quantification

### III.3.4 Monte-Carlo simulation methodology

As stated in *GUM* Supplement 1 [4], any method used to estimate uncertainty should include the stages of formulation, propagation, and summarizing. Once the probability distributions of the input quantities are defined, they need to be propagated to the output quantity, i.e., the measurand. Monte-Carlo method (MCM in *GUM* terminology) performs this propagation numerically by performing random sampling from probability distributions of the input quantities. The following steps were implemented in this work:

- The number of trials  $M$  was defined. In this case, 200,000 trials were used. Because this simulation does not require a high amount of computational time, the adaptive Monte-Carlo method was not needed.
- $M$  realizations of the set of  $N$  input quantities were generated by sampling the assigned probability density functions. In our case, Gaussian distributions for the input variables were assumed, but two different calculation scenarios were studied, considering uncorrelated and correlated input quantities
- For each realization, the value of the measurand  $Y$  was calculated, using the corresponding model equation.
- The  $M$  generated values of the measurand  $Y$  were sorted to approximate the probability density function  $G$  of the measurand.
- An estimation of the measurand  $y$ , its standard uncertainty  $u(y)$ , and an appropriate coverage interval can be calculated from the probability density function  $G$ .

### III.4 Uncertainty Quantification – Results

The *GUM* methodology was applied to assess the uncertainty of the effective properties of all isolators in the dataset. Histograms for the expanded relative uncertainty (i.e., the ratio of property expanded uncertainty to property mean value) and an adjusted Gaussian probability density function are shown in Figures 5 through 8. To elucidate the methodology used for the implementation, Tables 2 to 5 show the uncertainty budget and the uncertainty quantification for the effective stiffness  $k_{eff}$  and the effective damping  $\beta_{eff}$  for a specific isolator hereafter referred to as Specimen 1 with an external diameter  $D_{ext} = 70 \text{ cm}$ , an internal diameter  $D_{int} = 10 \text{ cm}$ , and a total rubber height  $H_r = 16.2 \text{ cm}$ . As effective stiffness  $k_{eff}$  is calculated using Equation (16), the uncertainty sources for the input quantities  $F^+$ ,  $F^-$ ,  $\Delta^+$ , and  $\Delta^-$  need to be investigated. Results are shown only for shear strain  $\gamma = 1.5$ , but similar trends are observed with other shear deformations.

#### III.4.1 Specimen 1 uncertainties – *GUM* Method

##### III.4.1.1 Uncertainty sources for force measurements $F^+$ and $F^-$

*Uncertainty arising from several measurements under repeatability conditions*

The uncertainty arising from several measurements under *repeatability conditions* is evaluated as the sample standard deviation of the mean value with the expression:

$$u(F^+_{rep}) = \sqrt{\frac{\sum_{j=1}^n (F^+_j - \bar{F}^+)^2}{n-1}} \quad (26)$$

$$u(F^-_{rep}) = \sqrt{\frac{\sum_{j=1}^n (F^-_j - \overline{F^-})^2}{\frac{n-1}{n}}}$$

where  $F^+_j$  is the force value associated with the maximum displacement for testing cycle  $j$ ;  $\overline{F^+}$  is the mean value of the forces associated with the maximum displacements for all cycles; and  $n$  is the number of cycles considered in the analysis, i.e., five cycles ranging from first to fifth, or from second to sixth. As the measurand expected value is calculated by evaluating the model equation in the mean values of the input quantities, the standard deviation of the mean of the input quantity shall be used [28]. The uncertainty for  $F^-$  is calculated following an analogous procedure.

*Uncertainty arising from the force measuring device and its calibration tolerance*

As stated in the calibration report [30], the maximum acceptable deviation specified for the load cell is defined as 1% of the applied force value. Nevertheless, a more realistic uncertainty value of the maximum deviation effectively observed during the calibration procedure was assigned to  $F^+$  and  $F^-$ . This value was 0.64% of the measured value. Giving that  $\overline{F^+}$  and  $\overline{F^-}$  for the analyzed specimen are 235.8594 kN and -236.1563 kN, the standard uncertainty values are 1.5095 kN and 1.5114 kN, for  $\overline{F^+}$  and  $\overline{F^-}$ , respectively.

*Uncertainty arising from calibration laboratory uncertainty*

As stated in [30], the MTS calibration laboratory force measurement expanded uncertainty (U) is  $\pm 0.34\%$  of the applied force. This value was calculated using and coverage factor (k) of 2.0 for an estimated level of confidence of 95%. Given that coverage factor, the standard uncertainty is given by the expression:

$$u(F^+_{cal}) = \frac{U}{k} = \frac{\pm 0.34\%}{2} = \pm 0.17\% \quad (27)$$

resulting in a force uncertainty of  $\pm 0.17\%$  for the measured mean value of  $\bar{F}^+$  and  $\bar{F}^-$ .

*Uncertainty arising from measurement instrument resolution*

As stated in [30], the force measuring resolution is 0.002 kN. Given a uniform probability distribution function in the resolution interval, the standard uncertainty due to resolution is given by the expression

$$u(F^+_{res}) = \frac{0.002 \text{ kN}}{2\sqrt{3}} = 0.0012 \text{ kN} \quad (28)$$

As all the variability sources described above are deemed independent and mutually uncorrelated, it can be stated that:

$$\mathbf{u}^2(\mathbf{F}^+) = u^2(F^+_{rep}) + u^2(F^+_{tol}) + u^2(F^+_{cal}) + u^2(F^+_{res}) \quad (29)$$

$$\mathbf{u}^2(\mathbf{F}^-) = u^2(F^-_{rep}) + u^2(F^-_{tol}) + u^2(F^-_{cal}) + u^2(F^-_{res}) \quad (30)$$

The different uncertainty sources for  $F^+$  and  $F^-$  and their corresponding values are summarized in Table 2

Table III-2. Summary of standard uncertainty components for  $F^+$  and  $F^-$ 

Standard uncertainty component $u(x_i)$	Source of uncertainty	Distribution type	Value of standard uncertainty $u(x_i)$
<b><math>u(F^+)</math></b>			<b>2.6583 kN</b>
$u(F^+_{rep})$	Repeatability	Normal	2.1511 kN
$u(F^+_{tol})$	Tolerance	Normal	1.5095 kN
$u(F^+_{cal})$	Calibration	Normal	0.4009 kN
$u(F^+_{res})$	Resolution	Uniform	5.7735e-04 kN
<b><math>u(F^-)</math></b>			<b>2.6901 kN</b>
$u(F^-_{rep})$	Repeatability	Normal	2.1888 kN
$u(F^-_{tol})$	Tolerance	Normal	1.5114 kN
$u(F^-_{cal})$	Calibration	Normal	0.4015 kN
$u(F^-_{res})$	Resolution	Uniform	5.7735e-04 kN

### III.4.1.2 Uncertainty sources for force measurements $\Delta^+$ and $\Delta^-$

*Uncertainty arising from several measurements under repeatability conditions*

The uncertainty arising from several displacement measurements under *repeatability conditions* is evaluated as the sample standard deviation of the mean value with the expression:

$$u(\Delta^+_{rep}) = \sqrt{\frac{\sum_{j=1}^n (\Delta^+_j - \bar{\Delta}^+)^2}{n-1}} \quad (26)$$

$$u(\Delta^-_{rep}) = \sqrt{\frac{\sum_{j=1}^n (\Delta^-_j - \bar{\Delta}^-)^2}{n-1}}$$

where  $\Delta^+_j$  is the maximum displacement for testing cycle  $j$ ;  $\bar{\Delta}^+$  is the mean value of the maximum displacements for all cycles; and  $n$  is the number of cycles. All assumptions used in the uncertainty estimation of the forces were also applied for displacements.

*Uncertainty arising from the displacement measuring transducer tolerance*

As stated in the calibration report [31], the maximum acceptable deviation in the LVDT reading is 1% of the full-scale range. Since the full-scale range is 500 mm, the allowable deviation is 5 mm. Nonetheless, to assess a more realistic uncertainty value, the maximum deviation effectively observed during the calibration procedure was assigned to the  $\Delta^+$  and  $\Delta^-$  values. This number was 0.79% of the measured value. The averages  $\overline{\Delta^+}$  and  $\overline{\Delta^-}$  for the analyzed specimen are  $\pm 24.2453$  cm, and hence, the standard uncertainty values are  $\pm 0.1915$  cm, for  $\overline{\Delta^+}$  and  $\overline{\Delta^-}$ , respectively.

*Uncertainty arising from calibration laboratory uncertainty*

As stated in [31], the uncertainty of the supplied calibration data is equal or smaller than the greater of  $\pm 0.25\%$  of the reading or  $\pm 50\mu$  inches. In this case, the former value is at least one order of magnitude larger than the latter; thus, it was chosen for the uncertainty assessment. As informed in the calibration report, this value considers a coverage factor ( $k$ ) of 2.0 for an estimated level of confidence of 95%. Given that coverage factor, the standard uncertainty is given by the expression:

$$u(\Delta^+_{cal}) = \frac{U}{k} = \frac{\pm 0.25\%}{2} = 0.125\% \quad (27)$$

resulting in a displacement uncertainty of 0.125% of the measured mean value of  $\overline{\Delta^+}$  and  $\overline{\Delta^-}$ .

*Uncertainty arising from measurement instrument resolution*

As stated in [31], the displacement measurement resolution is 0.001 mm. Assuming a uniform probability distribution function for the resolution interval, the standard uncertainty due to resolution is given by the expression:

$$u(\Delta^+_{res}) = \frac{0.0001 \text{ cm}}{2\sqrt{3}} = 2.8868 \cdot 10^{-5} \text{ cm} \quad (28)$$

As all the variability sources described above are independent and mutually uncorrelated, the combined standard uncertainty may be written as:

$$\mathbf{u}^2(\Delta^+) = u^2(\Delta^+_{rep}) + u^2(\Delta^+_{tol}) + u^2(\Delta^+_{cal}) + u^2(\Delta^+_{res}) \quad (29)$$

$$\mathbf{u}^2(\Delta^-) = u^2(\Delta^-_{rep}) + u^2(\Delta^-_{tol}) + u^2(\Delta^-_{cal}) + u^2(\Delta^-_{res}) \quad (30)$$

The different uncertainty sources for  $\Delta^+$  and  $\Delta^-$  and their corresponding values are summarized in Table 3

Table III-3. Summary of standard uncertainty components for  $\Delta^+$  and  $\Delta^-$

Standard uncertainty component $u(x_i)$	Source of uncertainty	Distribution type	Value of standard uncertainty $u(x_i)$
<b><math>u(\Delta^+)</math></b>			<b>0.1939 cm</b>
$u(\Delta^+_{rep})$	Repeatability	Normal	0.0013 cm
$u(\Delta^+_{tol})$	Tolerance	Normal	0.1915 cm
$u(\Delta^+_{cal})$	Calibration	Normal	0.0303 cm
$u(\Delta^+_{res})$	Resolution	Uniform	2.8868e-05 cm
<b><math>u(\Delta^-)</math></b>			<b>0.1939 cm</b>
$u(\Delta^-_{rep})$	Repeatability	Normal	0.0013 cm
$u(\Delta^-_{tol})$	Tolerance	Normal	0.1915 cm
$u(\Delta^-_{cal})$	Calibration	Normal	0.0303 cm
$u(\Delta^-_{res})$	Resolution	Uniform	2.8868e-05 cm

Based on these results, the propagation of the standard uncertainties of  $F^+$ ,  $F^-$ ,  $\Delta^+$  and  $\Delta^-$  to the uncertainty in the effective stiffness  $k_{eff}$  is carried out. Sensitivity coefficients in Equations (18) – (21) are evaluated for the mean values of the input quantities and shown in

the fourth column of Table 4. Finally, evaluating equation (6), the expanded uncertainty for the measurand  $k_{eff}$  is 0.3433 kN/cm. As the expected value of the measurand is 9.7342 kN/cm, the relative expanded uncertainty is 3.53 %. For assessing the coverage factor, that applied over the standard uncertainty results in the expanded uncertainty, the well-known Welch-Satterthwaite formula [2,28] is used.

Table III-4. Summary of standard uncertainty components for  $k_{eff}$

Standard uncertainty component $u(x_i)$	Expected value $\bar{x}_i$	Value of standard uncertainty $u(x_i)$	$c_i = \partial k_{eff} / \partial x_i$ (evaluated at $\bar{x}_i$ )	Value of combined expanded uncertainty $u(k_{eff})$	Value of relative expanded uncertainty %
<b><math>u(k_{eff})</math></b>	<b>9.7342 kN/cm</b>			<b>0.3433 kN/cm</b>	<b>3.53 %</b>
$u(F^+)$	235.8518 kN	2.6583 kN	0.0206 1/cm		
$u(F^-)$	-236.1639 kN	2.6901 kN	-0.0206 1/cm		
$u(\Delta^+)$	24.2453 cm	0.1939 cm	-0.2007 kN/cm <sup>2</sup>		
$u(\Delta^-)$	-24.2453 cm	0.1939 cm	0.2007 kN/cm <sup>2</sup>		

It is interesting to note the signs of the 4<sup>th</sup> column terms. Since they represent  $\partial k_{eff} / \partial x_i$ , for  $F^+$  the sensitivity of  $k_{eff}$  must be positive since an increase in  $F^+$  produces an increase in  $k_{eff}$ . The opposite occurs for  $F^-$  given its algebraic sign. On the other hand, for  $\partial k_{eff} / \partial \Delta^+$ , an increase in  $\Delta^+$  produces a decrease in  $k_{eff}$  at this level of deformation (24.2453 cm), and the opposite occurs for  $\Delta^-$ . Moreover, the uncertainty of  $k_{eff}$  was calculated with Equation (11) to include the second-order term in the Taylor polynomial approximation. However, there is no relevant difference in the uncertainty estimation by including the second-order terms, since in this case, they are at least four orders of magnitude smaller than the first-order terms.

The uncertainty in the effective isolator damping  $\beta_{eff}$  was also calculated. As can be seen from Equation (17), the assessment of the uncertainty of  $\beta_{eff}$  requires an intermediate step, which is the evaluation of the uncertainty of  $k_{eff}$ , as explained above. Furthermore, the evaluation of the uncertainty in the energy term  $E_{loop}$  also depends on the measured values of forces and displacements.

The uncertainty evaluation of  $E_{loop}$  requires a different methodology, as  $E_{loop}$  corresponds to the area enclosed by the force-displacement curve in a full cycle. The proposed method resamples the displacement values of the force-displacement curve at a new interval, say 0.1 cm. Once the displacements are resampled, a new set of input forces  $F_1, F_2, F_3, \dots, F_p$ , where  $p$  is the number of points defining the resampled curve, need to be considered. For each one of these new input quantities, there are as many measured values of force  $F_i$  as cycles were carried out during the test. Then, the uncertainty of  $E_{loop}$  was evaluated using the model of Equation (31) and the trapezoidal rule for cycle  $j$ :

$$(E_{loop})_j = \sum_{i=1}^{p-1} \frac{1}{2} ((F_i)_j + (F_{i+1})_j) \Delta_{int} \quad (31)$$

Where  $(E_{loop})_j$  is the dissipated hysteretic energy in cycle  $j$ ; and  $\Delta_{int}$  is the displacement interval. Indeed, several values of  $\Delta_{int}$  were studied to evaluate how this parameter influences the calculation of  $(E_{loop})_j$  and its associated uncertainty. It was observed that for  $\Delta_{int} \leq 1mm$ , there are no differences in the results. Table 5 summarizes the expected values for each of the input quantities used in computing  $\beta_{eff}$ , for the same isolator specimen used in the previous section.

Table III-5. Summary of standard uncertainty components for  $\beta_{eff}$ 

Standard uncertainty component $u(x_i)$	Expected value $\bar{x}_i$	Value of standard uncertainty $u(x_i)$	$c_i = \partial\beta_{eff}/\partial x_i$ (evaluated at $\bar{x}_i$ )	Value of combined expanded uncertainty $u(\beta_{eff})$	Value of relative expanded uncertainty %
$u(\beta_{eff})$	<b>0.1239</b>			<b>0.0045</b>	<b>3.61 %</b>
$u(E_{loop})$	4.4538e03 kN cm	17.1108 kN cm	2.781e-5 1/kN cm		
$u(k_{eff})$	9.7342 kN	0.1600 kN/cm	-0.0127 cm/kN		
$u(\Delta^+)$	24.2453 cm	0.1939 cm	-0.0051 1/cm		
$u(\Delta^-)$	-24.2453 cm	0.1939 cm	0.0051 1/cm		

The expanded uncertainty was also evaluated by implementing the second-order Taylor approximation in Equation (11). In this particular case, a slight difference of 1% between the second-order and the first-order approximation was observed.

#### III.4.2 Specimen 1 uncertainties – Comparison between *GUM* and Monte-Carlo method.

For the case of Specimen 1, as well as for the complete dataset used in this analysis, an excellent agreement was observed between the results from both methodologies, with a maximum difference of 0.95%. Table 6 presents the resulting ratios between both approaches for the effective stiffness and the effective damping, and all shear strains included in the analysis. These error ratios were defined as  $(GUM - MCM)/GUM$ .

Table III-6. Percentual difference ratio between *GUM* and Monte-Carlo uncertainty estimation for Specimen 1

Shear Strain	Effective Stiffness	Effective Damping
0.25	0.28%	0.68%
0.50	0.91%	0.19%
1.00	0.15%	0.95%
1.50	0.03%	0.64%

The influence of the linear correlation between input quantities in the measurand uncertainty can be easily assessed using the Monte-Carlo method. Thus, Monte-Carlo simulations were performed considering uncorrelated and correlated input quantities. For the correlated case, the realizations were constrained by the covariance matrix of the observed data. On average, the uncertainty of the measurand is 35% higher if the correlation between input quantities is considered in the analysis.

### III.4.3 Dataset uncertainty results

Figures (5) and (6) show data histograms for the complete dataset of 2,498 seismic isolators and a calibrated normal probability distribution function for the expanded relative uncertainty in  $k_{eff}$  and  $\beta_{eff}$ , respectively. Only one Type-A uncertainty source was considered (several measurements under *repeatability conditions*). As prescribed in NCh 2745 [24], properties and uncertainties were evaluated considering deformation cycles 2 through 6, being these histograms displayed in subplots (a) and (b) for the four shear deformations considered. For comparison purposes, properties and uncertainties were also evaluated considering cycles 1 through 5, being these results displayed in subplots (c) and (d).

The selection of the cycles to generate the averages has a predictable consequence in the uncertainty of the effective stiffness  $k_{eff}$  since, the mean uncertainties for the *unscragged* case (averaging cycles 1 through 5) are higher than the ones for the *scragged* case (cycles 2 through 6). When comparing standard deviations of the uncertainty, a clear trend is noticed as they are consistently higher in the *unscragged* case, with ratios ranging from 1.40 to 1.94 times relative to the *scragged* case. Furthermore, on average, the mean uncertainties

observed for Compound 1 are slightly but consistently higher than the ones for Compound 2.

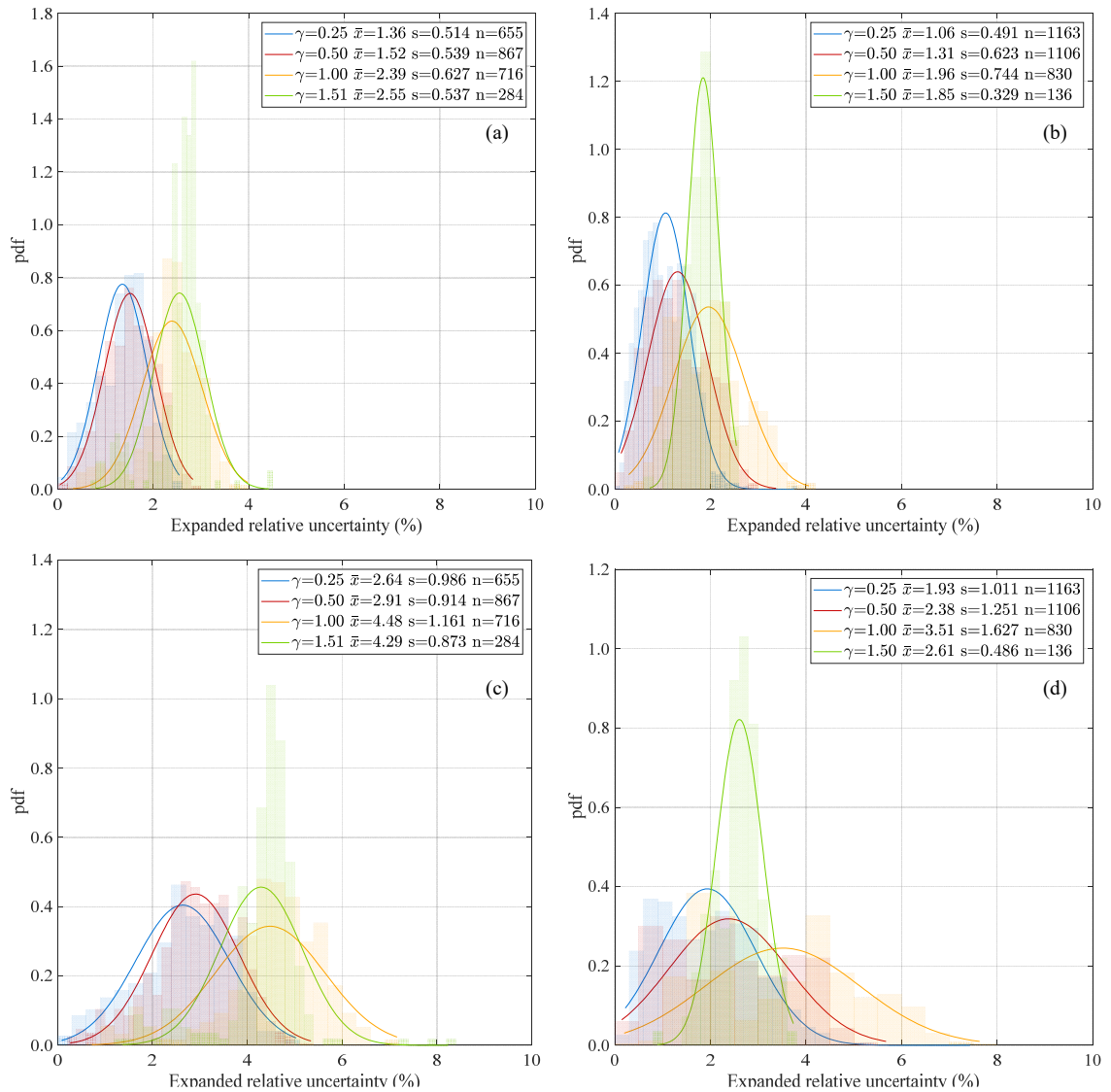


Figure III-5. Expanded relative uncertainty in equivalent stiffness  $k_{eff}$  for the seismic isolators dataset, considering only intercycle uncertainty: (a) Compound 1, using cycles 2 through 6, (b) Compound 2, using cycles 2 through 6, (c) Compound 1, using cycles 1 through 5, and (d) Compound 2, using cycles 1 through 5 (legend notation,  $\bar{x} = \overline{k_{eff}}$ ,  $s = \sigma_{k_{eff}}$ , and  $n$  = number of samples)

Figure 6 shows data histograms for the expanded relative uncertainty of  $\beta_{eff}$ . Just as it was observed for  $k_{eff}$ , the mean uncertainties for Compound 1 are mildly but consistently higher than the mean uncertainties for Compound 2. Nevertheless, there are no consistent trends between the means of the *scragged* and *unscragged* cases. Uncertainty assessment of effective damping  $\beta_{eff}$  involves measured values from the whole force-displacement curve, thus reducing the *scragging* relevance, since the *scragged* and *unscragged* curves are similar for low displacement levels. On the other hand, uncertainty assessment of the effective stiffness  $k_{eff}$  only considers the extreme values of the curves, thus leading to much more noticeable differences between the *scragged* and *unscragged* curves.

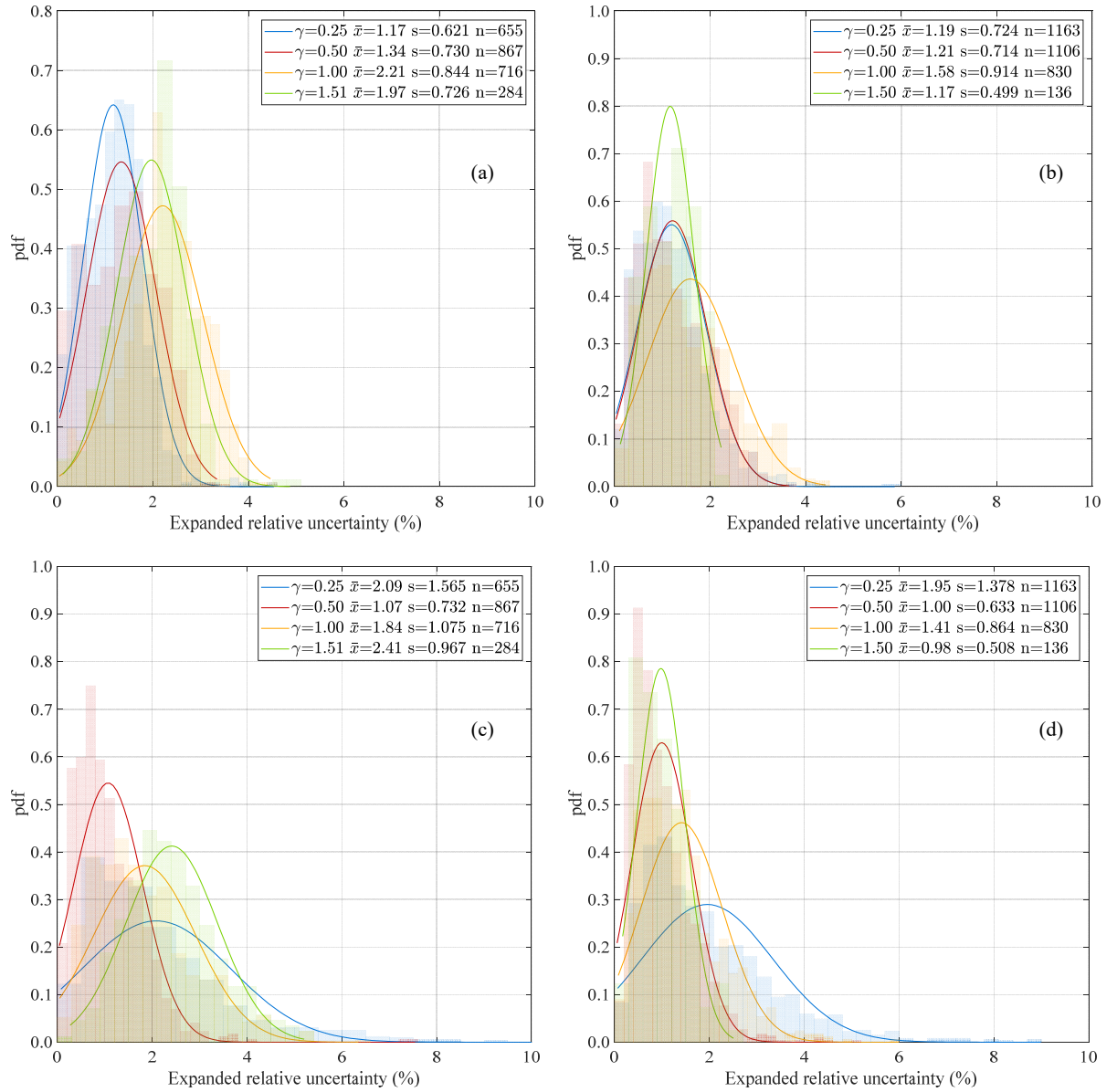


Figure III-6. Expanded relative uncertainty for the effective damping  $\beta_{eff}$  of the seismic isolator dataset, considering only intercycle uncertainty: (a) cycles 2 to 6 of Compound 1, (b) cycles 2 to 6 of Compound 2, (c) cycles 1 to 5 of Compound 1, and (d) cycles 1 to 5 of Compound 2 (legend notation,  $\bar{x} = \overline{\beta_{eff}}$ ,  $s = \sigma_{\beta_{eff}}$ , and  $n$  = number of samples)

Figures (7) and (8) show histograms analogous to the ones presented in Figures (5) and (6), but considering Type B uncertainty sources of tolerance, calibration, and resolution, as detailed in the example specimen, in addition to the variability under *repeatability conditions* (uncertainty source Type A).

Results from uncertainties in effective stiffness  $k_{eff}$  are shown in Figure 7. *Unscragged* mean uncertainties surpass their *scragged* counterpart values with ratios ranging from 1.32 to 1.82, and from 1.15 to 1.68, for Compounds 1 and 2, respectively. These ratios can be predicted as linear functions of shear strain  $\gamma$ , for values of  $\gamma$  ranging from 0.25 to 1.0. Standard deviations of the uncertainty are consistently higher for the *unscragged* case.

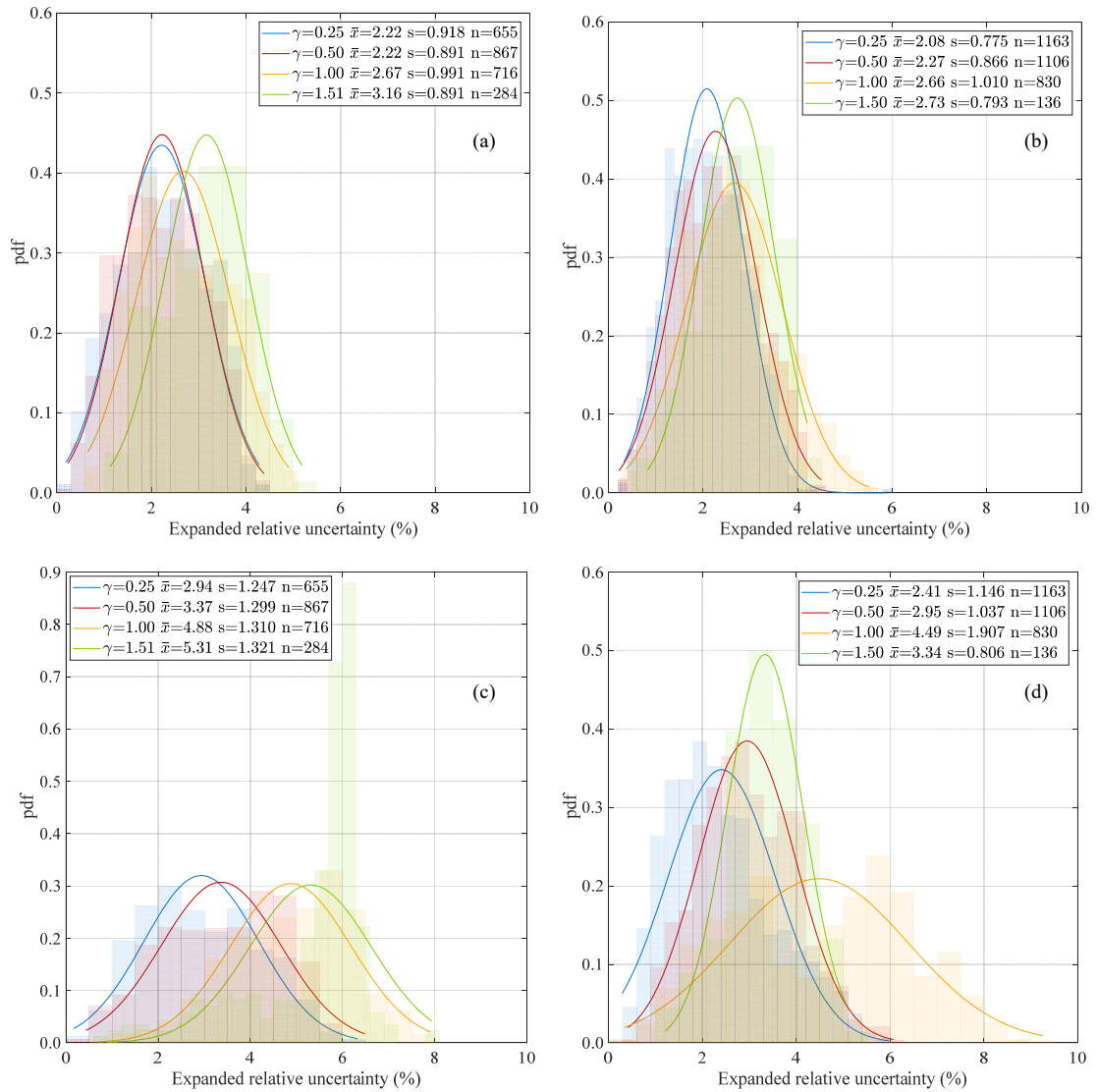


Figure III-7. Expanded relative uncertainty in equivalent stiffness  $k_{eff}$  for the seismic isolators dataset, considering intercycle uncertainty and Type B uncertainty sources: (a) compound 1, using cycles 2 through 6, (b) compound 2, using cycles 2 through 6, (c) compound 1, using cycles 1 through 5, and (d) compound 2, using cycles 1 through 5 (legend notation,  $\bar{x} = \overline{k_{eff}}$ ,  $s = \sigma_{k_{eff}}$ , and  $n$  = number of samples)

Results of Figure 8 present the effective damping  $\beta_{eff}$  and do not show a clear trend between mean uncertainties for the *scragged* and *unscragged* cases. Probability density functions

look similar for all the cases under analysis, showing that uncertainty in  $\beta_{eff}$  is less sensitive to differences in Compounds, shear strains, or cycle selection than uncertainty in  $k_{eff}$ .

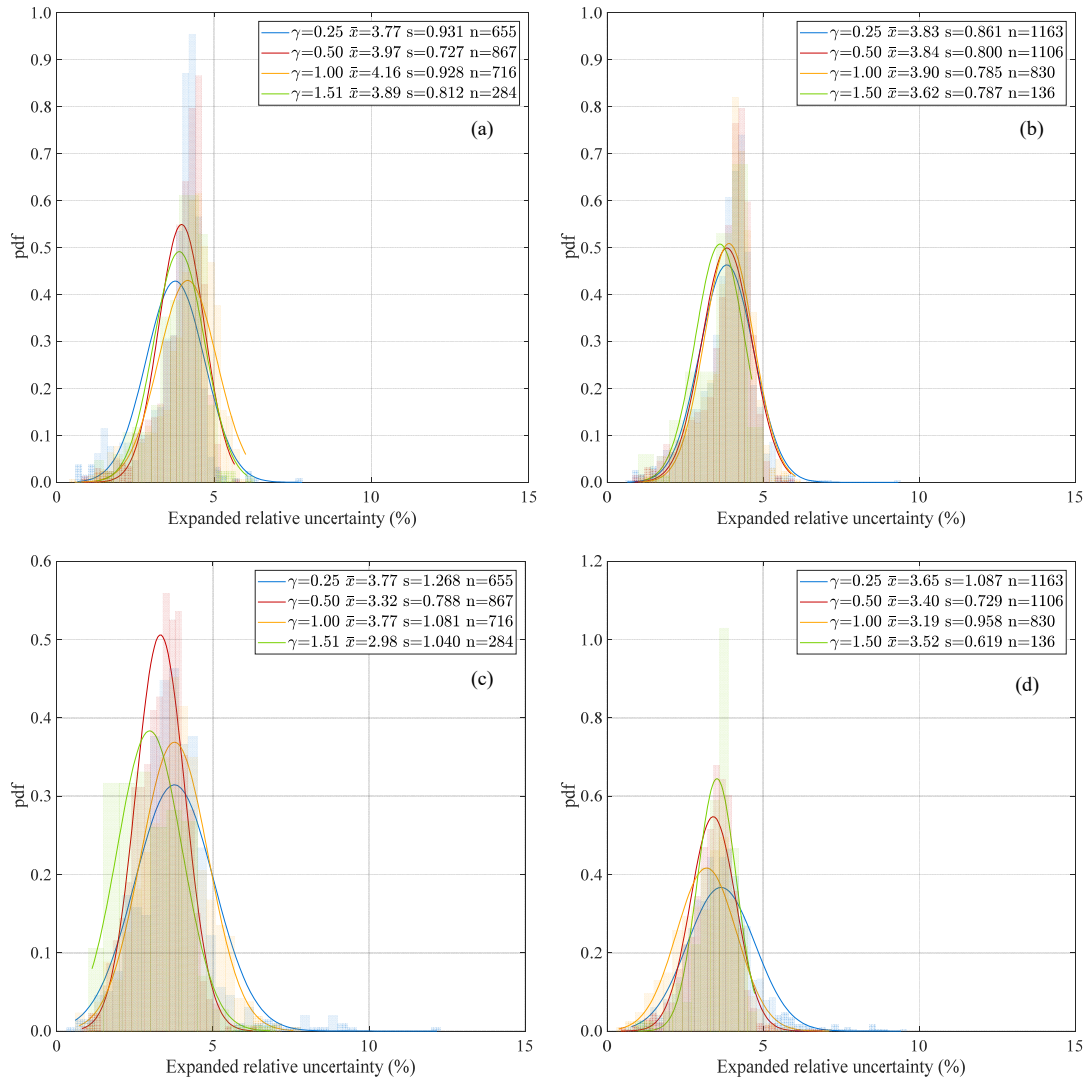


Figure III-8. Expanded relative uncertainty of the equivalent damping ratio  $\beta_{eff}$  for the seismic isolators dataset, considering intercycle uncertainty and Type B uncertainty sources: (a) Cycles 2 through 6 of Compound 1, (b) Cycles 2 through 6 of Compound 2, (c) Cycles 1 through 5 of Compound 1, and (d) Cycles 2 through 5 of Compound 2 (legend notation,  $\bar{x} = \overline{\beta_{eff}}$ ,  $s = \sigma_{\beta_{eff}}$ , and  $n$  = number of samples)

It could be stated that observations from data in Figures (7) and (8) are strongly dependent on the laboratory setup, rubber compounds characteristics, and manufacturing techniques. However, some trends in these results, such as the independence of the uncertainty  $\beta_{eff}$  with shear strain level, compound type, or cycle selection, might also appear in isolators manufactured from different companies and should be further investigated.

The mean uncertainties, the uncertainty standard deviations, and the maximum observed uncertainties for all isolators in the dataset are summarized in Tables (7) to (10) for both effective properties ( $k_{eff}$  and  $\beta_{eff}$ ), both manufacturing compounds, and typical values of shear strain. Results are presented for the *scragged* and *unscragged* cases, i.e., averaging cycles 2 to 6 and 1 to 5, respectively.

Table III-7. Expanded relative uncertainty in equivalent stiffness  $k_{eff}$ , considering only intercycle (Type A) uncertainty.

Averaging cycles 2 to 6								
Compound 1					Compound 2			
Strain	$\bar{U}(\%)$	$\sigma_U(\%)$	max $U(\%)$	$N$	$\bar{U}(\%)$	$\sigma_U(\%)$	max $U(\%)$	$N$
$\gamma = 0.25$	1.36	0.514	2.54	655	1.06	0.491	3.76	1163
$\gamma = 0.50$	1.52	0.539	2.83	867	1.31	0.623	3.37	1106
$\gamma = 1.00$	2.39	0.627	3.98	716	1.96	0.744	4.06	830
$\gamma = 1.50$	2.55	0.537	4.41	284	1.85	0.329	2.55	136
Averaging cycles 1 to 5								
Compound 1					Compound 2			
Strain	$\bar{U}(\%)$	$\sigma_U(\%)$	max $U(\%)$	$N$	$\bar{U}(\%)$	$\sigma_U(\%)$	max $U(\%)$	$N$
$\gamma = 0.25$	2.64	0.986	5.03	655	1.93	1.011	7.43	1163
$\gamma = 0.50$	2.91	0.914	5.34	867	2.38	1.251	5.68	1106
$\gamma = 1.00$	4.48	1.161	7.16	716	3.51	1.627	7.63	830
$\gamma = 1.50$	4.29	0.873	8.23	284	2.61	0.486	3.74	136

Table III-8. Expanded relative uncertainty in equivalent damping  $\beta_{eff}$ , considering only intercycle (Type A) uncertainty.

Averaging cycles 2 to 6								
Compound 1					Compound 2			
Strain	$\bar{U}(\%)$	$\sigma_{U(\%)}$	max $U(\%)$	$N$	$\bar{U}(\%)$	$\sigma_{U(\%)}$	max $U(\%)$	$N$
$\gamma = 0.25$	1.17	0.621	4.53	655	1.19	0.724	5.87	1163
$\gamma = 0.50$	1.34	0.730	3.34	867	1.21	0.714	3.66	1106
$\gamma = 1.00$	2.21	0.844	4.46	716	1.58	0.914	4.42	830
$\gamma = 1.50$	1.97	0.726	4.87	284	1.17	0.499	2.23	136
Averaging cycles 1 to 5								
Compound 1					Compound 2			
Strain	$\bar{U}(\%)$	$\sigma_{U(\%)}$	max $U(\%)$	$N$	$\bar{U}(\%)$	$\sigma_{U(\%)}$	max $U(\%)$	$N$
$\gamma = 0.25$	2.09	1.565	11.48	655	1.95	1.378	8.99	1163
$\gamma = 0.50$	1.07	0.732	7.54	867	1.00	0.633	5.00	1106
$\gamma = 1.00$	1.84	1.075	6.34	716	1.41	0.864	5.99	830
$\gamma = 1.50$	2.41	0.967	5.21	284	0.98	0.508	2.51	136

Table III-9. Expanded relative uncertainty in equivalent stiffness  $k_{eff}$ , considering intercycle uncertainty (Type A) and Type B uncertainty sources.

Averaging cycles 2 to 6								
Compound 1					Compound 2			
Strain	$\bar{U}(\%)$	$\sigma_{U(\%)}$	max $U(\%)$	$N$	$\bar{U}(\%)$	$\sigma_{U(\%)}$	max $U(\%)$	$N$
$\gamma = 0.25$	2.22	0.918	4.28	655	2.08	0.775	5.88	1163
$\gamma = 0.50$	2.22	0.891	4.38	867	2.27	0.866	4.50	1106
$\gamma = 1.00$	2.67	0.991	4.91	716	2.66	1.010	5.51	830
$\gamma = 1.50$	3.16	0.891	5.19	284	2.73	0.793	4.20	136
Averaging cycles 1 to 5								
Compound 1					Compound 2			
Strain	$\bar{U}(\%)$	$\sigma_{U(\%)}$	max $U(\%)$	$N$	$\bar{U}(\%)$	$\sigma_{U(\%)}$	max $U(\%)$	$N$
$\gamma = 0.25$	2.94	1.247	6.33	655	2.41	1.146	5.97	1163
$\gamma = 0.50$	3.37	1.299	6.48	867	2.95	1.037	6.07	1106
$\gamma = 1.00$	4.88	1.310	7.90	716	4.49	1.907	9.26	830
$\gamma = 1.50$	5.31	1.321	7.94	284	3.34	0.508	5.06	136

Table III-10. Expanded relative uncertainty in equivalent damping  $\beta_{eff}$ , considering intercycle uncertainty (Type A) and Type B uncertainty sources.

Averaging cycles 2 to 6								
Compound 1					Compound 2			
Strain	$\bar{U}(\%)$	$\sigma_{U(\%)}$	max $U(\%)$	$N$	$\bar{U}(\%)$	$\sigma_{U(\%)}$	max $U(\%)$	$N$
$\gamma = 0.25$	3.77	0.931	7.80	655	3.83	0.861	9.33	1163
$\gamma = 0.50$	3.97	0.727	5.65	867	3.84	0.800	5.90	1106
$\gamma = 1.00$	4.16	0.928	6.01	716	3.90	0.785	6.04	830
$\gamma = 1.50$	3.89	0.812	6.06	284	3.62	0.787	4.64	136
Averaging cycles 1 to 5								
Compound 1					Compound 2			
Strain	$\bar{U}(\%)$	$\sigma_{U(\%)}$	max $U(\%)$	$N$	$\bar{U}(\%)$	$\sigma_{U(\%)}$	max $U(\%)$	$N$
$\gamma = 0.25$	3.77	1.268	12.18	655	3.65	1.087	9.41	1163
$\gamma = 0.50$	3.32	0.788	6.27	867	3.40	0.729	6.90	1106
$\gamma = 1.00$	3.77	1.081	7.58	716	3.19	0.958	7.11	830
$\gamma = 1.50$	2.98	1.040	6.84	284	3.52	0.619	4.73	136

### III.5 Conclusions

This research work quantifies the uncertainty on the measured-by-test effective stiffness and damping ratio of a large dataset of 2,498 elastomeric seismic isolators, considering the methodology proposed by the *GUM* and using Monte-Carlo simulation. It is concluded that results from both approaches are, to all practical effects, equivalent.

A thorough analysis of the seismic-code requirement to neglect the effect of scragging in isolator properties, by eliminating the first deformation cycle from the physical isolator property calculations, was carried out. As it should be expected, stiffness results show that in the *unscragged* case, the mean and variability of the uncertainty are higher than those for the *scragged* case. On the other hand, there is no clear trend when comparing the effective damping uncertainties for the *unscragged* and *scragged* cases, since the complete force-displacement cycle is included in the uncertainty calculation, which reduces the scragging

effect. Mean relative-expanded uncertainties at the design shear strain for the *unscragged* case are 4.67% and 3.15% for stiffness and damping, respectively. If the *scragged* cycles are considered, these values change to 3.02% and 3.80%, respectively.

If repeatability is considered as the only uncertainty source (Type A), the dataset maximum relative-expanded uncertainty values are 8% and 11% for the effective stiffness and damping, respectively. The addition of Type B uncertainty sources increases these maximum values to 9% and 12%.

Finally, it was proven that for the functional forms used to assess the effective stiffness and effective damping uncertainties, the first-order Taylor approximation is sufficiently accurate. Moreover, differences between uncertainties calculated with *GUM* first-order approximation, *GUM* second-order approximation, and Monte-Carlo simulations were negligible.

### **Acknowledgments**

This research was funded by CONICYT Doctorado Nacional 21161027, the National Research Center for Integrated Natural Disaster Management CONICYT /FONDAP/15110017, and CONICYT/FONDECYT/1170836.

### **References**

1. Birge RT. The Propagation of Errors. *American Journal of Physics* 1939; 7(6): 351–357. DOI: 10.1119/1.1991484.

2. BIPM, IEC, IFCC, ILAC, ISO, IUPAC I and O. Guide to the Expression of Uncertainty in Measurement, JCGM 100:2008 (GUM 1995 with minor corrections). *International Organization for Standardization Geneva ISBN* 2008.
3. Stant LT, Aaen PH, Ridler NM. Comparing methods for evaluating measurement uncertainty given in the JCGM ‘Evaluation of Measurement Data’ documents. *Measurement: Journal of the International Measurement Confederation* 2016; **94**(2016): 847–851. DOI: 10.1016/j.measurement.2016.08.015.
4. BIPM, IEC, IFCC, ILAC, ISO, IUPAC I and O. Supplement 1 to the “Guide to the Expression of Uncertainty in Measurement” - Propagation of distributions using a Monte Carlo method, JCGM 101:2008. *International Organization for Standardization Geneva ISBN* 2008.
5. BIPM, IEC, IFCC, ILAC, ISO, IUPAC I and O. International Vocabulary of Metrology - Basic and General Concepts and Associated Terms (VIM), JCGM 200:2012. *International Organization for Standardization Geneva ISBN* 2012(Vim): 104. DOI: 10.1016/0263-2241(85)90006-5.
6. Da Silva Hack P, Ten Caten CS. Measurement uncertainty: Literature review and research trends. *IEEE Transactions on Instrumentation and Measurement* 2012; **61**(8): 2116–2124. DOI: 10.1109/TIM.2012.2193694.
7. Mauris G, Lasserre V, Foulloy L. A fuzzy approach for the expression of uncertainty in measurement. *Measurement: Journal of the International Measurement Confederation* 2001; **29**(3): 165–177. DOI: 10.1016/S0263-2241(00)00036-1.
8. Ferrero A, Salicone S. The random-fuzzy variables: A new approach to the expression of uncertainty in measurement. *IEEE Transactions on Instrumentation and Measurement* 2004; **53**(5): 1370–1377. DOI: 10.1109/TIM.2004.831506.
9. Shahanaghi K, Nakhjiri P. A new optimized uncertainty evaluation applied to the Monte-Carlo simulation in platinum resistance thermometer calibration. *Measurement: Journal of the International Measurement Confederation* 2010; **43**(7): 901–911. DOI: 10.1016/j.measurement.2010.03.008.

10. Theodorou D, Meligotsidou L, Karavoltzos S, Burnetas A, Dassenakis M, Scoullou M. Comparison of ISO-GUM and Monte Carlo methods for the evaluation of measurement uncertainty: Application to direct cadmium measurement in water by GFAAS. *Talanta* 2011; **83**(5): 1568–1574. DOI: 10.1016/j.talanta.2010.11.059.
11. Chen A, Chen C. Comparison of GUM and Monte Carlo methods for evaluating measurement uncertainty of perspiration measurement systems. *Measurement: Journal of the International Measurement Confederation* 2016; **87**: 27–37. DOI: 10.1016/j.measurement.2016.03.007.
12. Junga R, Chudy P, Pospolita J. Uncertainty estimation of the efficiency of small-scale boilers. *Measurement: Journal of the International Measurement Confederation* 2017; **97**: 186–194. DOI: 10.1016/j.measurement.2016.11.011.
13. Moona G, Sharma R, Kumar H. Evaluation of uncertainty of measurement of shadow mask dot pitch using different approaches. *Transactions of the Institute of Measurement and Control* 2018; **40**(7): 2428–2435. DOI: 10.1177/0142331217707367.
14. Link A, Täubner A, Wabinski W, Bruns T, Elster C. Modelling accelerometers for transient signals using calibration measurements upon sinusoidal excitation. *Measurement: Journal of the International Measurement Confederation* 2007; **40**(9–10): 928–935. DOI: 10.1016/j.measurement.2006.10.011.
15. Bringmann B, Knapp W. Machine tool calibration: Geometric test uncertainty depends on machine tool performance. *Precision Engineering* 2009; **33**(4): 524–529. DOI: 10.1016/j.precisioneng.2009.02.002.
16. Leyi G, Wei Z, Jing Z, Songling H. Mechanics analysis and simulation of material Brinell hardness measurement. *Measurement: Journal of the International Measurement Confederation* 2011; **44**(10): 2129–2137. DOI: 10.1016/j.measurement.2011.07.024.
17. Mahmoud GM, Hegazy RS. Comparison of GUM and Monte Carlo methods for the uncertainty estimation in hardness measurements. *International Journal of Metrology and Quality Engineering* 2017; **8**: 1–9. DOI: 10.1051/ijmqe/2017014.

18. Guimaraes Couto PR, Carreteiro J, de Oliveir SP. Monte Carlo Simulations Applied to Uncertainty in Measurement. *Theory and Applications of Monte Carlo Simulations* 2013. DOI: 10.5772/53014.
19. Kuhinek D, Zorić I, Hrženjak P. Measurement uncertainty in testing of uniaxial compressive strength and deformability of rock samples. *Measurement Science Review* 2011. DOI: 10.2478/v10048-011-0021-2.
20. Godina A, Acko B. Measurement uncertainty analysis for calibration of gauge blocks. *Procedia Engineering* 2014; **69**: 191–198. DOI: 10.1016/j.proeng.2014.02.220.
21. Salah B, Slimane Z, Zoheir M, Jurgen B. Uncertainty estimation of mechanical testing properties using sensitivity analysis and stochastic modelling. *Measurement: Journal of the International Measurement Confederation* 2015; **62**: 149–154. DOI: 10.1016/j.measurement.2014.10.036.
22. Fabricio DAK, Hack P da S, Caten CS ten. Estimation of the measurement uncertainty in the anisotropy test. *Measurement: Journal of the International Measurement Confederation* 2016; **93**: 303–309. DOI: 10.1016/j.measurement.2016.07.027.
23. American Society of Civil Engineers (ASCE). *Minimum Design Loads for Buildings and Other Structures, ASCE/SEI 7-16*. 2017.
24. Instituto Nacional de Normalización (INN). *NCh2745.Of2013 - Análisis y diseño de Edificios con Aislación Sísmica (In Spanish)*. 2013.
25. Mullins L. Softening of rubber by displacement. *Rubber Chemistry and Technology* 1969; **42**(1): 339–362.
26. Anil K. Chopra. *Dynamics of Structures Theory and Applications to Earthquake Engineering*. Fourth Edi. Prentice Hall; 2012.
27. De la Llera JC, Luders C, Leigh P, Sady H. Analysis, testing, and implementation of seismic isolation of buildings in Chile. *Earthquake Engineering and Structural Dynamics* 2004; **33**(5): 543–574. DOI: 10.1002/eqe.360.

28. Lira I. *Evaluating the Measurement Uncertainty: Fundamentals and Practical Guidance*. 2002.
29. Mekid S, Vaja D. Propagation of uncertainty: Expressions of second and third order uncertainty with third and fourth moments. *Measurement: Journal of the International Measurement Confederation* 2008; **41**(6): 600–609. DOI: 10.1016/j.measurement.2007.07.004.
30. MTS System Corporation. *Certificate of Calibration, SN10320683:1280148971*. 2010.
31. MTS System Corporation. *Certificate of Calibration, ACT3-182*. 2010.

## IV. THE EFFECT OF SPECTRAL SHAPE ON DAMPING MODIFICATION FACTORS

Sebastián Miranda,<sup>a),c)</sup> M.EERI, Eduardo Miranda,<sup>b)</sup> M.EERI and Juan Carlos de la Llera,<sup>a)</sup> M.EERI

### IV.1 Abstract

The main objective of this study is to investigate the effect of spectral shape on damping modification factors  $\eta$  used in equivalent static and response spectrum analyses of structures with damping ratios that are different from 5% critical damping. Record-to-record variability of  $\eta$  is also evaluated through a statistical analysis of 5,270 ground motions records from 1,137 interface earthquakes recorded in Chile. The effect of spectral shape is studied by using recently developed spectral shape metrics *SaRatio* and epsilon ( $\varepsilon$ ) and evaluating their use as possible predictors for  $\eta$ . Similarly to previous investigations, this paper also examines the effect of oscillator period, earthquake magnitude and duration for different levels of damping ratio. Results suggest that *SaRatio* is an effective predictor of  $\eta$ , particularly for highly damped structures. On the other hand, results also indicate that for rock and firm sites, earthquake faulting mechanism and site class do not have a significant

---

<sup>a)</sup> National Research Center for Integrated Natural Disaster Management, CONICYT/FONDAP/15110017, Faculty of Engineering, Pontificia Universidad Católica de Chile, Chile

<sup>b)</sup> John A. Blume Earthquake Engineering Center, Department of Civil and Environmental Engineering, Stanford University, Stanford, CA 94305-4020, U.S.A.

<sup>c)</sup> School of Engineering, Universidad del Desarrollo, Chile

influence on  $\eta$ . A simple period-independent regression model for  $\eta$  as a function of *SaRatio* and damping ratio is proposed. A comparison between median  $\eta$  from this study and those in current Chilean seismic codes shows that code factors are unconservative.

## IV.2 Introduction

Seismic design procedures require an intensity measure (IM), typically a spectral ordinate at a given vibration period  $S_a(T)$ , taken from a pseudo-acceleration design spectrum or a ground motion prediction model (GMPM). In most cases, both approaches consider 5% damped spectral ordinates. However, there are several situations in which one is interested in estimating response spectrum ordinates for damping ratios higher than 5% (for example, in structures with seismic isolation or with energy dissipation devices) or damping ratios smaller than 5% (for instance in high-rise buildings).

When systems with damping ratios different from 5% are under analysis, two approaches are typically considered: (1) using a GMPM specially developed for the desired damping ratio or; (2) scaling 5% damped ordinates by using damping modification factors  $\eta$ . The former approach has a significant limitation as there are only a few GMPMs that have been developed for damping ratios other than 5% and the few that are available have only been developed for specific seismically active regions. Furthermore, probabilistic seismic hazard analysis is typically only available for 5% spectral ordinates. That is why the latter approach is more frequently used, and it is currently implemented in most seismic design codes (e.g., ASCE/SEI 7-16 and NCh2745). This research is focused on damping modification factors  $\eta$ .

Damping modification factor  $\eta$  is defined as the ratio of the peak displacement of a linear SDOF with oscillator period  $T$  and damping ratio  $\xi$  to the peak displacement of a linear SDOF with the same oscillator period  $T$  and damping ratio 5%, as shown in the following expression:

$$\eta(T, \xi) = \frac{S_d(T, \xi)}{S_d(T, \xi = 5\%)} = \frac{A(T, \xi)}{A(T, \xi = 5\%)}$$

where

$$S_d(T, \xi) \equiv |u(t)|_{max}$$

and  $u(t)$  is the displacement of the oscillator under analysis.  $A(T, \xi)$  is the pseudo-acceleration spectral ordinate given by

$$A(T, \xi) \equiv \omega_n^2 S_d(T, \xi)$$

where  $\omega_n$  is the circular frequency of vibration of the system.

The effects of viscous damping on the seismic response of linear SDOF systems have been studied since almost half a century when Newmark and Hall (1982) conducted their pioneer study. Since then, many models have been proposed to estimate  $\eta$  as a function of: (1) oscillator parameters, namely period of vibration  $T$  and damping ratio  $\xi$ ; (2) earthquake magnitude and/or duration and distance to the source; and (3) site class. Lin et al. (2005) compared most relevant models to that date against mean damping modification factors computed with 216 ground motion records from firm sites in California.

Although most authors agree that  $\eta$  depends strongly on oscillator damping ratio and period of vibration, this period-dependence is currently neglected in most seismic design codes. Earthquake duration also affects  $\eta$ . In general, as duration increases, the effect of damping on the peak displacement becomes more pronounced.

Bommer and Mendis (2005) studied several GMPMs developed for damping ratios different from 5% and concluded that  $\eta$  is strongly dependent on earthquake magnitude and source-to-site distance. Cameron and Green (2007) performed a statistical analysis on 1,268 ground motion records finding that oscillator damping ratio and period of vibration, earthquake magnitude, and site class should be considered as predictors for  $\eta$  when the damping ratio is equal or higher than 2%. Also, they included source-to-site distance as a predictor for  $\eta$  when the damping ratio is equal to 1%. Moreover, several authors, including Bommer and Mendis (2005), Lin and Chang (2004), and Daneshvar et al. (2016) concluded that for rock and firm sites, site class does not have a significant influence on damping modification factors.

Stafford et al. (2008) developed a comprehensive study on damping modification factors considering different measures of duration but their recommendations were period independent. Rezaeian et al. (2012) developed a damping modification factor prediction model considering 2,250 horizontal ground motion records with rupture distances smaller than 50 km. They found a significant influence of earthquake duration on  $\eta$ . However, they noted that since earthquake duration is not explicitly considered when defining a seismic design scenario, they included the effect of duration indirectly through the use of magnitude as a predictor in their model given the strong positive correlation between duration and magnitude. Source-to-site distance, damping ratio, and oscillator period were also considered in their study as predictors for  $\eta$ . Bradley (2015) studied how some source-specific and site-specific effects influence the period-dependence of the damping modification factors  $\eta$  using ground motion records in New Zealand.

More recently, Daneshvar et al. (2016) performed a study of damping modification factors using ground motion records associated with the seismic hazard in southwestern British Columbia, Canada. This work differs from previous studies in the sense that it included the earthquake faulting mechanism as a predictor to estimate  $\eta$ . The inclusion of the type of seismic source was motivated by the fact that the seismic hazard in British Columbia includes shallow crustal, deep inslab, and interface subduction earthquakes. They concluded that the earthquake faulting mechanism influences the damping modification factors  $\eta$ .

The main objectives of this research are: (1) to study the influence of magnitude, duration and site class on damping modification factors  $\eta$  computed from ground motions recorded during subduction earthquakes in Chile; (2) to investigate if there are any systematic differences in  $\eta$  computed from ground motions recorded in interplate or intraplate subduction earthquakes; (3) to study the influence of spectral shape on  $\eta$ ; (4) to investigate the performance of two recently-proposed spectral shape proxy parameters as predictors of  $\eta$ ; (5) to propose a simple period-independent model to estimate  $\eta$  as a function of *SaRatio* and damping ratio; and (6) to compare computed median  $\eta$  values to damping modification factors  $B_D$  and  $B_M$  specified in the current Chilean Code NCh2745 for seismic isolation.

### **IV.3 Ground Motion Database**

The ground motion set used in this study consisted of 5,270 ground motion time histories recorded during 1,137 seismic events that occurred in Chile between 1985 and 2015. The seismic database used in this work was provided by the project SIBER-RISK (SIBER-RISK

2019). This database includes 1,004 interface events and 133 intraplate (in slab) events, resulting in 4,126 and 1,144 ground motions records, respectively.

Only events with magnitudes greater or equal than 5.0 were considered. The database includes several large-magnitude interface events that have taken place in Chile in recent years, including the 2010  $M_w$  8.8 Maule, 2014  $M_w$  8.2 Iquique, and 2015  $M_w$  8.4 Illapel earthquakes.

Site classes at the recording stations were classified using ASCE/SEI 7-16 (ASCE 2017) criteria based on the average shear wave velocity in the upper 30 meters of the site profile,  $V_{s30}$ . The database considers 68 records in site class A, 1,122 records in site class B, 3,014 records in site class C, and 1,066 records in site class D.

Figure 1 shows the magnitude versus source-to-site distance distribution (using  $R_{rup}$ , the minimum distance between the site and the rupture plane) for the ground motion set used in this study. The mean magnitude and the mean source-to-site distance in the dataset are 5.8 and 136 km, respectively, and are indicated by a red circle in Figure 1. Recorded peak ground accelerations in the dataset range from 0.01 g to 0.98 g.

While the arbitrary horizontal component approach is frequently used for engineering purposes, other horizontal component definitions as RotDxx or RotIxx (Boore 2010) are preferred when sensor orientation significantly influences the seismic characterization, e.g., ground motion records reflecting directivity effects. In this study, the damping modification factors were calculated for arbitrary horizontal components and RotI50 horizontal components, and results show that, for the Chilean dataset under analysis, the difference between both approaches is negligible, as it can be seen in Figure 4. Based on this fact, this study is developed using the arbitrary component approach.

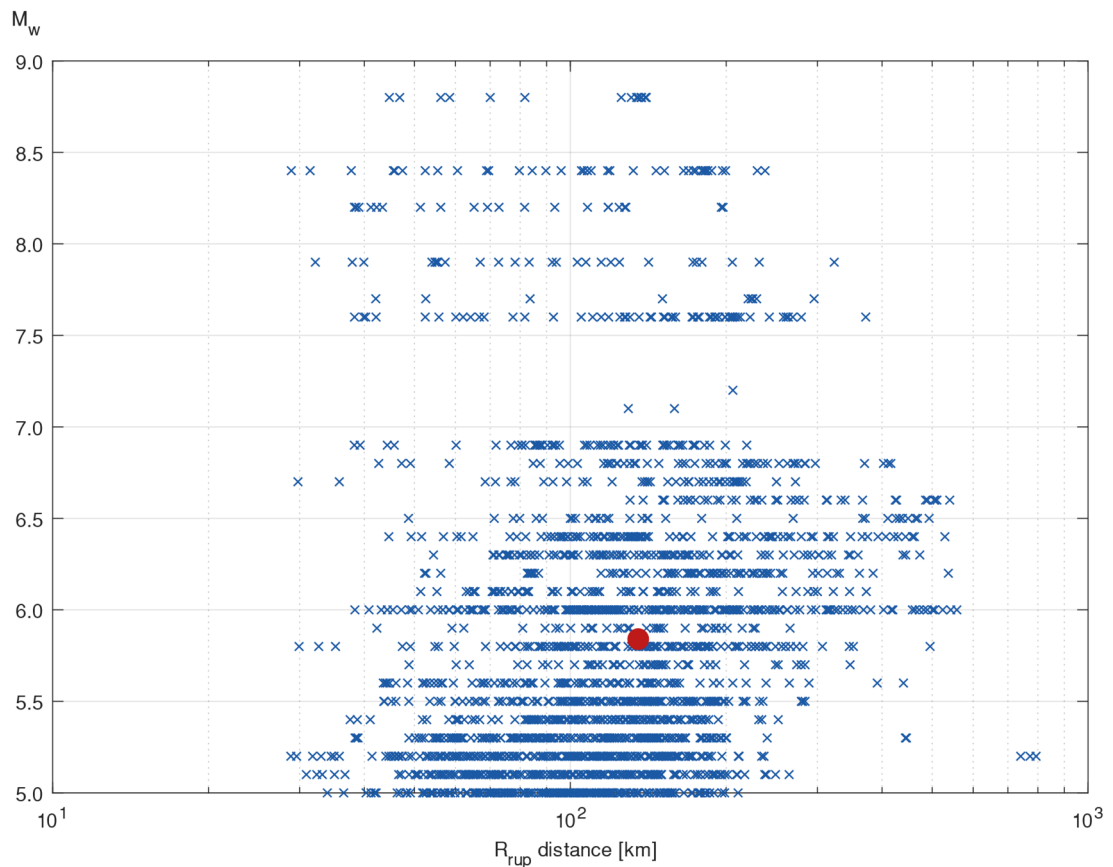


Figure IV-1. Magnitude versus source-to-site distance (minimum distance between source and site,  $R_{rup}$ ) for the considered ground motion database.

For each recorded ground motion, two different significant durations were computed, namely  $D_{5-75}$  and  $D_{5-95}$  (Bommer and Martinez-Pereira 1999). Figure 2 shows that for the ground motions considered in this study, the correlation between duration and moment magnitude is quite similar for both duration parameters with coefficients of determination ( $R^2$ ) of 0.22 for  $D_{5-75}$  and 0.23 for  $D_{5-95}$ , indicating no relevant difference between the use of one or the other. This is consistent with results by Stafford et al. (2008) that concluded that there was no significant difference between both duration measurements when used as a predictor to estimate  $\eta$ . Figure 3 shows the correlation between both duration measures

and source-to-site distance ( $R_{rup}$ ). In this case,  $D_{5-75}$  shows a higher correlation with  $R_{rup}$  than  $D_{5-95}$ , with coefficients of determination ( $R^2$ ) 0.32 and 0.16, respectively.

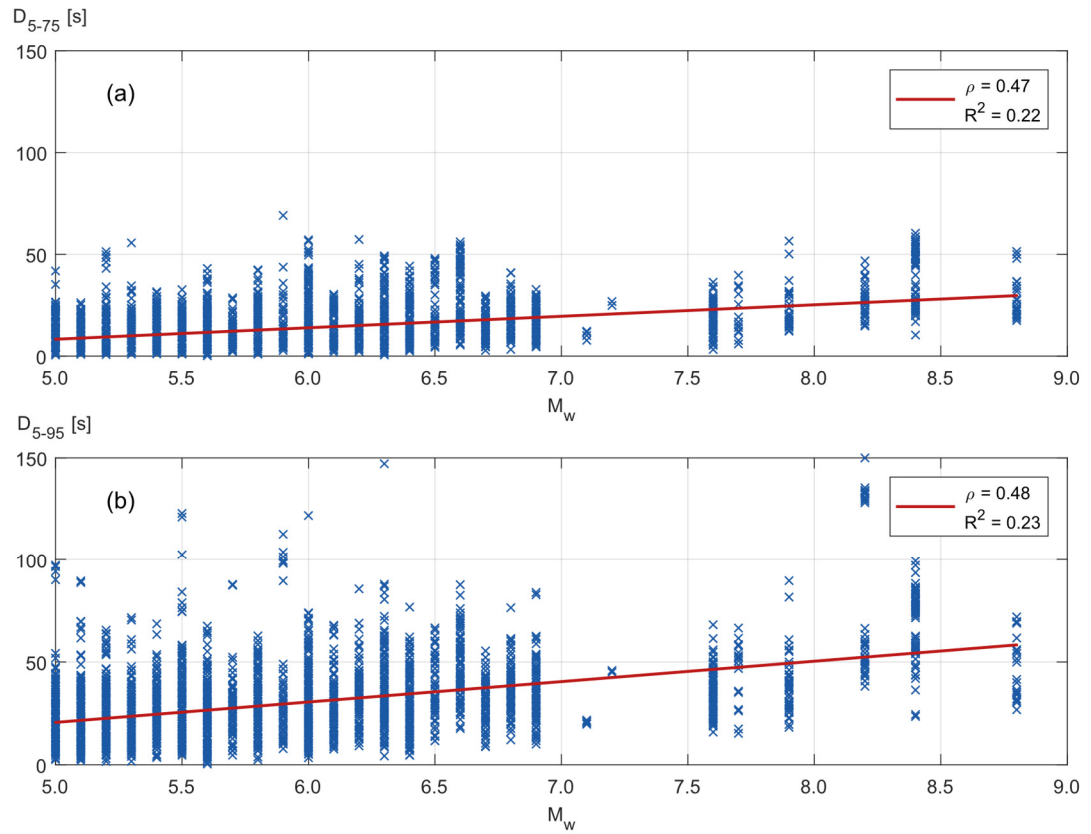


Figure IV-2. Variability of record duration as a function of magnitude; (a)  $D_{5-75}$  versus  $M_w$ , and (b)  $D_{5-95}$  versus  $M_w$ .

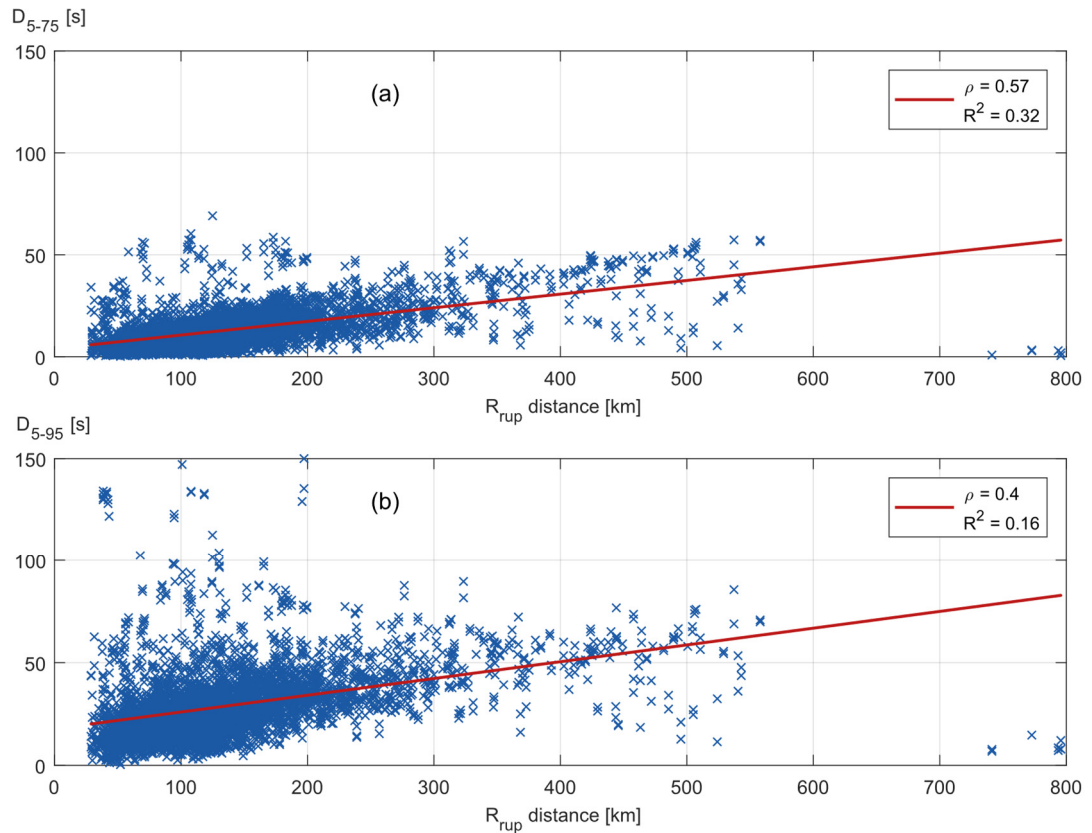


Figure IV-3. Variability of record duration as a function of source-to-site distance (minimum distance between source and site,  $R_{rup}$ ); (a)  $D_{5-75}$  versus  $R_{rup}$ , and (b)  $D_{5-95}$  versus  $R_{rup}$ .

#### IV.4 Damping Modification Factors

To assess the relationship between  $\eta$  and different predictors, damping modification factors were computed using the ground motion database described above for damping ratios of  $\xi = 0.5\%, 1\%, 2\%, 3\%, 4\%, 5\%, 8\%, 10\%, 12\%, 15\%, 18\%, 20\%, 25\%, 30\%$ , and  $50\%$  and a range of oscillator periods between  $0.05$  s and  $6$  s, with a period interval of  $0.01$  s.

Figure 4 shows median  $\eta$  values as a function of oscillator period for the complete ground motion dataset and selected damping ratios  $\xi = 1\%, 2\%, 3\%, 10\%, 20\%$ , and  $30\%$ . Median

values were calculated for arbitrary horizontal components and RotI50 horizontal components, and results are shown in blue solid and red dashed lines, respectively. The shaded area represents the  $\eta$ -values between the 16<sup>th</sup> and 84<sup>th</sup> percentiles, showing that dispersion around the median significantly increases as the damping ratios depart from 5%.

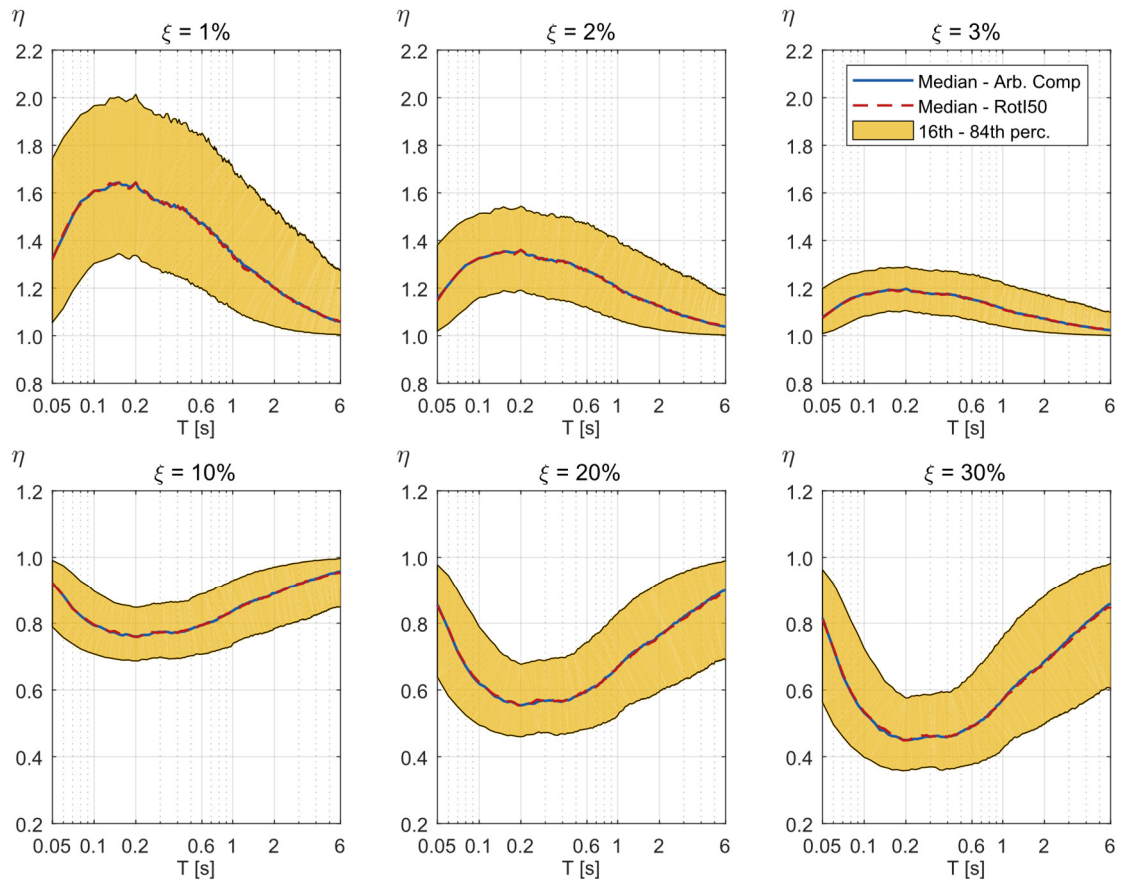


Figure IV-4. Effect of damping ratio and oscillator period on median  $\eta$  values, considering arbitrary horizontal components and RotI50 horizontal components, in blue solid and red dashed lines, respectively. The shaded area represents values between the 16<sup>th</sup> and 84<sup>th</sup> percentiles of  $\eta$ .

As it has been extensively stated in the literature (Bommer and Mendis 2005, Rezaeian et al. 2012) earthquake magnitude and duration have a relevant effect on damping modification factors  $\eta$ . Higher magnitude earthquakes tend to have longer duration, leading to more

significant response reductions in highly damped systems, and more significant response increases in low damping systems. Figure 5 shows the calculated median of  $\eta$  as a function of oscillator period when the ground motion dataset is binned by magnitude. Considered magnitude intervals were [5.0 - 6.0), [6.0 - 7.0), [7.0 - 8.0), and above 8.0, with 3202, 1698, 218, and 152 ground motion records, respectively. To isolate the effect of magnitude and to neutralize any relevant site effect, damping modification factors were normalized to a constant  $V_{s30}$  value of 760 m/s, by implementing the damping modification factor prediction model developed by Akkar et al. (2014) for assessment of the normalizing factor. Median  $\eta$  values calculated without normalization and median  $\eta$  values normalized to  $V_{s30} = 760$  m/s are shown in solid and dashed lines, respectively. It is observed that site correction has a mild influence on median values, especially in oscillators with vibration periods higher than 4.0 seconds and high damping ratio.

Results show a strong influence of earthquake magnitude on  $\eta$ . For example, an oscillator with a vibration period of 3.0 s and 20% damping ratio shows median  $\eta$  values of 0.89 and 0.61, for earthquakes in the [5.0 - 6.0) and the above 8.0 intervals, respectively, indicating an additional reduction in spectral ordinates of 31% in the higher magnitude scenario. Larger jaggedness in the curves corresponding to the two larger magnitudes bins, particularly for damping ratios of 1% and 2%, are the result of the smaller number of ground motions in these bins.

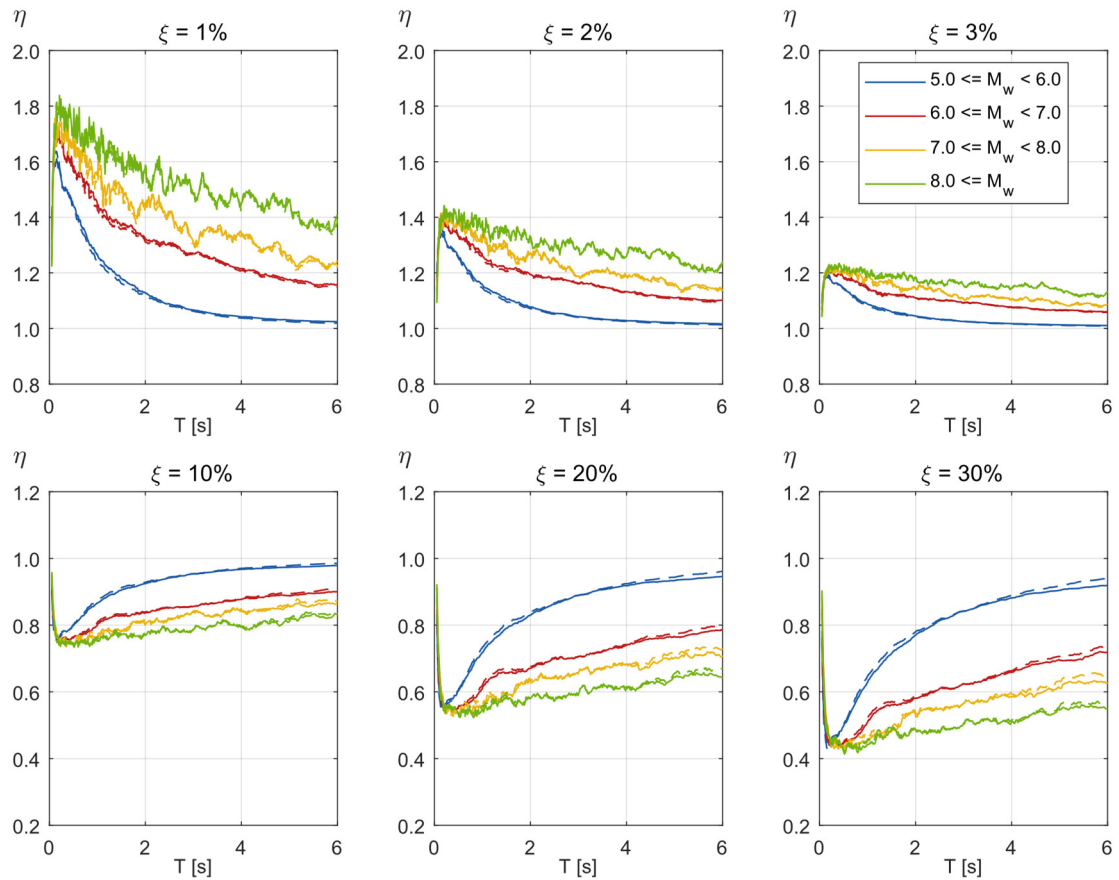


Figure IV-5. Effect of magnitude on median  $\eta$  values, calculated without site effect normalization and calculated with site effect normalization, in solid and dashed lines, respectively.

To investigate if differences in  $\eta$  calculated in this study and those calculated by Lin and Chang (2004) are due to differences in the earthquake faulting mechanism or due to differences in magnitudes, two subsets of the Chilean database were considered by selecting records associated with: (i) events of minimum magnitude 5.7 (to achieve a mean magnitude similar to that in Lin and Chang, 2004); and (ii) events of magnitude 8.0 or above.

Figure 6 compares median damping modification factors  $\eta$  computed in this study (for two subsets with minimum magnitudes of 5.7 and 8.0) with: (i) those currently specified in the Chilean code for seismically isolated structures NCh2745; (ii) those proposed by Lin and

Chang (2004); and (iii) those currently specified in ASCE/SEI 7-16. Results show that median  $\eta$  values from this study, when the 5.7 minimum magnitude subset and damping levels higher than 5% are considered, are much closer to the equation proposed by Lin and Chang (2004) for crustal earthquakes in the United States than to the equations used in the Chilean code NCh2745. On the other hand, results for the 8.0 minimum magnitude subset tend to be more consistent with the trends proposed by Chilean code NCh2745.

Results from Figure 6 also show that damping modification factors specified by the Chilean code NCh2745 (INN 2013) are unconservative in the complete period range when damping ratios higher than 5% are considered. For example, for a hypothetical case of an isolated building with an effective oscillator period of 3.0 s and an effective damping ratio of 20%, the 5% design spectral ordinate is reduced, according to the Chilean code procedure, by a factor of 0.52. However, the median value of  $\eta$  obtained for the 5.7 minimum magnitude ground motion subset is 0.70. In other words, the code is unconservative as the spectral ordinate is reduced 25% more than the median reduction computed from recorded ground motions.

Damping modification factors in the Chilean code were based on a set of records from the 1985 Chile earthquake ( $M_w$  7.9) that were spectrally matched in the frequency domain to the NCh2745 design spectrum. Naeim and Lew (1995) found that frequency-domain spectrally-matched ground motions could include high levels of input energy spread in a wide band of periods, then the  $\eta$  factors obtained from these synthetic records tend to overestimate the reduction in the response. As stated by Hancock et al. (2006) this effect could be minimized by using an improved time-domain spectral matching approach that simultaneously matches

spectra corresponding to different levels of damping. Consequently, it is recommended that new versions of the code define damping modification factors from time-domain spectrally matched records or from real earthquake records, like the ones presented in this study.

It should be noted that expressions in NCh2745 were never intended to be applied for structures with internal damping less than 5%, but if such expressions are used, for example in the design of high rise buildings whose damping ratios in the fundamental period are much smaller than 5%, they will lead to conservative results.

The Chilean code for earthquake-resistant design of industrial structures and facilities, NCh2369 (INN2003), considers a period-independent expression given by  $\eta = (0.05/\xi)^{0.4}$ .

In this case, for the hypothetical case of a system with an effective damping ratio of 20%, a reduction factor of 0.57 is applied resulting also in an unconservative design.

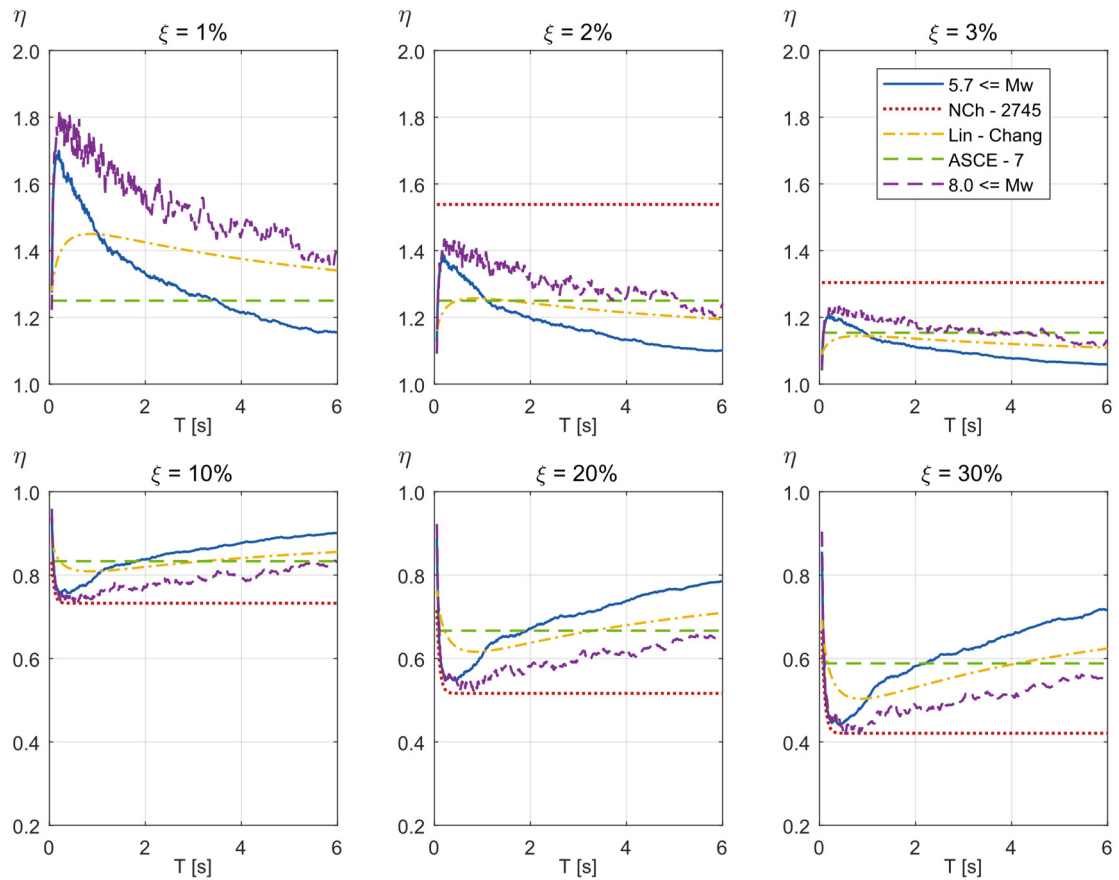


Figure IV-6. Damping modification factors: (i) median values calculated from a sub-set of Chilean ground motions with a minimum magnitude of 5.7; (ii) values currently specified in NCh 2745; (iii) values predicted by Lin and Chang (2004) model; (iv) values currently specified in ASCE/SEI 7-16; and (v) median values calculated from a sub-set of Chilean ground motions with a minimum magnitude of 8.0

Daneshvar et al. (2016) proposed damping modification factors that depend on the earthquake faulting mechanism, as the seismic hazard in British Columbia is affected by shallow crustal, deep in-slab, and interface subduction earthquakes. The authors studied the differences in frequency content in in-slab and interface events, by using their mean period  $T_m$  (Rathje et al. 2004) concluding that in-slab events have, on average, a lower mean period resulting in smaller damping modification factors  $\eta$  for short period structures. However, it

should be noted that, in their study, in addition to changes in the frequency content of ground motions recorded from inslab or interface events, there may be significant differences between their durations and magnitudes, that should also be considered when predicting  $\eta$  factors.

To investigate the effect of seismic source on  $\eta$ , ground motions considered in this study were classified based on their faulting mechanism. Figure 7 shows the distribution of magnitudes and  $D_{5-95}$  durations for interface and inslab records. Interface events present higher magnitudes than their corresponding inslab events with mean magnitudes of 5.9 and 5.6, respectively. This difference in magnitudes in interface and inslab events was found to be statistically significant. This statistically significant difference in magnitudes in interface and inslab events was also found to occur when examining the magnitude of subduction events contained in the NGA-Sub project (Bozorgnia and Stewart 2020). However, for the ground motions in our database the mean  $D_{5-95}$  duration is 29 s for both source cases. Bommer and Mendis (2005) studied the effect of both magnitude and duration on  $\eta$ . They concluded that duration, which is strongly correlated to earthquake magnitude, has a relevant effect on  $\eta$ ; therefore, it is important to evaluate the effect of the faulting mechanism separate from the effect of earthquake magnitude or duration.

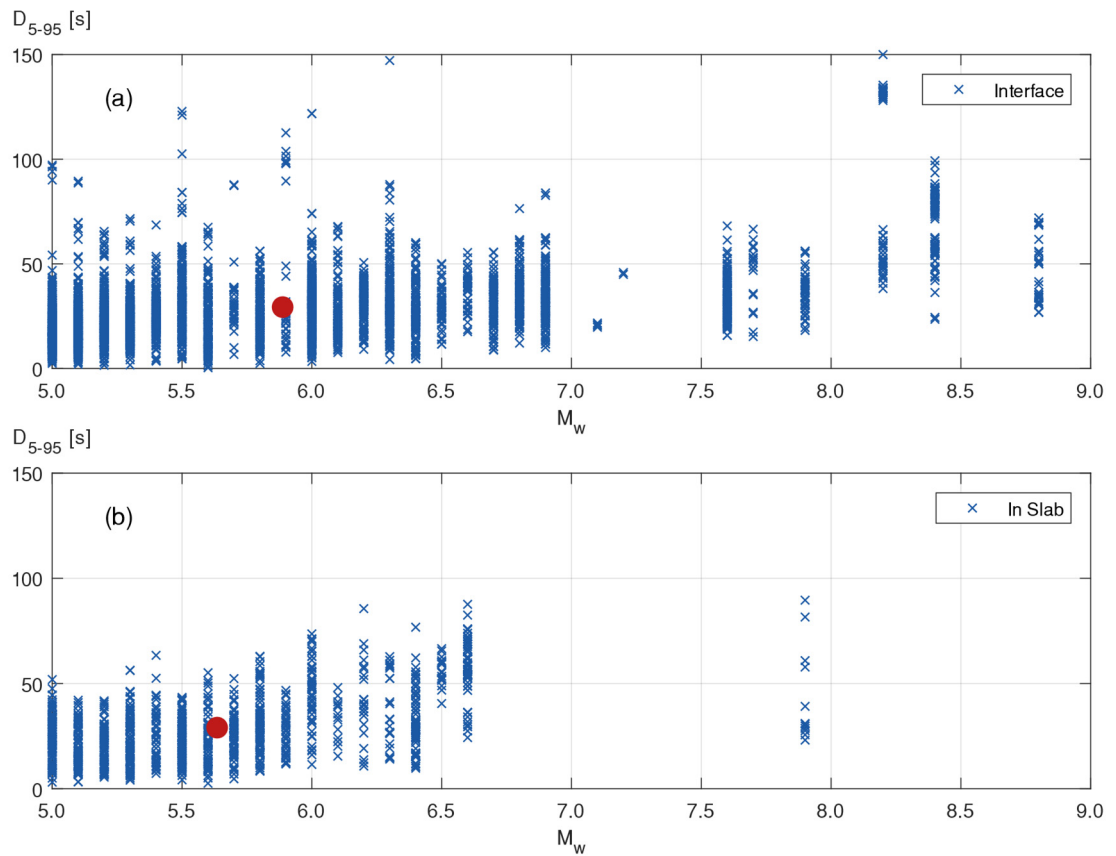


Figure IV-7. Duration  $D_{5-95}$  versus magnitude; (a) interface subduction events, and (b) in-slab events.

To evaluate the effect of faulting mechanism, the median  $\eta$  values for two subsets of interface and in-slab events with the same mean magnitude of 5.42 and the same mean  $D_{5-95}$  duration of 11.3 s are displayed in Figure 8. As shown in this figure, when events with similar magnitudes and durations are compared, there are no systematic differences between the median  $\eta$  values. Variability in  $\eta$  also does not seem to be significantly influenced by the type of source mechanism.

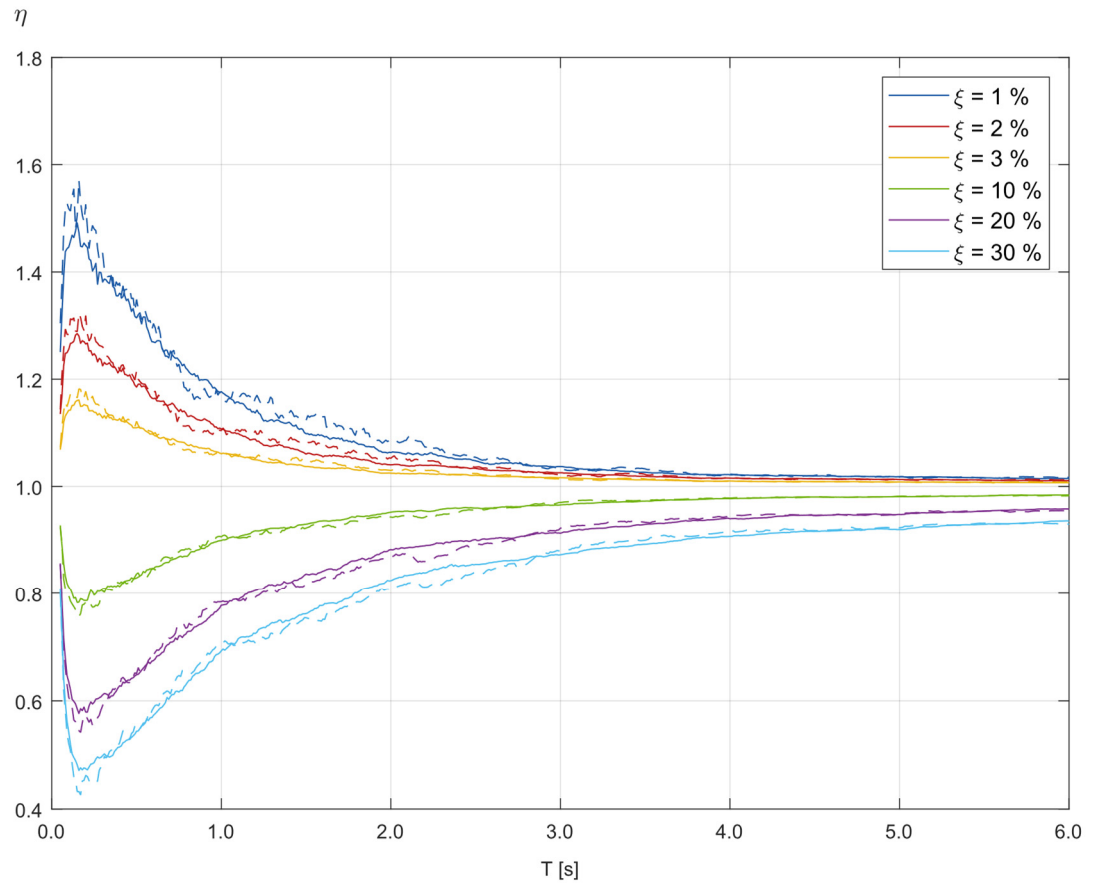


Figure IV-8. Median  $\eta$  values as a function of oscillator period for interface ground motion set and inslab ground motion set, in solid and dashed lines, respectively.

Lin and Chang (2004) performed a study on the site class effect on  $\eta$ . When considering rock and firm soils they concluded that site class produced differences smaller than 5% on mean  $\eta$  values. In this study,  $\eta$  factors were grouped as a function of site conditions at each recording station using the site classes defined in ASCE/SEI 7-16 according to the  $V_{s30}$  parameter. To purely reflect the site class effect, damping modification factors were normalized to: i) a constant magnitude of 5.8, and ii) a rupture distance of 136 km, by implementing the damping modification factor prediction model developed by Akkar et al.

(2014). These normalizing values were selected since they are the mean magnitude and the mean distance for the complete ground motion dataset.

Figure 9 compares median normalized  $\eta$  factors for ground motions recorded at site classes A, B, C, and D. As shown in this figure, site class (for those site classes) does not have a significant effect on median  $\eta$ . There is a greater effect in site class D and higher damping ratios (equal or higher than 20%). The jaggedness shown in the curves corresponding to site class A is due to the significantly smaller number of ground motions recorded in this site class (68) than for the other site classes (1122, 3014, and 1066 for site classes B, C, and D, respectively).

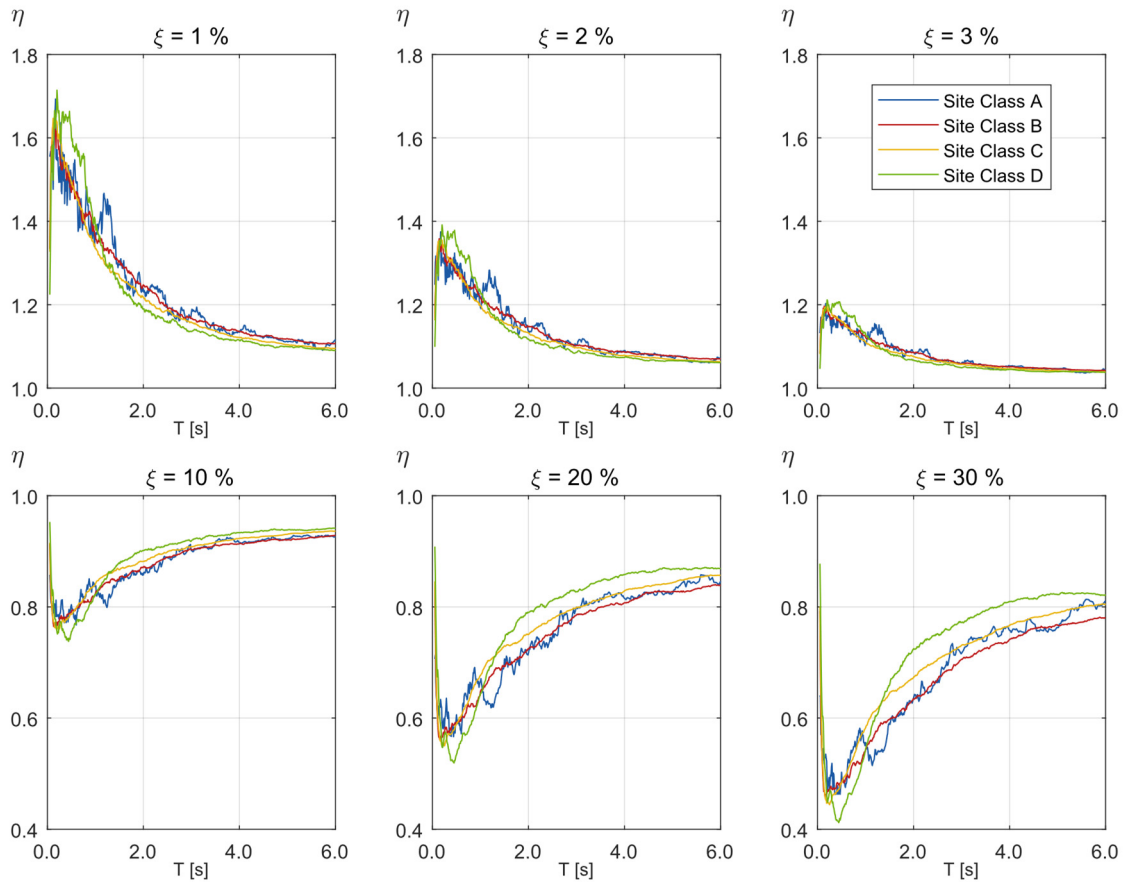


Figure IV-9. Effects of site class (following ASCE/SEI 7-16 classification) on median  $\eta$  values as a function of oscillator period.

#### IV.5 Spectral Shape Metrics

Consistent with previous studies, we found that  $\eta$  factors are primarily dependent on the damping ratio and the period of vibration of the oscillators. However, while most seismic design codes consider the damping ratio dependency, most specify period independent  $\eta$  factors. Another weakness of current design procedures is that earthquake magnitude or duration, are also not explicitly considered in the estimation of  $\eta$ , although their influence

has been widely established in the literature (e.g., Bommer and Mendis 2005, Rezaeian et al. 2012) and also corroborated by the results of this work.

Recent studies have shown that in addition to causal parameters such as earthquake magnitude and source-to-site distance, spectral shape may have an important influence on the seismic response of structures. To study the influence of spectral shape on  $\eta$  factors, two different spectral shape metrics were evaluated as possible predictors when estimating  $\eta$ .

The first approximate measure of spectral shape that was evaluated was epsilon ( $\varepsilon$ ) which is defined as the number of logarithmic standard deviations that a given spectral ordinate is above or below the median value predicted by a GMPM and is evaluated by the following expression:

$$\varepsilon(T) \equiv \frac{\ln Sa(T) - \mu_{LnSA}(M, R, T)_{GMPM}}{\sigma_{LnSA}(T)_{GMPM}}$$

where  $\ln Sa(T)$  is the natural logarithm of the spectral pseudo-acceleration ordinate at a given vibration period  $T$ , and  $\mu_{LnSA}(M, R, T)_{GMPM}$  and  $\sigma_{LnSA}(T)_{GMPM}$  are the values of the mean and the standard deviation of  $\ln Sa(T)$ , respectively, as predicted by a representative GMPM, being all the defined quantities typically calculated for a 5% damping ratio. Epsilon ( $\varepsilon$ ) depends on the GMPM selected for its evaluation, but Baker and Cornell (2006) concluded that its value does not show a strong dependency on the GMPM used in its calculation. Consequently, in this work epsilon ( $\varepsilon$ ) values were calculated using the GMPM developed by Montalva et al. (2017) for the Chilean subduction zone given that the ground motion set used in our statistical study is quite similar to the set used for the development of their GMPM. It should be noted that as Montalva GMPM predicts geomean spectral

ordinates and this study considers arbitrary horizontal components, a correction factor, based on the results presented in Beyer and Bommer (2006), was considered when epsilon ( $\varepsilon$ ) values were calculated.

The second approximate measure of spectral shape is *SaRatio*, whose robustness as collapse predictor was analyzed by Eads et al. (2016). It is defined as the 5% damping ratio spectral ordinate at the oscillator period of interest  $T_1$ , normalized by the geometric mean of the 5% damping ratio spectral ordinates over a period range, defined by two non-negative parameters  $a$  and  $b$ , and is evaluated with the expression:

$$SaRatio = \frac{Sa(T_1, \xi = 5\%)}{Sa_{avg}([a \cdot T_1, b \cdot T_1])}$$

where

$$Sa_{avg}([a \cdot T_1, b \cdot T_1]) = \left( \prod_{i=1}^N Sa(T_i, \xi = 5\%) \right)^{\frac{1}{N}}$$

and

$$T_i = \left( a + \frac{(i-1)}{(N-1)}(b-a) \right) T_1$$

$N$  is the number of ordinates, typically equally spaced, considered in the average. In this study we used 100 equally spaced spectral ordinates.

For instance, Eads et al. (2016) found that for a wide range of buildings, the values of  $a$  and  $b$  that maximize the correlation between *SaRatio* and collapse intensity are 0.2 and 3.0, respectively. An optimal period range needs to be selected to maximize the correlation

between *SaRatio* and  $\eta$  by selecting appropriate values for  $a$  and  $b$  factors. An extensive calculation was implemented herein for this purpose considering SDOF oscillators with vibration periods  $T = 0.25$  s,  $0.50$  s,  $0.75$  s,  $1.00$  s,  $1.25$  s,  $1.50$  s,  $1.75$  s,  $2.00$  s,  $2.25$  s,  $2.50$  s,  $2.75$  s, and  $3.00$  s and damping ratios of  $\xi = 1\%$ ,  $2\%$ ,  $10\%$ , and  $20\%$ , leading to a total of 48 cases. Parameters  $\eta$  and *SaRatio* were calculated for each ground motion record and the quality of a linear regression was evaluated through their coefficient of determination  $R^2$ , which was computed for each pair of  $a$  and  $b$  factors. Indeed, this procedure was repeated for all possible combinations of  $a$  and  $b$ , ranging from  $0.02$  to  $0.98$  and  $1.04$  to  $4.00$ , respectively.

Figure 10 displays contour curves of equal  $R^2$  for each  $a$  and  $b$  pair, considering SDOF systems with vibration periods  $T = 0.50$  s,  $1.50$  s, and  $3.00$  s, and  $2\%$  and  $20\%$  critical damping ratio, showing that the maximum coefficient of determination  $R^2$  between  $\eta$  and *SaRatio* is higher for highly damped systems and reaches a maximum value of  $0.62$  for an oscillator with  $T_n = 3$  s and  $\xi = 20\%$ . On the other hand, systems with low damping, say  $2\%$ , show significantly smaller correlation and reach a maximum  $R^2$  value of  $0.30$  for  $T_n = 3$  s and  $\xi = 2\%$ .

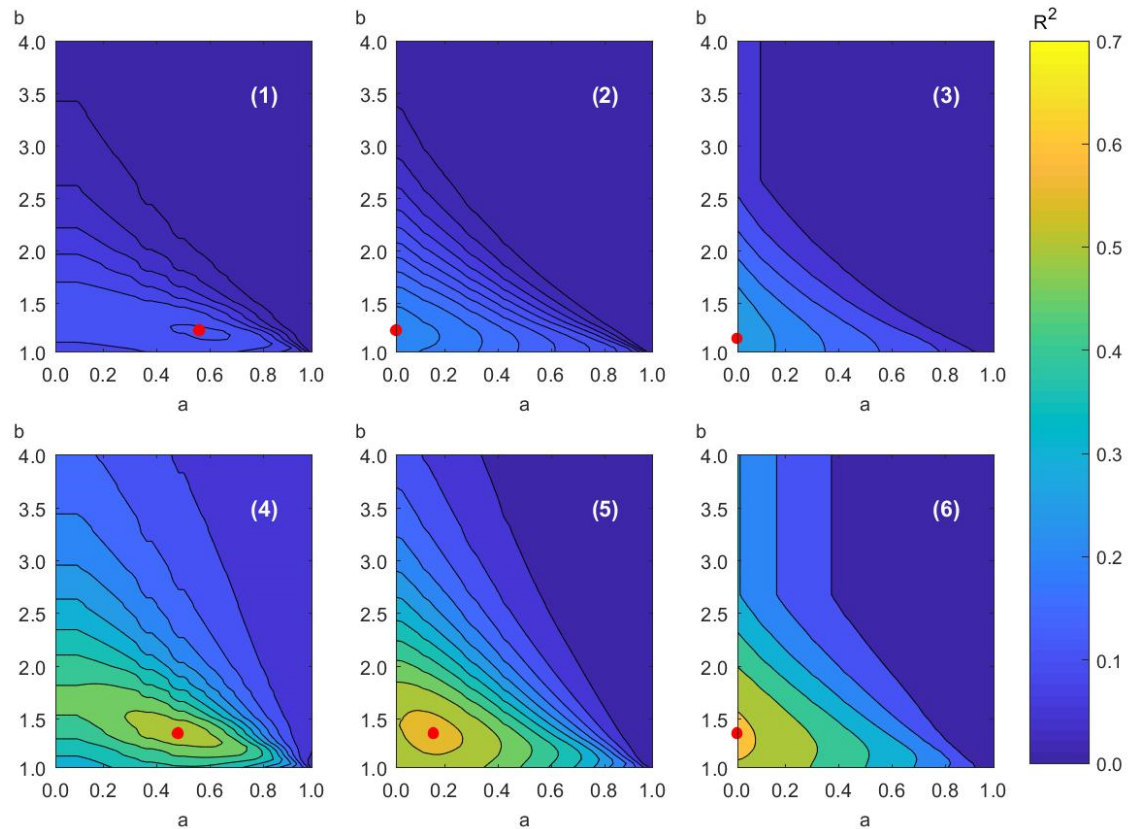


Figure IV-10. Contour curves of equal  $R^2$  for  $\eta$  as a function of  $SaRatio$  for different  $a$  and  $b$  pairs:

- (1)  $T = 0.5$  s and  $\xi = 2\%$ ; (2)  $T = 1.5$  s and  $\xi = 2\%$ ; (3)  $T = 3.0$  s and  $\xi = 2\%$ ; (4)  $T = 0.5$  s and  $\xi = 20\%$ ; (5)  $T = 1.5$  s and  $\xi = 20\%$ ; and (6)  $T = 3.0$  s and  $\xi = 20\%$ .

The optimal  $b$  factor, that is the one that maximizes the coefficient of determination  $R^2$ , varies with the oscillator period and the damping ratio, but it is typically between 1.1 and 1.4. There is, however, a small increment of  $b$  with increasing values of  $\xi$ . On the other hand, optimum values of  $a$  present more variability ranging from 0.02 (i.e., the complete spectral zone to the left of the vibration period of interest) to 0.8. In general, optimum values of  $a$  decrease as the oscillator period increases. This variability is summarized in Figure 11, which shows how optimal values of  $a$  and  $b$  vary as a function of vibration period and damping ratio.

Results of Figure 10 suggest that there is a significant correlation between  $\eta$  and  $SaRatio$ , especially in systems with high damping ratio and long vibration period (e.g., structures with seismic isolation or energy dissipators devices). However, as Figure 11 shows, the optimal values of  $a$  and  $b$  that maximize this correlation are period dependent, thus presenting an additional complexity when using  $SaRatio$  as a predictor.

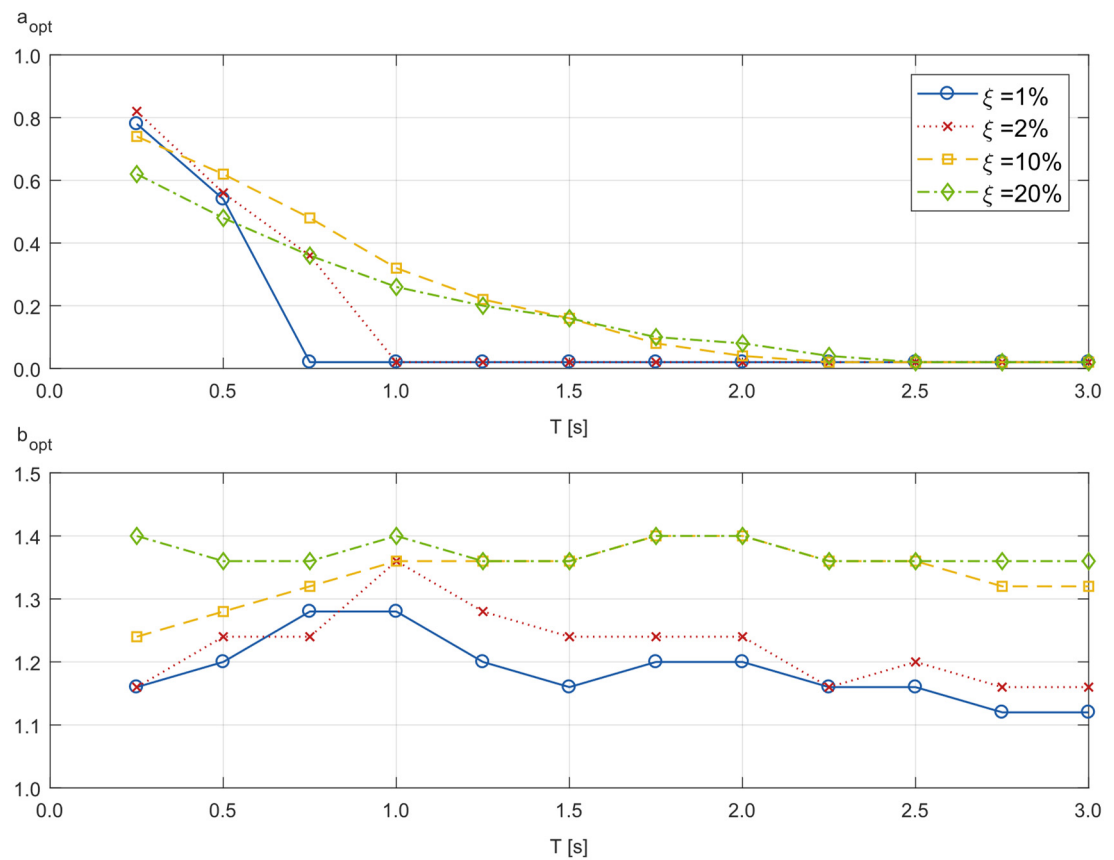


Figure IV-11.  $a$  and  $b$  factor optimal values as a function of vibration period for different damping ratios.

To propose a simplification in the  $SaRatio$  calculation procedure, an interval of  $[0.2 \cdot T_1, 1.3 \cdot T_1]$  independent of vibration period and damping ratio was used to evaluate the correlation between  $\eta$  and  $SaRatio$ . Figure 12 compares the values of  $R^2$  calculated when

using optimal values of  $a$  and  $b$ , depending on the oscillator parameters when computing  $SaRatio$ , and when using  $a$  and  $b$  fixed to 0.2 and 1.3, respectively. As shown in this figure, there is a significant difference between the  $R^2$  values computed using optimal versus constant  $a$  and  $b$  factors for short period oscillators with high-damping ratios. However, in structures with low damping ratios, regardless of vibration period, and in structures with high damping ratios and vibration periods longer than  $T = 1.0$  s the difference is relatively small (less than 10% difference from the optimal  $R^2$  value). Hence, this constant interval appears to provide relatively good results leading to a more straightforward procedure, especially in structures equipped with seismic isolation whose effective periods tend to be long. Therefore, this approach will be used in the remaining sections of this document.

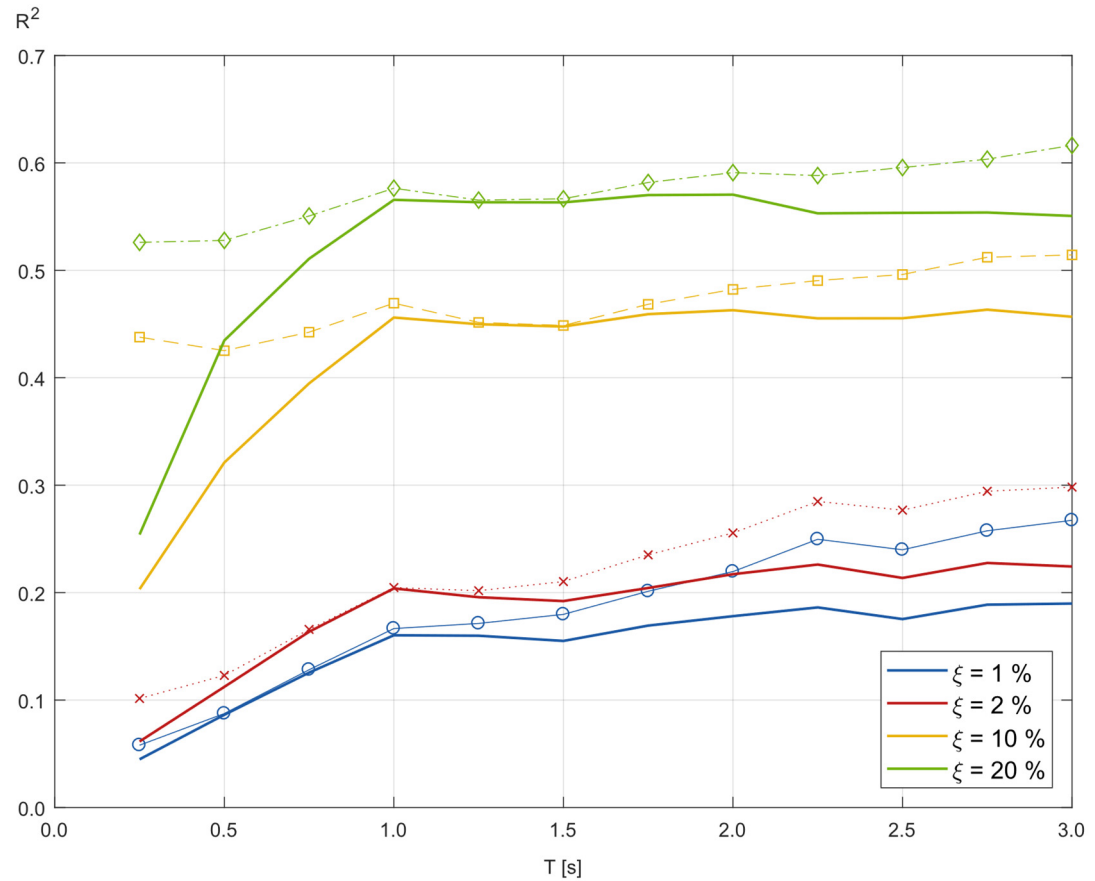


Figure IV-12.  $R^2$  values measuring the correlation between  $\eta$  and  $SaRatio$  as a function of vibration period and damping ratio for two different methodologies to compute  $SaRatio$ : (1) considering optimal values of  $a$  and  $b$  factors; and (2) considering constant values of  $a$  and  $b$  factors, displayed with markers and solid lines, respectively.

#### IV.6 Evaluation Of Possible Predictors

Having already defined the period range for  $SaRatio$  calculation, the capabilities of different parameters were assessed as possible predictors of damping modification factors  $\eta$ . Figure 13 shows scatter plots of  $\eta$ , calculated for an SDOF oscillator with  $T = 3.0$  s and  $\xi = 20\%$ , as a function of magnitude, significant duration  $D_{5-95}$ , epsilon ( $\varepsilon$ ), and  $SaRatio$  for the

complete dataset of ground motion records. It should be explicitly stated here that spectral shape metrics epsilon ( $\varepsilon$ ) and *SaRatio* were calculated considering 5% damping ratio, as their capabilities as spectral shape proxies are not strongly dependent on the damping ratio considered in their calculation.

A regression curve (linear or exponential, the one that fits best) is drawn through the data. As shown in Figure 13, *SaRatio* performs significantly better as a predictor than the other three parameters showing a coefficient of determination  $R^2$  of 0.56 with an exponential model, followed by earthquake magnitude with an  $R^2$  value of 0.33, duration  $D_{5-95}$  with an  $R^2$  value of 0.15, and finally epsilon showing practically no correlation with  $\eta$ . The same conclusion can be drawn when the Akaike information criterion (AIC) was implemented to compare the relative quality of the models. Due to space limitations, only results for this oscillator period and damping ratio are shown, but this trend was observed in all the oscillators with damping ratios higher than 10%. In the electronic supplement of this manuscript, plots for different periods of vibration and damping ratios are included.

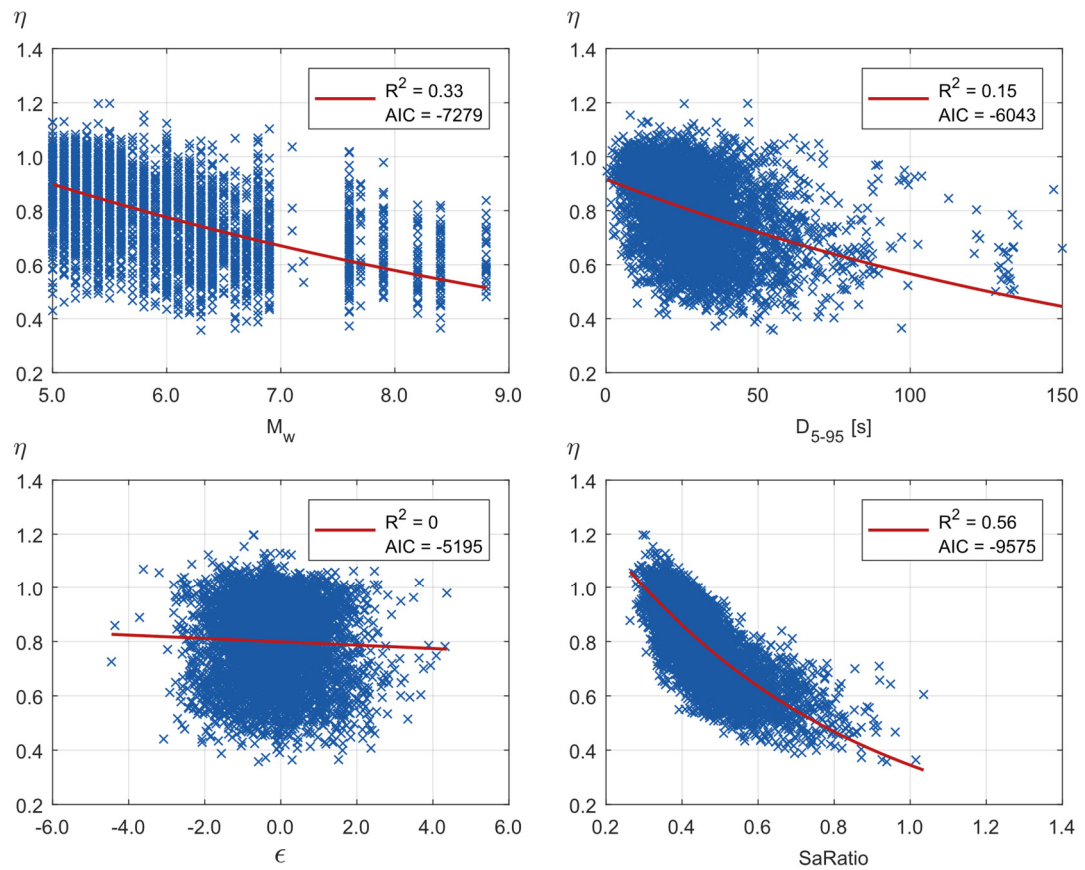


Figure IV-13.  $\eta$  values as a function of earthquake magnitude, duration  $D_{5-95}$ , epsilon ( $\epsilon$ ), and SaRatio for the complete ground motion set and an SDOF oscillator with  $T=3.0$  s and  $\xi = 20\%$ .

Coefficients of determination  $R^2$  for regression of  $\eta$  as a function of SaRatio are presented for different vibration periods and damping ratios in the first subplot of Figure 14.  $R^2$  values higher than 0.4 are obtained for SDOF systems with vibration periods longer than 0.5 s and damping ratios higher than 10%; this correlation metric increases rapidly as the damping ratio increases. For example, an SDOF with  $T = 1.0$  s and  $\xi = 50\%$  has a coefficient of determination of 0.72, indicating that most of the record-to-record variation in damping modification factors  $\eta$  is due to changes in SaRatio. As shown in the figure, for systems

with damping ratios lower than 10% correlation decreases rapidly regardless of the oscillator period considered.

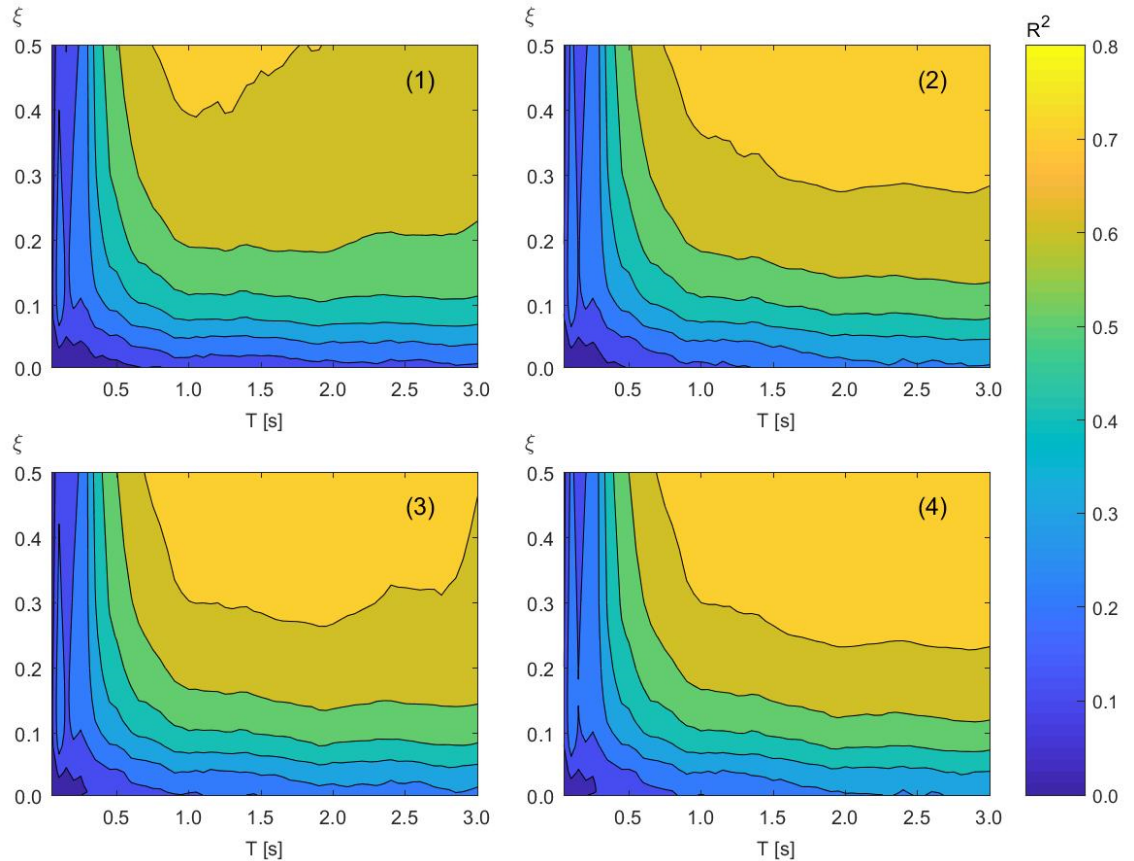


Figure IV-14. Contour curves of equal  $R^2$  for different combinations of oscillator periods and damping ratios when using different predictors: a) SaRatio; b) SaRatio and earthquake magnitude; c) SaRatio and duration  $D_{5-95}$ ; and d) SaRatio, earthquake magnitude, and duration  $D_{5-95}$ .

To evaluate if this exponential model could be improved by including more than one predictor, the following functional forms were also evaluated:

$$\eta = a_1 \cdot \exp(b_1 \cdot SaRatio + c_1 \cdot M_w)$$

$$\eta = a_2 \cdot \exp(b_2 \cdot SaRatio + c_2 \cdot D_{5-95})$$

$$\eta = a_3 \cdot \exp(b_3 \cdot SaRatio + c_3 \cdot M_w + d_3 \cdot D_{5-95})$$

where  $a_i$ ,  $b_i$ ,  $c_i$  and  $d_i$  are constants obtained through nonlinear regression to minimize differences between the observed and estimated values of  $\eta$ .

Contour plots for these models are also displayed in Figure 14 on plots b), c), and d), respectively. A mild improvement is observed, when including additional predictors in addition to *SaRatio*, especially for long period oscillators and damping ratios higher than 30%. Figure 15 presents coefficients of determination  $R^2$  for the four models considered in this study (based on *SaRatio* and additional predictors  $M_w$  and  $D_{5-95}$ ) and those of: (1) a model with source-to-site distance  $R_{rup}$  as the only predictor; (2) a model with earthquake magnitude  $M_w$  as the only predictor; and (3) a model with earthquake magnitude  $M_w$  and source-to-site distance  $R_{rup}$  as predictors. The comparison was performed at damping ratios of 2%, 10%, and 20%, and a range of periods of vibration between  $T = 0.05$  s and 3.00 s. Since the correlation level is relatively low for periods of vibration less than  $T = 1.0$  s and a damping ratio of 2%, there are no significant differences between the different models in this period range. However, as the oscillator period and the damping ratio increase, models using only *SaRatio* or *SaRatio* combined with additional parameters as predictors, significantly improve their  $R^2$ . Even though additional improvement can be achieved by using more complex models, herein only the model predicting  $\eta$  as a function of *SaRatio* (in addition to  $T$  and  $\xi$ ) will be further pursued.

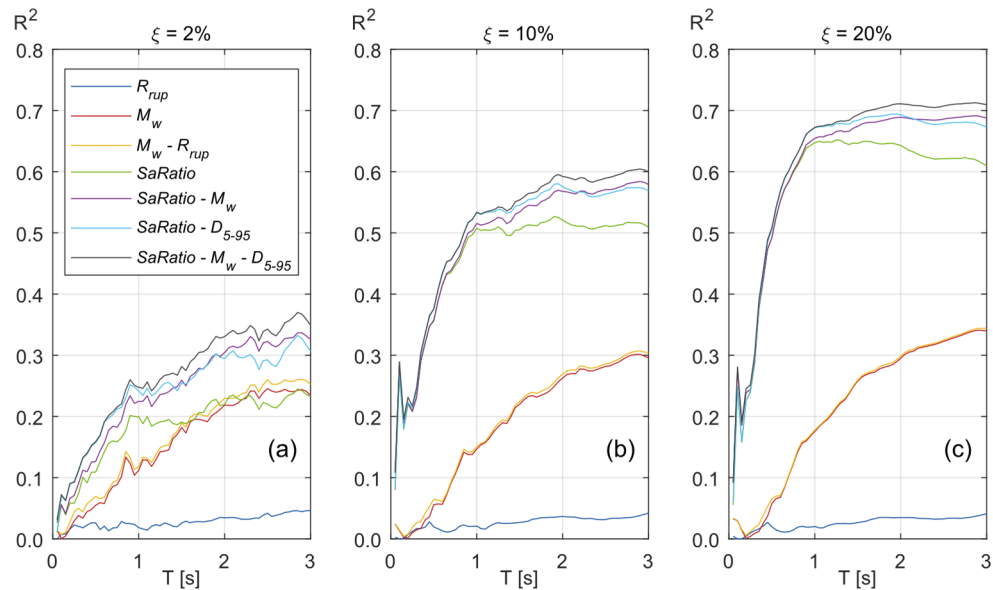


Figure IV-15. Coefficient of determination  $R^2$  as a function of oscillator period for different regression models: a) 2% damping ratio; b) 10% damping ratio; and c) 20% damping ratio.

Figure 16 shows another relevant benefit of using *SaRatio* as a predictor for the damping modification factor  $\eta$ . Median  $\eta$  values as a function of *SaRatio* are plotted for the binned by magnitude ground motion dataset, using the same magnitude intervals of Figure 5, for damping levels  $\xi = 1\%, 2\%, 3\%, 10\%, 20\%$ , and  $30\%$ . For systems with damping levels higher than  $2\%$ , the  $\eta$  versus *SaRatio* relationship shows considerably less dependency on earthquake magnitudes than the  $\eta$  versus period of vibration relationship. Based on this fact, regression-based prediction expressions for  $\eta$  are considerably simpler and more robust if *SaRatio* is used as a predictor, as their regression parameters will not depend on the magnitude range used for the statistical analysis. This means that most of the influence of magnitude on  $\eta$  is computed by considering *SaRatio* as a predictor.

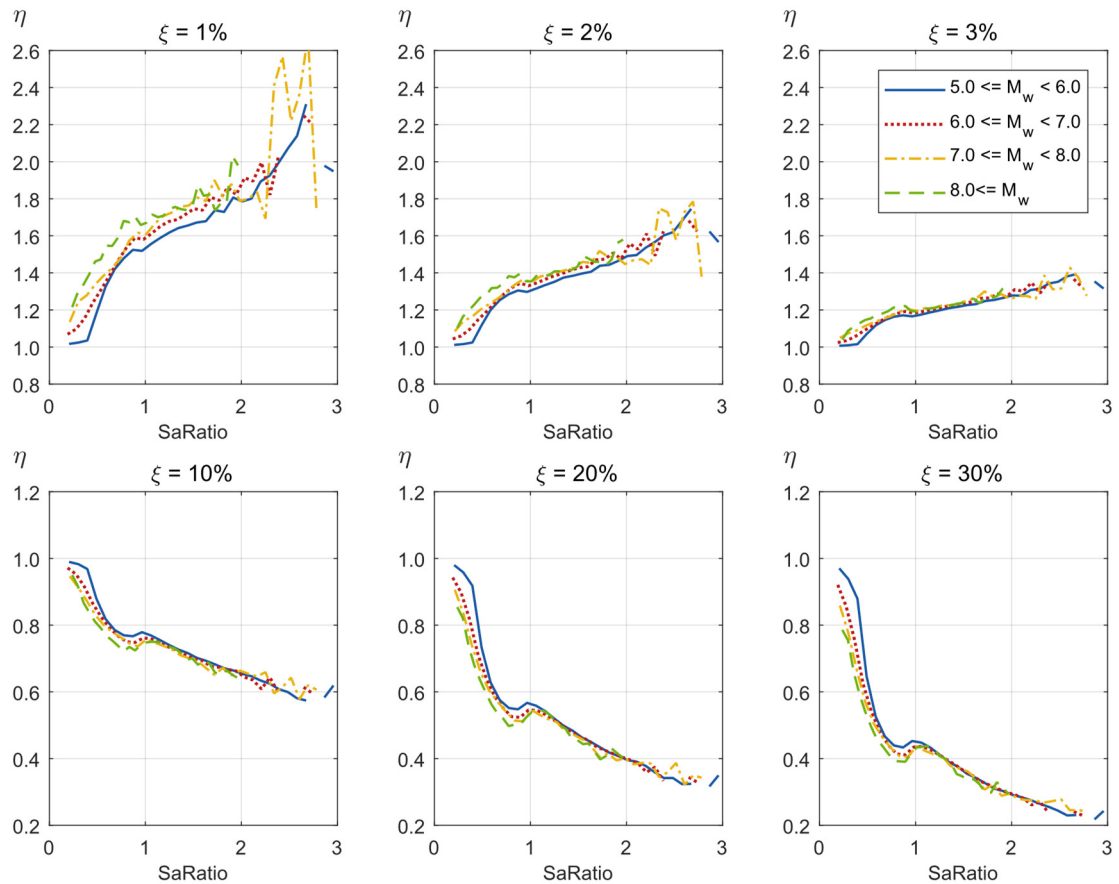


Figure IV-16. Median  $\eta$  values as a function of  $SaRatio$  for magnitude-binned ground motion records.

#### IV.7 Regression Model

Damping modification factor  $\eta$  is dependent on damping ratio and oscillator period, as it has been extensively documented in the literature and confirmed by results from this study. On the other hand, earthquake duration and/or event magnitude, are also known to influence  $\eta$ . However, based on the results of this study, their correlations are not as strong as the one with  $SaRatio$ , especially for systems with high damping. Additionally, as it can be seen in

Figure 16, the  $\eta$  versus  $SaRatio$  relationship presents only a minor magnitude dependency for the complete  $SaRatio$  range and damping ratios above 2%.

Figure 17 shows scatter plots of  $\eta$  as a function of  $SaRatio$ , for systems with 10% and 20% critical damping and vibration periods  $T = 0.5$  s, 1.5 s, and 3.0 s. As it can be seen in this figure, the relationship between  $\eta$  and  $SaRatio$  is not strongly influenced by the oscillator period for which  $SaRatio$  is calculated. As the oscillator period shortens, the maximum value of  $SaRatio$  increases; however, the exponential trend between these two variables is similar, regardless of the oscillator period under consideration. Based on this fact, the variation of  $\eta$  as a function of  $SaRatio$  could be treated approximately as period independent, and a simplified model for evaluating  $\eta$  only as a function of  $SaRatio$  and  $\xi$  can be proposed.

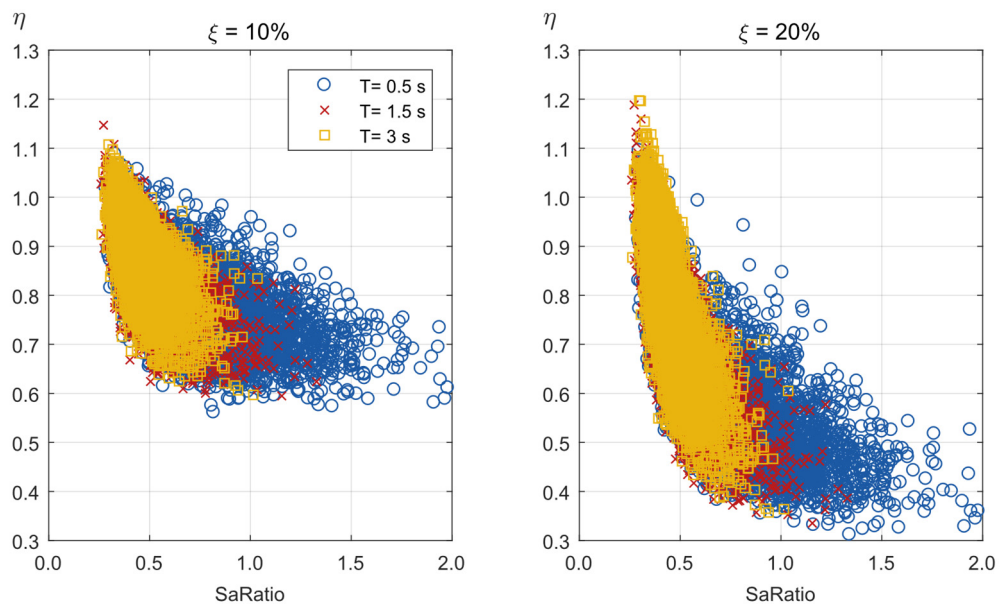


Figure IV-17.  $\eta$  versus  $SaRatio$  scattered data for different oscillator periods.

Figure 18 shows a tridimensional scatter plot of the three variables under study. On the horizontal plane, the axes are  $\xi$  and  $SaRatio$ , and the vertical axis is  $\eta$ .  $SaRatio$  and  $\eta$  values

were calculated for six vibration periods  $T = 0.5$  s, 1.0 s, 1.5 s, 2.0 s, 2.5 s, and 3.0 s for the complete ground motion set, resulting in a total of 31,620 points for each damping ratio. As the calculation was repeated for damping ratios of  $\xi = 10\%$ , 12%, 15%, 18%, 20%, and 25%, the total number of  $(\xi, SaRatio, \eta)$  samples increases to 189,720

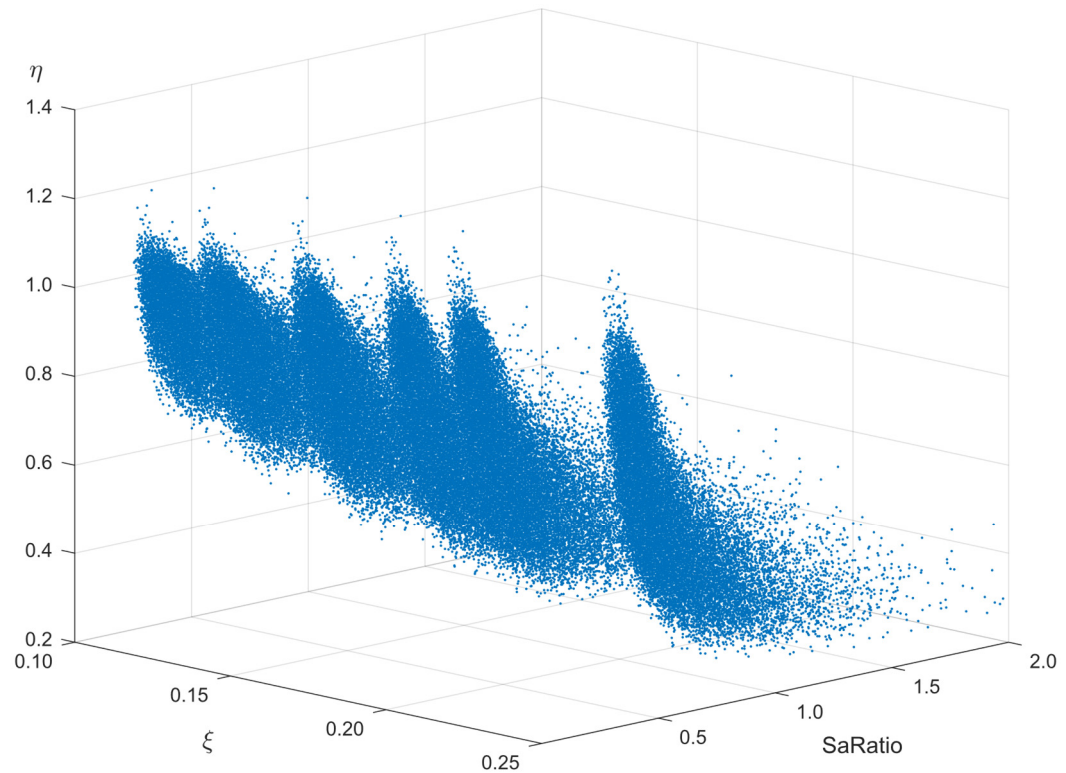


Figure IV-18. 189,720  $(\xi, SaRatio, \eta)$  sample points to perform non-linear regression.

Several functional forms were studied to propose a sufficiently simple, but reasonably accurate, model. A functional form composed by the addition of two exponential terms is finally proposed:

$$\eta(\xi, SaRatio) = \exp(a_1 \cdot \xi) + \exp(a_2 \cdot SaRatio)$$

where coefficients  $a_1$  and  $a_2$  were determined through a nonlinear least square regression.

After performing the regression, the calculated values were  $a_1 = -3.66$  and  $a_2 = -3.22$ . The proposed model is intended to be used with damping ratios between 0.10 and 0.25 and *SaRatio* values ranging from 0.40 to 1.60. The corresponding coefficient of determination  $R^2$  over these ranges of *SaRatio* and damping ratios is 0.56. Figures 19 and 20 show a surface fitted through regression and plots of residual, respectively. Residuals are plotted as a function of *SaRatio* for different damping ratios.

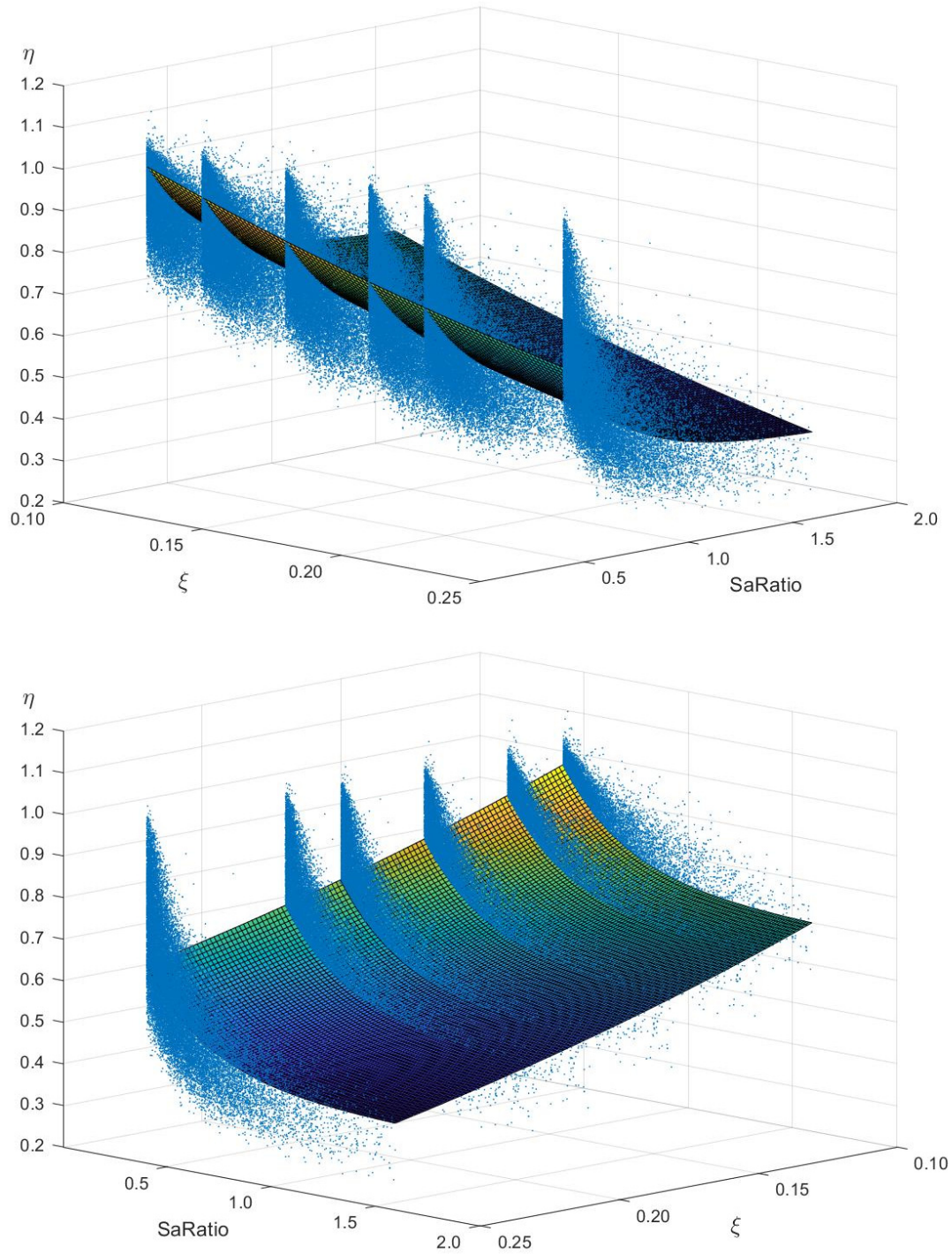


Figure IV-19. Proposed model to estimate  $\eta$  as a function of damping ratio  $\xi$  and *SaRatio* (same data, different views).

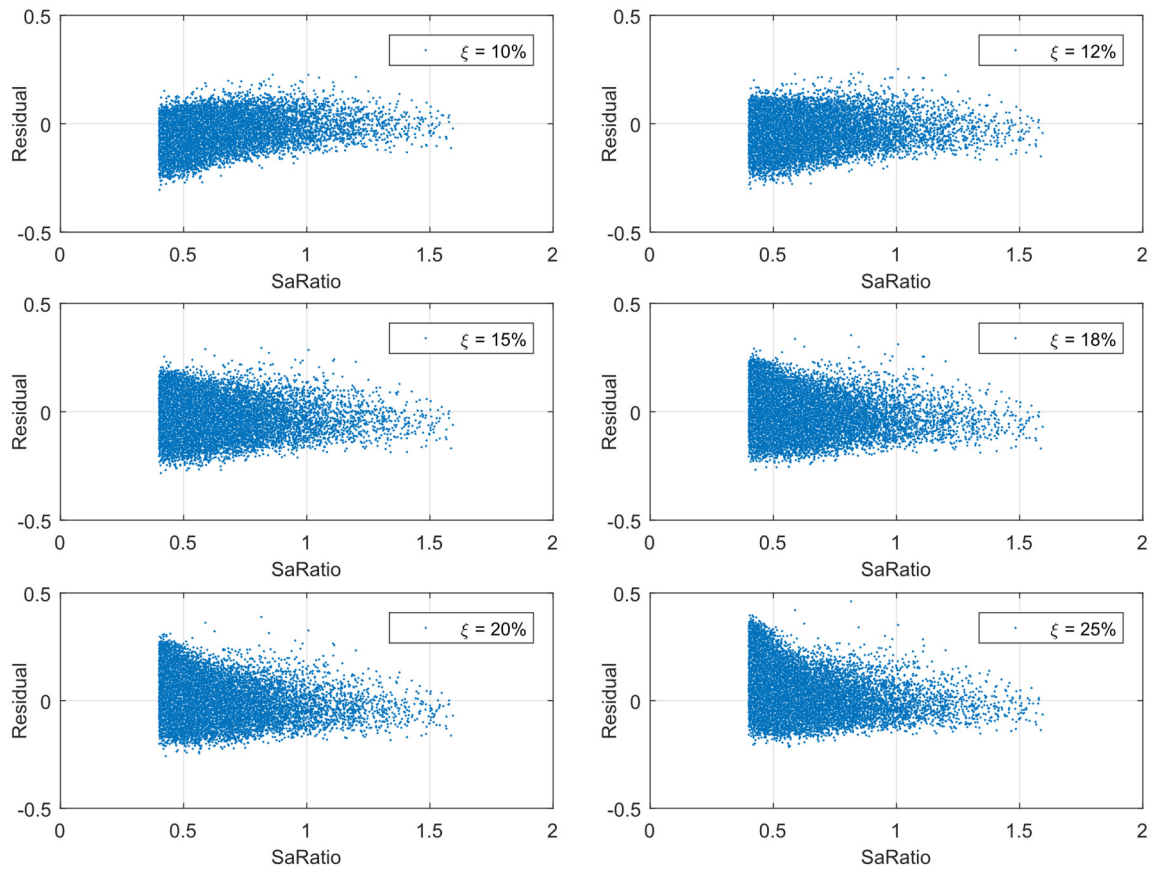


Figure IV-20. Residuals between observed and estimated damping modification factors  $\eta$  as a function of  $\beta$  and SaRatio.

## IV.8 Summary And Conclusions

This study has presented a statistical analysis of damping modification factors  $\eta$  that permit to estimate spectral ordinates corresponding to any value of damping ratio as a function of 5% spectral ordinates. Damping modification factors were computed for a recently compiled Chilean ground motion dataset that includes 5,270 ground motions recorded during 1,137 seismic events. Displacement modification factors were computed for oscillators with periods of vibration ranging from  $T = 0.05$  s to  $T = 6.0$  s, and damping ratios ranging from

0.5% to 50%. These displacement modification factors were calculated considering arbitrary horizontal components and RotI50 horizontal components, being the difference between these two calculation approaches negligible. Results from statistical analysis are generally consistent with widely used regression models from previous studies when the same magnitude bounds are considered.

The novelty in this study is the evaluation of the effect of spectral shape on  $\eta$ , using two recently-proposed spectral shape proxy parameters as epsilon ( $\epsilon$ ) and *SaRatio*. A detailed analysis is presented to determine the optimal period range to be used for *SaRatio* calculation. Although strictly speaking optimal period range is period and damping dependent, reasonable results are obtained when a constant period range of  $[0.2 \cdot T_1, 1.3 \cdot T_1]$  is used for calculating *SaRatio* to estimate the peak displacement response of systems with damping ratio different than 5%.

Results show that *SaRatio* is a better predictor than earthquake magnitude or than duration, especially in moderate and long-period systems, and in highly damped structures. On the other hand, epsilon ( $\epsilon$ ) does not show any significant statistical correlation with  $\eta$ .

In highly damped structures, the  $\eta$  versus *SaRatio* relationship was proven to be only mildly dependent on oscillator period and earthquake magnitude. Therefore, based on this interesting observation, a straightforward regression model is proposed, which enables to estimate  $\eta$  only based on two predictors: damping ratio and *SaRatio*.

Earthquake faulting mechanism was found not to have a significant influence on  $\eta$  when events with similar magnitudes and durations are compared. The effect of soil class was also

studied, and its influence on  $\eta$  variability was also found to be negligible for site classes A, B C, and D.

A comparison between median  $\eta$  values from this statistical analysis and currently implemented  $B_D$  or  $B_M$  demand reduction values in Chilean code NCh 2745 was performed. Results show that  $\eta$  factors are strongly dependent on earthquake magnitude, an aspect that is currently neglected and could be introduced in future versions of the code. Larger magnitude earthquakes tend to show reductions that are, on average, 16% smaller than the reductions prescribed by the code, while smaller magnitude earthquakes lead to reductions significantly smaller than the ones predicted by the code.

### **Acknowledgments**

This research was funded by CONICYT Doctorado Nacional 21161027, the National Research Center for Integrated Natural Disaster Management CONICYT /FONDAP/15110017, and CONICYT/FONDECYT/1170836. We also thank the John A. Blume Earthquake Engineering Center at Stanford University. The seismic database used in this work was provided by the project SIBER-RISK: Simulation Based Earthquake Risk and Resilience of Interdependent Systems and Networks CONICYT/FONDECYT/1170836.

### **Electronic supplement**

Additional figures showing comparisons between various  $\eta$  predictors for different oscillator periods and damping ratios are available in the electronic supplement of this manuscript.

## References

- Akkar, S., Sandikkaya, M. A., and Ay, B. Ö., 2014. Compatible ground-motion prediction equations for damping scaling factors and vertical-to-horizontal spectral amplitude ratios for the broader Europe region. *Bulletin of earthquake engineering*, 12(1), 517-547.
- American Society of Civil Engineers (ASCE), 2017. *Minimum Design Loads for Buildings and Other Structures*, ASCE/SEI 7-16, Reston, VA.
- Baker, J.W., and Allin Cornell, C., 2006. Spectral shape, epsilon and record selection. *Earthquake Engineering & Structural Dynamics*, 35(9), 1077-1095.
- Beyer, K., and Bommer, J. J., 2006. Relationships between median values and between aleatory variabilities for different definitions of the horizontal component of motion. *Bulletin of the Seismological Society of America*, 96(4A), 1512-1522.
- Bommer, J.J., and Martinez-Pereira, A., 1999. The effective duration of earthquake strong motion. *Journal of earthquake engineering*, 3(02), 127-172.
- Bommer, J.J., and Mendis, R., 2005. Scaling of spectral displacement ordinates with damping ratios, *Earthquake Engineering & Structural Dynamics*, 34(2), 145-165.
- Boore, D. M., 2010. Orientation-independent, nongeometric-mean measures of seismic intensity from two horizontal components of motion. *Bulletin of the Seismological Society of America*, 100(4), 1830-1835.
- Bozorgnia, Y., and Stewart, J.P. (Ed.), 2020. *Data Resources for NGA-Subduction Project*, PEER Report 2020/02. Pacific Earthquake Engineering Research Center, Berkeley, CA, 179pp.
- Bradley, B.A., 2015. Period dependence of response spectrum damping modification factors due to source-and site-specific effects, *Earthquake Spectra*, 31(2), 745-759.
- Cameron, W.I., and Green, R.A., 2007. Damping correction factors for horizontal ground-motion response spectra, *Bulletin of the Seismological Society of America*, 97(3), 934-960

- Daneshvar, P., Bouaanani, N., Goda, K., and Atkinson, G.M., 2016. Damping reduction factors for crustal, inslab, and interface earthquakes characterizing seismic hazard in southwestern British Columbia, Canada. *Earthquake Spectra*, 32(1), 45-74.
- Eads, L., Miranda, E. and Lignos, D., 2016. Spectral shape metrics and structural collapse potential, *Earthquake Engineering & Structural Dynamics*, 45(10), 1643-1659.
- Hancock, J., Watson-Lamprey, J., Abrahamson, N. A., Bommer, J. J., Markatis, A., McCoy, E. M. M. A., & Mendis, R., 2006. An improved method of matching response spectra of recorded earthquake ground motion using wavelets. *Journal of earthquake engineering*, 10(spec01), 67-89.
- Instituto Nacional de Normalización (INN), 2003. *Norma Chilena NCh2369 Oficial2003 Diseño sísmico de estructuras e instalaciones industriales*, Chile (in Spanish).
- Instituto Nacional de Normalización (INN), 2013. *Norma Chilena NCh2745 Oficial2013 Análisis y Diseño de Edificios con Aislación Sísmica*, Chile (in Spanish).
- Lin, Y.Y., and Chang, K.C., 2004. Effects of site classes on damping reduction factors, *Journal of Structural Engineering*, 130(11), 1667-1675.
- Lin, Y.Y., Miranda, E., and Chang, K.C., 2005. Evaluation of damping reduction factors for estimating elastic response of structures with high damping, *Earthquake engineering & structural dynamics*, 34(11), 1427-1443.
- Montalva, G. A., Bastías, N., & Rodriguez-Marek, A., 2017. Ground-motion prediction equation for the Chilean subduction zone. *Bulletin of the Seismological Society of America*, 107(2), 901-911.
- Naeim, F., & Lew, M., 1995. On the use of design spectrum compatible time histories. *Earthquake Spectra*, 11(1), 111-127.
- Newmark, N. M., and Hall, W. J., 1982. *Earthquake Spectra and Design*, Earthquake Engineering Research Institute, Oakland, CA.

Rathje, E. M., Faraj, F., Russell, S., and Bray, J. D., 2004. Empirical relationships for frequency content parameters of earthquake ground motions, *Earthquake Spectra*, 20, 119-144.

Rezaeian, S., Bozorgnia, Y., Idriss, I.M., Campbell, K.W., Abrahamson, N., and Silva, W.J., 2012. *Spectral Damping Scaling Factors for Shallow Crustal Earthquakes in Active Tectonic Regions*, PEER Report 2012/01. Pacific Earthquake Engineering Research Center, Berkeley, CA, 168pp.

Simulation Based Earthquake Risk and Resilience of Interdependent Systems and Networks (SIBER-RISK), 2019. Web page for SIBER-RISK: Simulation Based Earthquake Risk and Resilience of Interdependent Systems and Networks CONICYT/FONDECYT/1170836 Strong Motion Database, available at <https://siberrisk.ing.puc.cl/StrongMotionDatabase> (last accessed October 30, 2019)

Stafford, P.J., Mendis, R. and Bommer, J.J., 2008. Dependence of damping correction factors for response spectra on duration and numbers of cycles, *Journal of Structural Engineering*, 134(8), 1364-1373.

## V. SUMMARY AND CONCLUSIONS

This dissertation presents an investigation of several aspects of the currently implemented design procedures for structures equipped with seismic isolators, being most findings applicable to the design of high-damping elastomeric-based isolators. This research work covers three different, but closely related, topics that correspond to the chapters of this thesis: (i) the development of a simplified and versatile element for seismic isolation modeling; (ii) a comprehensive statistical analysis on the uncertainty of the effective properties of elastomeric isolators, comprising results from more than 2,000 tests; and (iii) an extensive review of damping modification factors  $\eta$ , proposing the implementation of the recently developed spectral shape metric *SaRatio* as a useful predictor to estimate  $\eta$  for a given ground motion record.

The first phase of this research (Chapter II) presents a general-purpose simplified element model for seismic isolation bearings. The model force-displacement relationship is based on an elastoplastic, a linear, and a nonlinear spring arranged in parallel. The model mathematical formulation is more straightforward than most of the currently available research-oriented models. It only requires the identification of six parameters that, in exceptional cases, can be defined as shear-strain dependent, but, as the results of the study show, can also be defined as constants, still delivering accurate predictions. It is highly expected that this new modeling tool can be widely used for practitioners to select the best isolator type for a given project. By simple modification of its parameters, the model adequately represents the force-displacement curves of high damping rubber bearings (HDRBs), lead core rubber bearings (LRBs), and simple friction pendulums (FPS).

The model parameter identification was carried out using four quasi-static cyclic and two earthquake simulator tests of different HDRB and LRB specimens. Different error indexes between test-measured and model-predicted values were implemented in the parameter identification stage, generating several optimal sets and studying the model ability to predict seismic response for each case. For the HDRB specimen under consideration, exhibiting significant hardening, the force-based optimization method delivers a more robust parameter set with small deviations between test and model-predicted values, regardless of the metric (dissipated energy, force, or stiffness) used to quantify the error. On the other hand, stiffness-based optimization is biased to the high shear-strain hardening range, and then, model-predicted values are not accurate enough in the low shear-strain range, where stiffness is smaller and can generate unrealistic displacement increases while numerically integrating the oscillator seismic response.

As expected, increasing the number of displacement-dependent parameters delivers a better fit. However, results showed that for a small number of displacement-dependent parameters (one or two), the model delivers results accurate enough for selecting the optimal isolator type for a given project. When displacement-dependent parameters are implemented in response history, a linear functional form relating the parameter with the shear-strain is recommended. Other functional forms were studied, but their results do not depart considerably from the linear approach.

The second phase of this dissertation covers isolators' effective properties, evaluated from the results of non-destructive prototype and production tests, and used in equivalent lateral force and response spectrum methods. The effective secant stiffness  $k_{eff}$  and the effective damping  $\beta_{eff}$  are calculated by averaging results from repeated deformation cycles and,

despite their inherent randomness, are afterward treated as deterministic. Effective properties variability is influenced by complex phenomena, especially for HDRBs, including high shear-strain hardening, scragging, and strain-rate effects that modify the isolator response between deformation cycles. As the first step in a vast effort to quantify this variability, the effective properties' uncertainty of an extensive dataset of isolators was evaluated using the *Guide to the expression of Uncertainty in Measurement GUM* and Monte-Carlo simulation methods. The uncertainty sources considered in the study were the variability between deformation cycles and instrumentation errors.

Chilean design code NCh2745, for structures with seismic isolation, mandates to discard the first deformation cycle to characterize the isolator's scragged properties. A thorough analysis of the outcome of this provision was carried out. As expected, effective stiffness results show that the mean uncertainty and the uncertainty variability, for the complete 2,400 isolators dataset, are higher in the *unscragged* case than in the *scragged* case. Contrastingly, there is no clear trend when comparing the effective damping mean uncertainty of the *unscragged* and the *scragged* cases, as the inclusion of the whole force-displacement curve in the damping uncertainty calculation reduces the scragging influence. Mean dataset relative-expanded uncertainties, for the *unscragged* case at the design shear strain, were 4.67% and 3.15% for effective stiffness and damping, respectively. When the *scragged* case was considered, these values changed to 3.02% and 3.80%. These reported mean values considered intercycle variability and instrumentation error as uncertainty sources.

When intercycle variability was considered as the only uncertainty source, the maximum relative-expanded uncertainties were 8% and 11% for stiffness and damping, respectively.

These maximum values increased to 9% and 12% when the uncertainty from laboratory instrumentation was included.

A second-order term in the Taylor expansion of the measurand uncertainty was included in this work. Results showed that for the functional forms used to assess isolators' effective properties, the first-order Taylor approximation is accurate enough. Differences between uncertainties calculated with the *GUM* first-order approximation, the *GUM* second-order approximation, and Monte-Carlo simulations were negligible.

Based on the results presented in this dissertation, a novel analysis approach is currently being implemented to split the uncertainty into two components, the former due to pure random variability and the latter due to the *scragging* effect. Once these effects are separated, a detailed comparison between the scragging-related uncertainties and the currently implemented property modification factors in ASCE/SEI 7-16 will be carried out.

Finally, the third phase of this doctoral dissertation (Chapter IV) presents a profound study of the widely used damping modification factors  $\eta$  used to correct the seismic demand in equivalent lateral force or response spectrum methods when structure damping departs from 5% damping ratio. Record-to-record variability of  $\eta$  was analyzed through a statistical analysis of 5,270 ground motions records from 1,137 Chilean interface earthquakes by computing  $\eta$  factors for oscillators with periods of vibration ranging from  $T = 0.05$  s to  $T = 6.0$  s, and damping ratios ranging from 0.5% to 50%. Damping modification factors  $\eta$  were calculated for arbitrary and RotI50 horizontal components. Results from both approaches do not differ noticeably, as most ground motion records have large source-to-site distances.

As extensively documented in the literature and confirmed by the results in this dissertation, damping modification factors are strongly dependent on damping ratio, vibration period, earthquake magnitude, and earthquake distance. However, this work's main novelty is the evaluation of the spectral shape effect on  $\eta$ , using epsilon ( $\epsilon$ ) and *SaRatio*, two recently-proposed spectral shape proxy parameters.

An extensive study to define the optimal period range for *SaRatio* calculation was carried out and then, a constant interval of  $[0.2 \cdot T_1, 1.3 \cdot T_1]$  was implemented. Results showed that *SaRatio* is a much better predictor than earthquake magnitude or duration, especially in moderate and long-period systems with high damping ratios, i.e., base-isolated structures. Additionally, it was proven that in highly damped structures, the  $\eta$  versus *SaRatio* relationship is mildly dependent on oscillator period and earthquake magnitude. Therefore a straightforward and novel regression model was proposed, able to estimate  $\eta$  based on only two predictors: damping ratio and *SaRatio*.

Faulting mechanism, when events with similar magnitudes and durations were considered, and soil class were not found to have a significant influence on  $\eta$ .

A comparison between median  $\eta$  from this study and those in current Chilean seismic codes shows that code factors are unconservative. Large magnitude earthquakes tend to show reductions that are, on average, 16% smaller than the reductions prescribed by the code. Small magnitude earthquakes lead to reductions significantly smaller than the code.

In summary, modeling techniques and design procedures for isolated structures can be oversimplified, especially in the HDRBs case. Large shear-strain hardening could increase force and acceleration demands on protected structures and simultaneously reduce

displacement demand over the isolators; however, this effect is completely neglected in current design practice. The element model presented in this dissertation is currently being implemented to quantify the aforementioned effects through response history analysis.

Regarding effective properties uncertainty quantification, an effort is being made to separate the scragging effect from the pure random variability expected in repeated measurements.

Once these effects are separated, values for HDRBs property modification factors, currently not available in the literature, could be proposed.

## APPENDIX A

The expression for the uncertainty propagation using a second-order Taylor expansion is derived as follows:

A second-order approximation of a function  $y = f(x_1, x_2, \dots, x_n)$  can be written as

$$y(x_1, x_2, \dots, x_n) = y(\bar{x}_1, \bar{x}_2, \dots, \bar{x}_n) + \sum_{i=1}^n \frac{\partial y}{\partial x_i} (x_i - \bar{x}_i) + \frac{1}{2} \sum_{i=1}^n \frac{\partial^2 y}{\partial x_i^2} (x_i - \bar{x}_i)^2 \quad (\text{A-1})$$

Applying the expectation operator

$$E[y(x_1, x_2, \dots, x_n)] = \bar{y} = E \left[ y(\bar{x}_1, \bar{x}_2, \dots, \bar{x}_n) + \sum_{i=1}^n \frac{\partial y}{\partial x_i} (x_i - \bar{x}_i) + \frac{1}{2} \sum_{i=1}^n \frac{\partial^2 y}{\partial x_i^2} (x_i - \bar{x}_i)^2 \right] \quad (\text{A-2})$$

The first term in the right side of the equation is constant, and the second term vanishes to zero as it includes the term  $E(x_i - \bar{x}_i)$ , then rewriting equation (A-2) gives:

$$\bar{y} = y(\bar{x}_1, \bar{x}_2, \dots, \bar{x}_n) + \frac{1}{2} \sum_{i=1}^n \frac{\partial^2 y}{\partial x_i^2} E[(x_i - \bar{x}_i)^2] \quad (\text{A-3})$$

Subtracting equation (A-3) from (A-1):

$$y - \bar{y} = \sum_{i=1}^n \frac{\partial y}{\partial x_i} (x_i - \bar{x}_i) + \frac{1}{2} \sum_{i=1}^n \frac{\partial^2 y}{\partial x_i^2} (x_i - \bar{x}_i)^2 - \frac{1}{2} \sum_{i=1}^n \frac{\partial^2 y}{\partial x_i^2} E[(x_i - \bar{x}_i)^2] \quad (\text{A-4})$$

Then, squaring equation (A-4):

$$(y - \bar{y})^2 = \left[ \sum_{i=1}^n \frac{\partial y}{\partial x_i} (x_i - \bar{x}_i) + \frac{1}{2} \sum_{i=1}^n \frac{\partial^2 y}{\partial x_i^2} (x_i - \bar{x}_i)^2 - \frac{1}{2} \sum_{i=1}^n \frac{\partial^2 y}{\partial x_i^2} E[(x_i - \bar{x}_i)^2] \right]^2 \quad (\text{A-5})$$

Expanding the right side of the equation gives:

$$\begin{aligned}
(y - \bar{y})^2 &= \left[ \sum_{i=1}^n \frac{\partial y}{\partial x_i} (x_i - \bar{x}_i) \right]^2 + \left[ \frac{1}{2} \sum_{i=1}^n \frac{\partial^2 y}{\partial x_i^2} (x_i - \bar{x}_i)^2 \right]^2 + \left[ \frac{1}{2} \sum_{i=1}^n \frac{\partial^2 y}{\partial x_i^2} E[(x_i - \bar{x}_i)^2] \right]^2 \\
&+ 2 \left[ \sum_{i=1}^n \frac{\partial y}{\partial x_i} (x_i - \bar{x}_i) \right] \left[ \frac{1}{2} \sum_{i=1}^n \frac{\partial^2 y}{\partial x_i^2} (x_i - \bar{x}_i)^2 \right] \\
&+ 2 \left[ \sum_{i=1}^n \frac{\partial y}{\partial x_i} (x_i - \bar{x}_i) \right] \left[ -\frac{1}{2} \sum_{i=1}^n \frac{\partial^2 y}{\partial x_i^2} E[(x_i - \bar{x}_i)^2] \right] \\
&+ 2 \left[ \frac{1}{2} \sum_{i=1}^n \frac{\partial^2 y}{\partial x_i^2} (x_i - \bar{x}_i)^2 \right] \left[ -\frac{1}{2} \sum_{i=1}^n \frac{\partial^2 y}{\partial x_i^2} E[(x_i - \bar{x}_i)^2] \right]
\end{aligned} \tag{A-6}$$

Applying the expectation operator and simplifying some terms:

$$\begin{aligned}
E[(y - \bar{y})^2] &= E \left( \left[ \sum_{i=1}^n \frac{\partial y}{\partial x_i} (x_i - \bar{x}_i) \right]^2 \right) + E \left( \left[ \frac{1}{2} \sum_{i=1}^n \frac{\partial^2 y}{\partial x_i^2} (x_i - \bar{x}_i)^2 \right]^2 \right) \\
&+ E \left( \left[ \frac{1}{2} \sum_{i=1}^n \frac{\partial^2 y}{\partial x_i^2} E[(x_i - \bar{x}_i)^2] \right]^2 \right) \\
&+ E \left( \left[ \sum_{i=1}^n \frac{\partial y}{\partial x_i} (x_i - \bar{x}_i) \right] \left[ \sum_{i=1}^n \frac{\partial^2 y}{\partial x_i^2} (x_i - \bar{x}_i)^2 \right] \right) \\
&- E \left( \left[ \sum_{i=1}^n \frac{\partial y}{\partial x_i} (x_i - \bar{x}_i) \right] \left[ \sum_{i=1}^n \frac{\partial^2 y}{\partial x_i^2} E[(x_i - \bar{x}_i)^2] \right] \right) \\
&- E \left( \left[ \frac{1}{2} \sum_{i=1}^n \frac{\partial^2 y}{\partial x_i^2} (x_i - \bar{x}_i)^2 \right] \left[ \sum_{i=1}^n \frac{\partial^2 y}{\partial x_i^2} E[(x_i - \bar{x}_i)^2] \right] \right)
\end{aligned} \tag{A-7}$$

The fifth term in the right side vanishes to zero as it includes  $E(x_i - \bar{x}_i)$ . For convenience, the expectation and summation operators are interchanged in the last term. Rewriting gives:

$$\begin{aligned}
E[(y - \bar{y})^2] &= E\left(\left[\sum_{i=1}^n \frac{\partial y}{\partial x_i} (x_i - \bar{x}_i)\right]^2\right) + \frac{1}{4} E\left(\left[\sum_{i=1}^n \frac{\partial^2 y}{\partial x_i^2} (x_i - \bar{x}_i)^2\right]^2\right) \\
&\quad + \frac{1}{4} E\left(\left[\sum_{i=1}^n \frac{\partial^2 y}{\partial x_i^2} E[(x_i - \bar{x}_i)^2]\right]^2\right) \\
&\quad + E\left(\left[\sum_{i=1}^n \frac{\partial y}{\partial x_i} (x_i - \bar{x}_i)\right] \left[\sum_{i=1}^n \frac{\partial^2 y}{\partial x_i^2} (x_i - \bar{x}_i)^2\right]\right) \\
&\quad - \frac{1}{2} \left(\left[\sum_{i=1}^n \frac{\partial^2 y}{\partial x_i^2} E(x_i - \bar{x}_i)^2\right] \left[\sum_{i=1}^n \frac{\partial^2 y}{\partial x_i^2} E[(x_i - \bar{x}_i)^2]\right]\right)
\end{aligned} \tag{A-8}$$

In the third term, all addends are constant; then, the expectation operator can be removed.

Consequently, like terms (third and fifth) can be combined.

$$\begin{aligned}
E[(y - \bar{y})^2] &= E\left(\left[\sum_{i=1}^n \frac{\partial y}{\partial x_i} (x_i - \bar{x}_i)\right]^2\right) + \frac{1}{4} E\left(\left[\sum_{i=1}^n \frac{\partial^2 y}{\partial x_i^2} (x_i - \bar{x}_i)^2\right]^2\right) \\
&\quad + E\left(\left[\sum_{i=1}^n \frac{\partial y}{\partial x_i} (x_i - \bar{x}_i)\right] \left[\sum_{i=1}^n \frac{\partial^2 y}{\partial x_i^2} (x_i - \bar{x}_i)^2\right]\right) - \frac{1}{4} \left[\sum_{i=1}^n \frac{\partial^2 y}{\partial x_i^2} E[(x_i - \bar{x}_i)^2]\right]^2
\end{aligned} \tag{A-9}$$

The summations in equation (A-9) are expanded and written in a more convenient matrix

format. Then the first term gives:

$$\begin{aligned}
&E\left(\left[\sum_{i=1}^n \frac{\partial y}{\partial x_i} (x_i - \bar{x}_i)\right]^2\right) \\
&= \sum_{i=1}^n \left(\frac{\partial y}{\partial x_i}\right)^2 E[(x_i - \bar{x}_i)^2] \\
&\quad + 2 \sum_{i=1}^{n-1} \sum_{j=i+1}^n \frac{\partial y}{\partial x_i} \frac{\partial y}{\partial x_j} E[(x_i - \bar{x}_i)(x_j - \bar{x}_j)] = \mathbf{g}^T \mathbf{cov}(\mathbf{x}_i) \mathbf{g}
\end{aligned} \tag{A-10}$$

where

$$\mathbf{g} = \left[ \frac{\partial y}{\partial x_1} \quad \frac{\partial y}{\partial x_2} \quad \dots \quad \frac{\partial y}{\partial x_n} \right]^T \tag{A-11}$$

and

$$\mathbf{cov}(x_i) = \mathbf{E} \begin{bmatrix} (x_1 - \bar{x}_1)^2 & (x_1 - \bar{x}_1)(x_2 - \bar{x}_2) & \dots & (x_1 - \bar{x}_1)(x_n - \bar{x}_n) \\ (x_2 - \bar{x}_2)(x_1 - \bar{x}_1) & (x_2 - \bar{x}_2)^2 & \dots & (x_2 - \bar{x}_2)(x_n - \bar{x}_n) \\ \vdots & \vdots & \ddots & \vdots \\ (x_n - \bar{x}_n)(x_1 - \bar{x}_1) & (x_n - \bar{x}_n)(x_2 - \bar{x}_2) & \dots & (x_n - \bar{x}_n)^2 \end{bmatrix} \quad (\text{A-12})$$

The second term can be expressed as:

$$\begin{aligned} & \frac{1}{4} \mathbf{E} \left( \left[ \sum_{i=1}^n \frac{\partial^2 y}{\partial x_i^2} (x_i - \bar{x}_i)^2 \right]^2 \right) \\ &= \frac{1}{4} \sum_{i=1}^n \left( \frac{\partial^2 y}{\partial x_i^2} \right)^2 \mathbf{E} [(x_i - \bar{x}_i)^4] \\ &+ \left( \frac{1}{4} \right) (2) \sum_{i=1}^{n-1} \sum_{j=i+1}^n \frac{\partial^2 y}{\partial x_i^2} \frac{\partial^2 y}{\partial x_j^2} \mathbf{E} [(x_i - \bar{x}_i)^2 (x_j - \bar{x}_j)^2] \\ &= \frac{1}{4} (\mathbf{g}')^T \mathbf{krt}(x_i) \mathbf{g}' \end{aligned} \quad (\text{A-13})$$

where

$$\mathbf{g}' = \begin{bmatrix} \frac{\partial^2 y}{\partial x_1^2} & \frac{\partial^2 y}{\partial x_2^2} & \dots & \frac{\partial^2 y}{\partial x_n^2} \end{bmatrix} \quad (\text{A-14})$$

and

$$\mathbf{krt}(x_i) = \mathbf{E} \begin{bmatrix} (x_1 - \bar{x}_1)^4 & (x_1 - \bar{x}_1)^2 (x_2 - \bar{x}_2)^2 & \dots & (x_1 - \bar{x}_1)^2 (x_n - \bar{x}_n)^2 \\ (x_2 - \bar{x}_2)^2 (x_1 - \bar{x}_1)^2 & (x_2 - \bar{x}_2)^4 & \dots & (x_2 - \bar{x}_2)^2 (x_n - \bar{x}_n)^2 \\ \vdots & \vdots & \ddots & \vdots \\ (x_n - \bar{x}_n)^2 (x_1 - \bar{x}_1)^2 & (x_n - \bar{x}_n)^2 (x_2 - \bar{x}_2)^2 & \dots & (x_n - \bar{x}_n)^4 \end{bmatrix} \quad (\text{A-15})$$

The third term gives:

$$\begin{aligned}
E \left( \left[ \sum_{i=1}^n \frac{\partial y}{\partial x_i} (x_i - \bar{x}_i) \right] \left[ \sum_{i=1}^n \frac{\partial^2 y}{\partial x_i^2} (x_i - \bar{x}_i)^2 \right] \right) \\
= \sum_{i=1}^n \left( \frac{\partial y}{\partial x_i} \right) \left( \frac{\partial^2 y}{\partial x_i^2} \right) E[(x_i - \bar{x}_i)^3] \\
+ \sum_{i=1}^n \sum_{\substack{j \neq i \\ j=1}}^n \left( \frac{\partial y}{\partial x_i} \right) \left( \frac{\partial^2 y}{\partial x_j^2} \right) E[(x_i - \bar{x}_i)(x_j - \bar{x}_j)^2] = (\mathbf{g})^T \mathbf{skw}(\mathbf{x}_i) \mathbf{g}'
\end{aligned} \tag{A-16}$$

where  $\mathbf{g}$  and  $\mathbf{g}'$  were defined in equations (A-11) and (A-14) respectively and:

$$\mathbf{skw}(\mathbf{x}_i) = E \begin{bmatrix} (x_1 - \bar{x}_1)^3 & (x_1 - \bar{x}_1)(x_2 - \bar{x}_2)^2 & \dots & (x_1 - \bar{x}_1)(x_n - \bar{x}_n)^2 \\ (x_2 - \bar{x}_2)(x_1 - \bar{x}_1)^2 & (x_2 - \bar{x}_2)^3 & \dots & (x_2 - \bar{x}_2)(x_n - \bar{x}_n)^2 \\ \vdots & \vdots & \ddots & \vdots \\ (x_n - \bar{x}_n)(x_1 - \bar{x}_1)^2 & (x_n - \bar{x}_n)(x_2 - \bar{x}_2)^2 & \dots & (x_n - \bar{x}_n)^3 \end{bmatrix} \tag{A-17}$$

Finally, the fourth term can be expanded as shown:

$$\begin{aligned}
\frac{1}{4} \left[ \sum_{i=1}^n \frac{\partial^2 y}{\partial x_i^2} E[(x_i - \bar{x}_i)^2] \right]^2 &= \\
= \frac{1}{4} \sum_{i=1}^n \left( \frac{\partial^2 y}{\partial x_i^2} \right)^2 E[(x_i - \bar{x}_i)^2]^2 & \\
+ \left( \frac{1}{4} \right) (2) \sum_{i=1}^{n-1} \sum_{j=i+1}^n \left( \frac{\partial^2 y}{\partial x_i^2} \right) \left( \frac{\partial^2 y}{\partial x_j^2} \right) & (E[(x_i - \bar{x}_i)^2]) (E[(x_j - \bar{x}_j)^2]) \\
= \frac{1}{4} \mathbf{g}'^T \mathbf{var}^2(\mathbf{x}_i) \mathbf{g}' &
\end{aligned} \tag{A-18}$$

where

$$\mathbf{var}^2(\mathbf{x}_i) = \begin{bmatrix} E[(x_1 - \bar{x}_1)^2]^2 & E[(x_1 - \bar{x}_1)^2]E[(x_2 - \bar{x}_2)^2] & \dots & E[(x_1 - \bar{x}_1)^2]E[(x_n - \bar{x}_n)^2] \\ E[(x_2 - \bar{x}_2)^2]E[(x_1 - \bar{x}_1)^2] & (E[(x_2 - \bar{x}_2)^2])^2 & \dots & E[(x_2 - \bar{x}_2)^2]E[(x_n - \bar{x}_n)^2] \\ \vdots & \vdots & \ddots & \vdots \\ E[(x_n - \bar{x}_n)^2]E[(x_1 - \bar{x}_1)^2] & E[(x_n - \bar{x}_n)^2]E[(x_2 - \bar{x}_2)^2] & \dots & (E[(x_n - \bar{x}_n)^2])^2 \end{bmatrix}$$

(A-19)

Rewriting equation (A-9) in a compact matrix format gives:

$$\mathbf{Var}(\mathbf{y}) = \mathbf{g}^T \mathbf{cov}(x_i) \mathbf{g} + \frac{1}{4}(\mathbf{g}')^T \mathbf{krt}(x_i) \mathbf{g}' + (\mathbf{g})^T \mathbf{skw}(x_i) \mathbf{g}' - \frac{1}{4}\mathbf{g}'^T \mathbf{Var}^2(x_i) \mathbf{g}' \quad (\text{A-20})$$

expression that was implemented in the presented manuscript.

## APPENDIX B

The second derivatives required to evaluate equations (11) and (15) in Chapter III are shown below:

$$\frac{\partial^2 k_{eff}}{\partial F^{+2}} = 0 \quad (\text{B-1})$$

$$\frac{\partial^2 k_{eff}}{\partial F^{-2}} = 0 \quad (\text{B-2})$$

$$\frac{\partial^2 k_{eff}}{\partial \Delta^{+2}} = \frac{2(F^+ - F^-)}{(\Delta^+ - \Delta^-)^3} \quad (\text{B-3})$$

$$\frac{\partial^2 k_{eff}}{\partial \Delta^{-2}} = \frac{2(F^+ - F^-)}{(\Delta^+ - \Delta^-)^3} \quad (\text{B-4})$$

$$\frac{\partial^2 \beta_{eff}}{\partial E_{loop}^2} = 0 \quad (\text{B-5})$$

$$\frac{\partial^2 \beta_{eff}}{\partial k_{eff}^2} = \frac{4}{\pi} \frac{E_{loop}}{k_{eff}^3 (\Delta^+ - \Delta^-)^2} \quad (\text{B-6})$$

$$\frac{\partial^2 \beta_{eff}}{\partial \Delta^{+2}} = \frac{-12}{\pi} \frac{E_{loop}}{k_{eff} (\Delta^+ - \Delta^-)^4} \quad (\text{B-7})$$

$$\frac{\partial^2 \beta_{eff}}{\partial k_{eff}^2} = \frac{12}{\pi} \frac{E_{loop}}{k_{eff} (\Delta^+ - \Delta^-)^4} \quad (\text{B-8})$$